Exhumation of deep mountain roots: lessons from the Western Tatra Mountains, northern Slovakia

by

Yves Moussallam

Thèse soumise à la Faculté des études supérieures et postdoctorales
En vue de l'obtention de la maitrise en sciences de la terre

Thesis submitted to the Faculty of Graduate and Postdoctoral Studies
In partial fulfillment of the requirements for the M.Sc. degree in Earth Sciences

Ottawa-Carleton Geosciences Centre / Institut Ottawa-Carleton pour les Géosciences
University of Ottawa / Université d'Ottawa
Department of Earth Sciences / Département des Sciences de la Terre
Ottawa, Canada

May 2010

Abstract

The Tatric crystalline unit of the Western Carpathians in northern Slovakia displays an inverted metamorphic sequence where high-grade migmatite and orthogneiss units are overlying lower-grade mica schists. Enclosed within the migmatites are lenses of eclogite-bearing amphibolites. Conventional geothermobarometry coupled with isochemical modeling constrained P-T paths that exhibit contrasting metamorphic histories for rock units that are now heterogeneously interleaved. Relict eclogite facies assemblages with occasionally preserved omphacite record post-peak pressure conditions of 1.7-1.8 GPa followed by near isothermal decompression at ~750 °C leading to intensive re-equilibration of eclogites at high-pressure granulite facies conditions and development of diopside + plagioclase symplectitic textures. New ID-TIMS Sm-Nd dating of garnet separated from the omphacite-bearing eclogite yields a whole rock-garnet isochron age of 337 ± 10 Ma, with an epsilon Nd isotopic composition of +8.3. While major element profiles across the garnets display little variation, the trace element distribution shows a typical HREE enrichment profile and a slight core to rim disparity with LREE and MREE concentrations higher in the cores and higher HREE in the rims. Granulite-facies migmatites that host the eclogite boudins record lower pressure metamorphic conditions of 1.2 GPa at ~750 °C and a similar retrograde path. The lower-grade micaschists reached metamorphic conditions of 0.8 GPa at ~650 °C. Monazite U-Pb analysis from a migmatite surrounding the eclogite boudins yields one population of ca. 380 Ma age. Another migmatite away from the eclogite yields two populations monazite ages. A robust 340 ± 11 Ma monazite U-Pb age is indistinguishable from our garnet age and U-Pb SIMS age of zircons in the anatectic leucosome of the migmatite (347 ± 7 Ma). We interpret the ca. 340 Ma ages to represent the exhumation of the deep crustal root of

the Variscan orogen into the middle crust coeval with anatexis. A younger monazite U-Pb age of 300 ± 16 Ma is consistent with $^{40}Ar/^{39}Ar$ thermochronology data of ca. 310 Ma that is likely indicative of the Late Carboniferous I-type magmatism and cooling in the Tatric block. Cooling rates calculated by garnet diffusion modeling yield estimates of ~30 °/Ma. This exhumation was likely tectonically forced by the action of a rigid indentor which prompted the weak lower crust to be heterogeneously extruded to mid-crustal levels at a time coeval with anatexis and subsequently extruded with mid-crustal material to the upper crust.

Résumé

L'unité cristalline du Tatricum dans les Carpates Occidentales montre une séquence métamorphique inversée où des migmatites et orthogneiss de haut degré métamorphique surplombent des schistes à mica de plus faible degré. Encastré à l'intérieur de ces migmatites se trouvent des lentilles d'amphibolites contenant des éclogites. Une modélisation de diagrammes de phase iso-chimique associée à des calculs par géothermobarometrie permet d'approximer l'évolution du chemin P-T dévoilant des histoires métamorphiques distinctes pour des roches présentement mêlées. Des reliques d'assemblage du facies éclogite avec des omphacites occasionnellement préservées enregistrent des conditions de pressions de 1.7-1.8 GPa suivit par une décompression iso-thermale à ~750 °C entrainant la rééquilibration des eclogites dans le facies granulite et au développement de texture symplectique diopside + plagioclase. La datation des grenats séparés de l'eclogite par la méthode Sm-Nd par ID-TIMS procure un âge par isochrone roche-grenat de 337 ± 10 Ma, avec une valeur epsilon Nd isotopique de +8.3. Alors qu'un profile des éléments majeurs à travers ces grenats change peu, les éléments traces montrent une distribution typique d'enrichissement en HREE ainsi qu'une concentration en LREE et MREE plus haute dans le cœur et une concentration en HREE plus haute dans les bordures. Les migmatites de facies granulite qui contiennent les boudins d'éclogites enregistrent des conditions de pression plus basse de l'ordre de 1.2 GPa à ~750 °C suivit d'un chemin rétrograde similaire. Les schistes à micas de plus faible degré enregistrent des conditions métamorphiques culminant à 0.8 GPa et ~650 °C. La datation de monazite, par la méthode U-Pb, appartenant à une migmatite à proximité du boudin d'éclogite procure un âge unique de 380 Ma. Une autre migmatite située plus loin du boudin d'éclogite fournit deux populations d'âge de monazite. La plus robuste à 340 ± 11 Ma est similaire à l'âge obtenue par la géochronologie des

grenats de l'éclogite et par datation des zircons provenant du leucosome d'une migmatite (347 ± 7 Ma) par la méthode U-Pb SIMS. L'interprétation de ces âges aux alentours de 340 Ma est qu'ils représentent l'exhumation de la racine crustale profonde de l'Orogénèse Variscane à des profondeurs crustales moyennes, simultanément à une fusion partielle. Un âge plus jeune, de 300 ± 16 Ma, dérivé de la deuxième population de monazite est consistant avec les données thermo-chronologique obtenues par la méthode $^{40}Ar/^{39}Ar$ sur les muscovites (ca. 310 Ma). Ces âges indiquent probablement un épisode magmatique durant le Carbonifère supérieur produisant des granites de type I, ainsi que le refroidissement du bloque Tatric. Les taux de refroidissement calculées par modélisation de diffusion des grenats procure une estimation de ~30 °/Ma. L'exhumation des roches profonde était probablement induite par l'action d'un indenteur rigide qui a forcé la croûte inférieure, peu résistante, à être extraite de manière hétérogène à des profondeurs crustales moyennes à une période contemporaine à une anatexie de grande ampleur. Postérieurement, les roches appartenant à la croute inférieure et moyenne ont été extraites conjointement dans la croûte supérieure.

Table of contents

List of Tables

List of Figures

List of Acronyms

EMP:	Electron microprobe
HREE:	Heavy rare earth elements
ID-TIMS:	Isotope dilution - thermal ionization mass spectrometry
LA-ICPMS:	Laser ablation inductively coupled plasma mass spectrometry
LREE:	Light rare earth elements
MREE:	Medium rare earth elements
MSWD:	Mean square weighted deviation
P:	Pressure
REE:	Rare earth elements
SIMS:	Secondary ion mass spectrometry
SEM:	Scanning electron microscope
T:	Temperature
t:	Time
TIMS:	Thermal ionization mass spectrometry
WR:	Whole rock
XRF:	X-ray fluorescence

1. INTRODUCTION

Resolving the heterogenous nature of the crustal architecture in many metamorphic terranes has provided challenges for developing crustal-scale models of orogenic growth (e.g. Western Gneiss Region, Engvik & Andersen, 2000; Bohemian Massif, Schulmann et al., 2008). Notably, the occurrence of deep crustal boudins surrounded by migmatitic mid-crustal assemblages suggests an intimate association between the exhumation of the lower crust and widespread anatexis. In order to better understand the relationship between disparate metamorphic blocks, documenting the pressure-temperature-time (P-T-t) evolution of each of the assemblages is a reliable first step in the discrimination between tectonic models.

The Tatric crystalline unit of the Western Carpathians represents the easternmost exposure of the Variscan orogen in Europe which marks the collision of Laurasia with Gondwanian affiliated terranes during the Paleozoic. This orogen was marked by the closure of the Proto-Tethys Ocean with accretion of the Avalonia Terranes followed by the closure of the Rheic Ocean with the accretion of the Armorican Terrane Assemblage (Franke, 2000; Stampfli & Borel 2002). These rocks were most recently uplifted and exhumed from shallow depths during Alpine collision but their Variscan origin remains intact. The basement core of the Western Tatra Mountains displays an inverted metamorphic sequence where high-grade migmatite and orthogneiss units are overlying lower-grade mica schist (Janák, 1994; Janák et al. 1996, 1999). Enclosed within the migmatites are lenses and bands of eclogite-bearing amphibolites and the entire sequence was intruded by late- to post-orogenic granites.

In this contribution, our objective is to illuminate the metamorphic evolution of Variscan lower crustal assemblages by documenting the timing and style of tectono-thermal activity. For this purpose, we investigate the P-T-t paths of the sequences that compose the metamorphic core

of the Western Tatra. We first establish the P-T evolution of these units based on isochemical phase diagram calculations and conventional geothermobarometry. These results are then coupled with a strategic thermochronologic dataset, in an attempt to constrain the timing of juxtaposition of the main lithologic units during exhumation. We found dissimilar P-T path for lower and mid-crustal rock units homogenizing at ca. 340 Ma under mid-crustal conditions coeval with anatexis followed by exhumation and cooling at a rate of 30 °/Ma. These findings favor a tectonic model in which the middle crust represents a partially molten layer in which rocks from various depths are combined and jointly exhumed.

2. GEOLOGY & TECTONIC SETTING OF THE WESTERN TATRAS

The Variscan belt of Europe, stretching from Portugal to Slovakia, was a large, hot bivergent orogen (Beaumont et al., 2006) that marked the collision of Laurasia with Gondwanian-derived terranes during the Paleozoic. The eastern margin of the orogen is exposed in the Bohemian Massif of central Europe and is commonly subdivided (e.g. Suess, 1926; Kossmat, 1927) from NW to SE into the Rhenohercynian, Saxo-Thuringian, Teplá-Barrandian and Moldanubian zones (Fig. 2.1). The Rhenohercynian zone consists of greenschist facies, folded and thrusted Devonian and Early Carboniferous meta-sedimentary rocks that were deposited in a back-arc basin between the southern margin of Avalonia and the northern margin of Saxo-Thuringian (Franke, 2000). The Saxo-Thuringian zone is composed of a Neoproterozoic basement of migmatites and paragneisses intruded by Cambro-Ordovician calc-alkaline porphyritic granitoids converted to augen orthogneisses during the Variscan orogeny (e.g. Schulmann et al., 2009). These rocks are unconformably covered by Palaeozoic marine sediments assumed to be continuous from the Ediacaran to the Visean and the entire sequence is part of the Armorican Terrane Assemblage (Franke, 2000). The Teplá-Barrandian zone consist of Neoproterozoic basement unconformably overlain by Early Palaeozoic sediment and volcanic sequences and represent another member of the Armorican Terrane Assemblage. The Moldanubian zone is composed of high- to medium-grade metamorphic domain intruded by numerous Carboniferous granitic plutons, altogether forming the high-grade core of the Variscan orogeny. This Moldanubian zone has been interpreted to represent a back-arc basin during Siluro-Devonian time (e.g. Schulmann et al., 2009). The Brunia continent was subsequently defined as the western deformed margin of the Moravo-Silesian zone by Dudek (1980). The basement crystalline rocks of the Brunian continent

composed of granitoids, migmatites and schist, have been inferred to originate from Pan-African orogenic events (e.g. Finger et al., 2000; Friedl et al., 2004) and is unconformably overlain by Early to Late Palaeozoic strata. Schulmann et al. (2008) hypothesized that the Brunian continental promontory acted as an indentor on the Moldanubian domain leading to the development of a channel flow-like mid-crustal system during the Variscan orogeny.

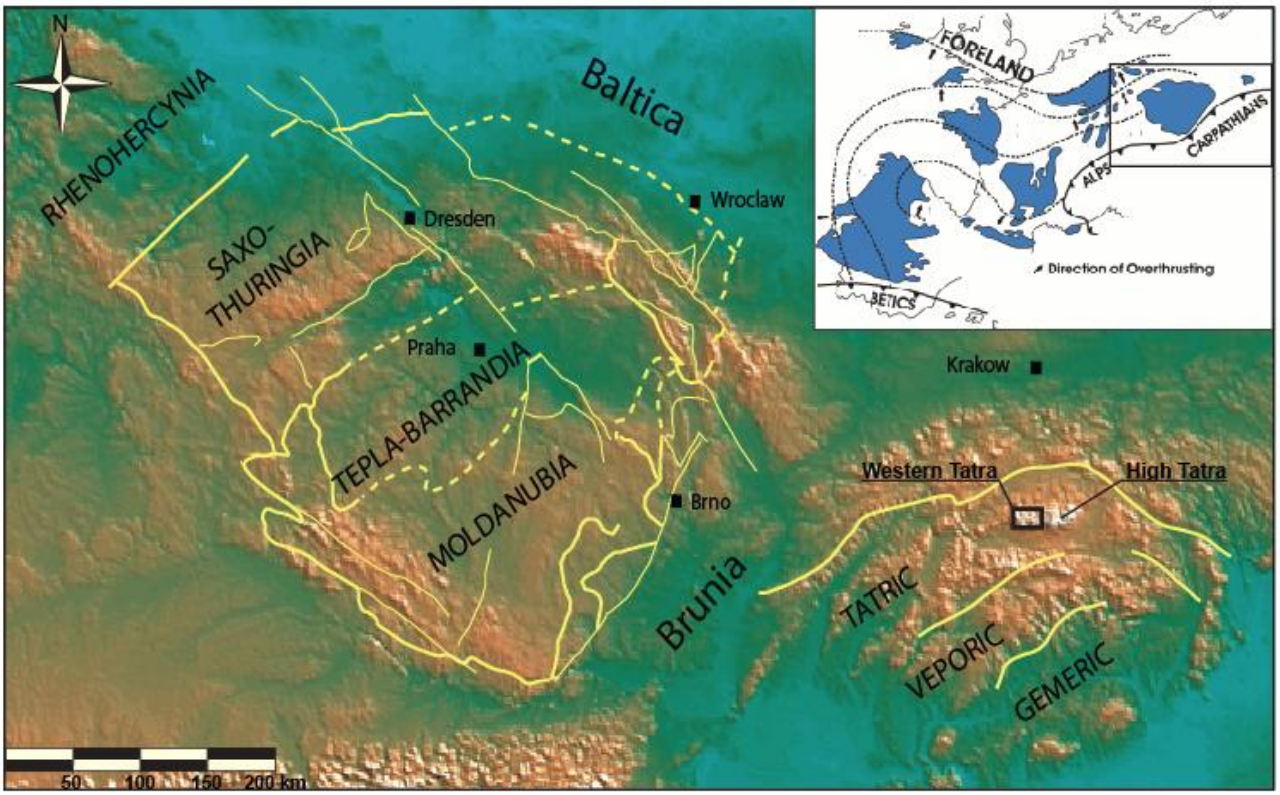

Figure 2.1: Simplified tectonic map of the Bohemian Massif and the Tatra. Brunia and Baltica refer to proto-continents while Rhenohercynia, Saxo-Thurigia, Teplá-Barrandian and Moldanubia refer to Variscan zones and Tatric, Veporic and Gemeric refer to Carpathian units. The small black box shows the location of the Western Tatra and Figure 2.2. The upper right inset shows the position of the Bohemian Massif in the frame of the European Variscides (modified from Bromley & Holl, 1986)

The Western Tatra Mountains are located east of the Bohemian Massif, in northern Slovakia and southern Poland and are part of the younger (Cretaceous) Alpine-Carpathians belt which truncates the Variscan belt. The western part of the Carpathian belt is subdivided into three major tectonic units which were juxtaposed by north-directed Cretaceous thrusting. The rock units from the Western Tatra belong to the northernmost Tatric unit which is overlain to the south by the Veporic and the Gemeric units (e.g. Bezák et al., 1997). The pre-Mesozoic rocks from these units form the Variscan basement which is overlain by Mesozoic and Cenozoic sedimentary units. Previous workers (e.g. Janák, 1994) divided the crystalline basement into two superimposed tectonic units separated by a shear zone (Fig. 2.2). The lower structural unit mainly consists of micaschist and is divided into two metamorphic zones: the staurolite-kyanite zone and the kyanite-sillimanite (fibrolite) zone separated by the staurolite-out isograd in the west. It is at least 1000 m thick, shows evidence of ductile and brittle deformation and represents a metaflysch lithology (Janák, 1994). The base of the upper unit is dominated by banded amphibolites, some of which contain boudins of relict eclogites (Janák et al., 1996). Structurally above, the sequence is composed mainly of orthogneiss and sporadic kyanite-bearing paragneisses (Janák et al., 1999). Amphibolites and ortho- and paragneisses are surrounded by sillimanite-bearing migmatites. All of these rock types show deformation under ductile conditions and the whole sequence is intruded by Carboniferous granitoids of both S- and I-types (e.g. Kohút and Janák, 1994).

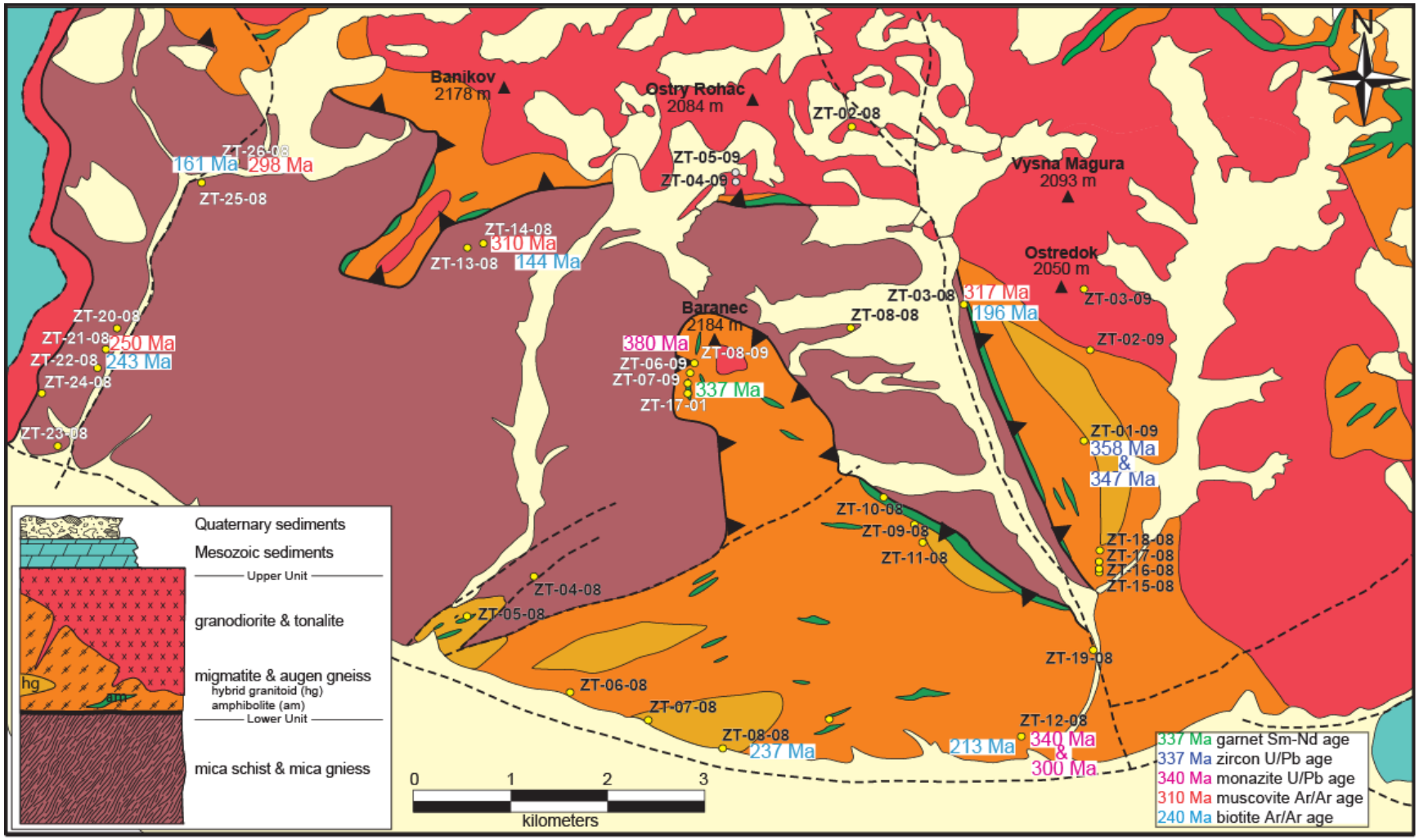

Figure 2.2: Simplified geological map of the western Tatra with sample locations and geochron results. Lower left inset shows the lithostratigraphy of the Western Tatra with the commonly used lower and upper structural unit subdivision (from Nemčok et al., 1994). Dashed lines represent brittle faults.

The structural contact between the two units is a shear zone separating the higher grade upper unit from the lower grade lower unit, producing an apparent inverted metamorphic sequence. This shear zone represents a folded low-angle trust fault, inferred to be Variscan in age (Janák, 1994; Janák et al., 1999). Dominant kinematic indicators suggest a SE-directed emplacement of the upper unit above the lower one during the first phase of deformation (Fritz et al., 1992; Janák, 1994). Four main periods of deformation have been identified (c.f. Janák et al., 1999). D1 is defined by a mineral lineation (muscovite, biotite, sillimanite, amphibole) that is likely related to SE-directed thrusting of the upper unit onto the lower unit. The second deformation event (D2) is defined by a composite foliation and re-orientation of L1 due to east-west shearing; (D2) was related to orogen-parallel extension. However, the Variscan normal faults are not preserved due to erosion of upper crustal levels in post-Variscan time, or they have been re-activated during Alpine tectonic events. Alpine deformation (D3) under brittle conditions is manifested by top-to-the-northwest shear, which is attributed to a Late Cretaceous contractional event. The last major deformation (D4) is related to uplift of the Tatra Mountains due to Late Tertiary transpression along west-east trending brittle wrench zones, accompanied by normal faulting in a north-south to northwest-southeast direction.

The tectonometamorphic evolution of the Western Tatra was gradually unraveled as geochronological data became available over the last two decades. Much of the basement of the Western Tatra is composed of schists and ortho- and paragneiss that preserve Silurian and Devonian protholith ages (Burchart, 1968; Poller et al., 1999, 2000; Burda, 2007). These earliest crustal growth ages are likely a product of magmatic activity during Caledonian subduction, similar to the basement ages of the Bohemian Massif directly to the west (Finger & von Quadt, 1995; Schulmann et al., 2005). Variscan reworking during collision and crustal thickening led to

pervasive metamorphism of the terrane. Timing constraints on this thermal episode remain enigmatic, as only a few studies have yielded reliable dates that are likely thought to represent the timing of metamorphism and anatexis during the Early Carboniferous (Poller et al., 1999, 2000). Cooling ages determined by $^{40}Ar/^{39}Ar$ dating from the granites and migmatites are 300-330 Ma (Maluski et al., 1993; Janák & Onstott, 1993; Janák 1994) and were variably reset due to post-Variscan magmatism and tectonic events. Notably, Janák (1994) conducted laser probe investigation of paragneisses of the High Tatra that yield biotite cooling ages between ca. 340 and 288 Ma.

Variscan orogenesis in the region was followed by Permian continental rifting, which marked the opening of the Meliata Ocean in the Triassic (Plašienka et al., 1999). Extension and reheating during the Permian is evident in $^{40}Ar/^{39}Ar$ cooling dates of individual biotite crystals (Janák, 1994). This Permian event has been documented in the Western Carpathians (Poller et al. 2002; Finger et al., 2003; Jeřábek et al., 2008) and in the Alps (e.g. Thöni & Miller, 2009) where it resulted in magmatism and low-pressure–high-temperature metamorphism (Schuster & Stüwe, 2008). The subsequent and latest Alpine deformation commenced in the Cretaceous with thrust-nappes and juxtaposition of the Tatric, Veporic and Gemeric units, and regional metamorphism up to amphibolite facies in the boundary between the Veporic and Gemeric units (Janák et al., 2001). Current topography and related uplift of the Western Tatra was constrained by apatite fission track dating and is as young as Middle Miocene (Kováč et al., 1994). This uplift has been related to the rotation of the Tatra block accommodated by movement in the sub-Tatric fault (e.g. Jurewicz, 2005), $^{40}Ar/^{39}Ar$ dating of pseudotachylytes suggests that this fault was active between 50 and 30 Ma (Kohút & Sherlock, 2003).

3. P-T PATH RECONSTRUCTION

3.1. Petrography and Sample Description

The crystalline basement of the Western Tatra is composed of four distinct lithologies: micaschists, migmatites, orthogneisses and eclogite-bearing amphibolites (Fig. 2.2 and 3.1). A suite of 35 samples was collected in four main regions in the study area (Fig. 2.1); to the west where micaschists from the lower unit are best exposed, to the east where migmatites, amphibolites and orthogneisses from the upper unit are well exposed, to the north near the contact with the granites and finally along and on both sides of the shear zones that mark the contact between the upper and lower unit and especially near the eclogite locality in the area of Baranec peak. For all of these samples thin sections were prepared and samples were selected for their respective analysis on the basis of petrographic inspection (least retrogressed, least weathered, etc.). Samples that presented diagnostic mineral assemblages and clearly identifiable textures with regard to geothermobarometric calculation were selected for P-T work and samples containing larger and non-chloritized micas and amphiboles were selected for $^{40}Ar/^{39}Ar$ dating.

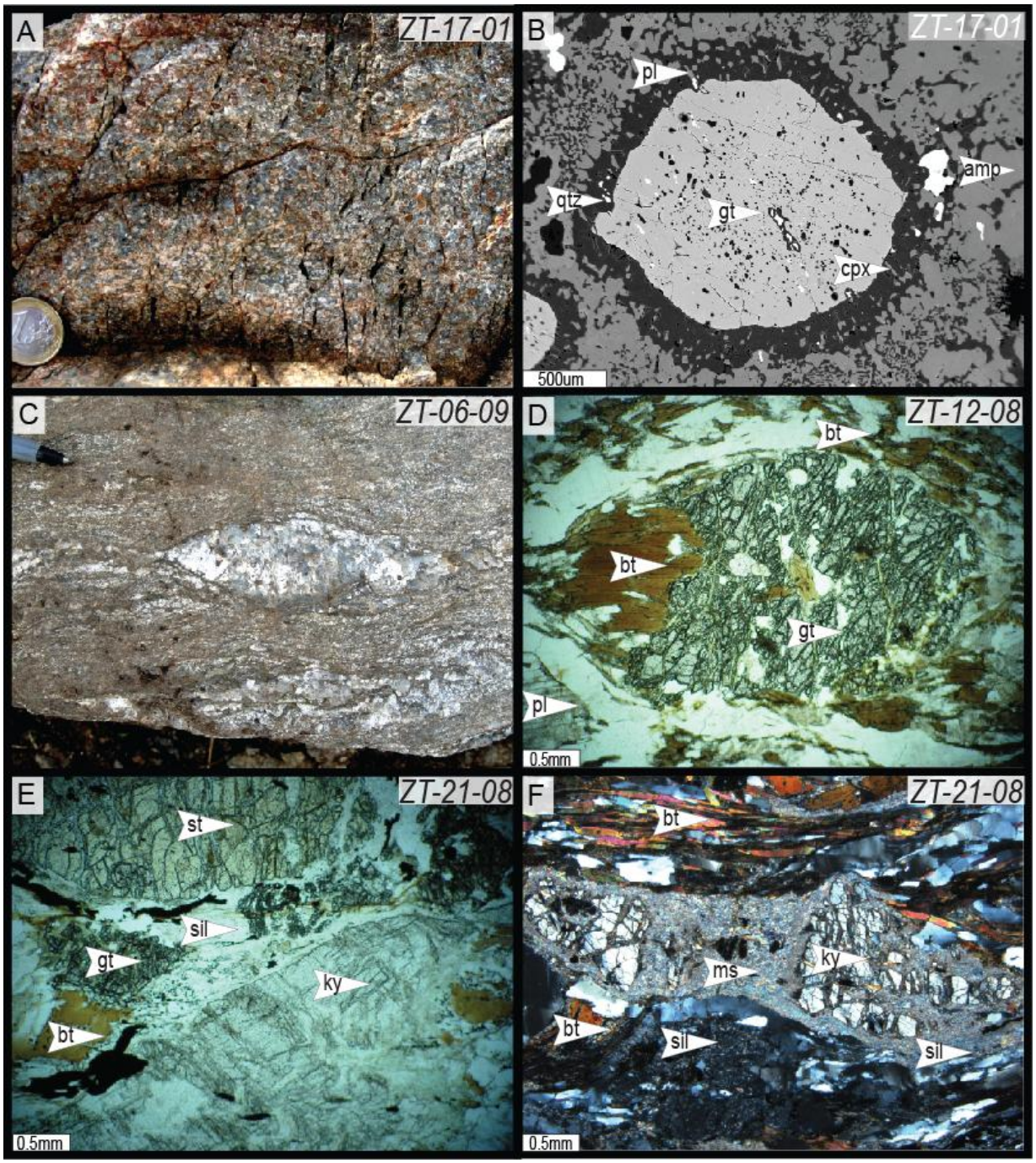

Figure 3.1: Photographs and photomicrographs from representative samples of the Western Tatra. A: Field photograph, close-up of an eclogite boudin within an amphibolite lense (upper unit). B: SEM image of a garnet from an eclogite sample rimmed by Cpx + Pl + Amph + Qtz symplectites. C: Photo of a layered to stromatitic type migmatites from the upper unit with leucosome boudin. D: Photomicrograph of a garnet from the melanosome of a migmatite sample (upper unit). E: Photomicrograph of relict kyanite and staurolite porphyroblast in a micaschist from the lower unit. F: Photomicrograph of a kyanite porphyroblast partially replaced by muscovite and silimanite in a micaschist from the lower unit.

Migmatites, generally stromatitic in texture, show segregation into leucosome and melanosome and/or mesosome. Leucosomes are composed of plagioclase, quartz, muscovite and garnet. Melanosomes are composed of biotite, plagioclase and garnet. A typical mineral assemblage is garnet + biotite + K-feldspar + muscovite + plagioclase + quartz ± sillimanite. Sillimanite (fibrolite) replaced muscovite and biotite is retrograded to chlorite (see also Janák et al., 1999 for more details). Accessory minerals include zircon and monazite. Orthogneisses exhibit a coarse grained texture with augen-like potassium feldspar and/or plagioclase with asymmetric tails indicating deformation under ductile conditions and SE-vergent sense of shearing (Janák, 1994).

Amphibolite lenses occur within the migmatites and contain boudins of retrogressed eclogite. Banding occurs at a mm- to dm-scale with alternations of felsic and mafic domains, indicative of high-temperature ductile deformation. The mafic layers consist of hornblende and plagioclase. The felsic layers are dominated by plagioclase and quartz, with minor hornblende and garnet. Few biotite crystals are present and are mostly retrograded to chlorite. Epidote veinlets are present and concordant to the banding. Accessory phases include rutile and zircon.

Eclogite occasionally preserve clinopyroxene with less than 10% jadeite component (Table 1) as inclusions within garnets. Garnets occur as euhedral to subhedral crystals with plagioclase-amphibole kelyphitic rims. Inclusions in the garnet, other than clinopyroxene, are mostly quartz, plagioclase, amphibole, rutile, ilmenite and very rarely epidote and zoisite. Clinopyroxenes occur mostly as vermicular grains intergrown with plagioclase in symplectites indicating breakdown of an earlier omphacite clinopyroxene. The eclogite sample analyzed in this study was previously described by Janák (1996).

Micaschists show typical mineral assemblage of garnet + biotite + muscovite + plagioclase + quartz + sillimanite ± kyanite ± staurolite. Kyanite is partly replaced by fibrolitic sillimanite that clearly postdates the main fabric. Porphyroblasts are typically subhedral, kyanite and staurolite crystals are up to 3 mm in size, and garnets are smaller (up to 1.5 mm) and more abundant (see also Janák 1994 for more details).

3.2. Phase equilibrium modeling & geothermobarometry

In order to constrain the P-T path of the samples described above we calculated isochemical phase diagrams. Pressure-temperature isochemical phase diagrams represent fields of theoretically most stable assemblage for a rock of fixed composition within P-T space. We used the program PERPLEX-07 (Connolly, 1990; http://www.perplex.ethz.ch) to calculate isochemical phase diagrams using the thermodynamic database and mineral solutions models from Holland & Powell (1998). Bulk rock XRF analyses were performed using the X-ray facilities at the University of Ottawa (Canada), to estimate the average bulk rock composition. If a fraction of anatectic melt was lost during the prograde evolution, the measured rock composition represents bulk composition after the loss of melt. As a consequence, the calculated isochemical phase diagrams are most appropriate for the peak T and retrograde evolution of the rocks. Isochemical phase diagrams were constructed for three rock types: i) micaschist from the lower unit, ii) migmatite of the upper unit and iii) eclogite from the upper unit.

For the lower unit micaschist our modeled chemical system includes Na_2O-MgO-Al_2O_3-SiO_2-K_2O-CaO-MnO-FeO and we considered the following phases: biotite, garnet, plagioclase, staurolite and chlorite. For this micaschist (ZT-21-08) the presence of relict staurolite and

kyanite replaced by fibrolitic sillimanite and the absence of potassium feldspar constrains the P-T evolution of the lower unit to peak pressure conditions between 0.8 and 1.1 GPa and the peak temperature between 625 and 775 °C (Fig. 3.2). For the upper unit migmatites our modeled chemical system includes Na_2O-MgO-Al_2O_3-SiO_2-K_2O-CaO-MnO-FeO and we considered the following phases: biotite, garnet, plagioclase and potassium feldspar. For this migmatite (ZT-12-08) the presence of potassium feldspar, sillimanite and the occurrence of kyanite in nearby migmatite (Janák et al., 1999) suggest peak pressure conditions between 0.9 and 1.2 GPa and peak temperature between 740 and 810 °C. For the eclogite our modeled chemical system includes Na_2O-MgO-Al_2O_3-SiO_2-CaO-MnO-FeO and we considered the following phases: garnet, amphibole, plagioclase and omphacite. The calculations are based upon saturated H_2O during metamorphism. Several calculations with varying amount of H_2O have been carried out and have had little to no effect on most of the phase stability boundaries. In all calculations we have treated the iron as Fe^{2+} since no Fe^{3+} oxides were observed. For this eclogite (ZT-17-01) the presence of omphacite inclusions within garnet suggest post-peak pressures above 1.6 GPa and post-peak temperatures between 700 and 900 °C. This was followed by the breakdown of omphacite to amphibole ± plagioclase ± quartz assemblage in the amphibolite facies.

In order to further constrain the P-T evolution of these rock samples conventional geothermobarometric calculations were performed using coexisting mineral assemblages. The mineral composition were analyzed using the Cameca SX100 at the Slovak Academy of Science, Bratislava, Slovakia, in point-beam mode at 15 kV and 10 nA (Table 3.1). The garnet-biotite thermometer was used for both of the metapelitic samples (micaschist and migmatite) using the calibration of Ganguly & Saxena (1984) and Ferry & Spear (1978) with Berman (1990) garnet model. Several barometers were used for the metapelitic samples depending on their mineral

assemblages. The Gt-Bt-Ms-Sil barometer was used with the calibration from Hodges & Crowley (1985) and Holdaway et al. (1988). The Gt-Pl-Sil-Qtz barometer was used with the calibration of Newton & Haselton (1981) and Koziol (1989). The Gt-Pl-Bt-Qtz barometer was used with the calibration of Hoisch (1990) and the Gt-Pl-Ms-Qtz barometer was used with the calibration from Hoisch (1990). For the metabasite (eclogite), the Gt-Hbl and Gt-Cpx thermometers were used using the calibration from Graham & Powell (1984), Perchuk et al. (1985) and Ellis & Green (1979) and Powell (1985) respectively. The Gt-Pl-Hbl-Qtz and the Gt-Pl-Cpx-Qtz barometers were used using the calibration from Kohn & Spear (1990), Mocher et al. (1988) and Powell & Holland (1988) with Ganguly & Saxena (1984) garnet model. The pressures and temperatures were calculated with the computer software "Thermobarometry" 2.1 of Spear & Kohn (1999; http://ees2.geo.rpi.edu/MetaPetaRen/Frame-software.html/). In all calculations we have treated the iron as Fe^{2+}.

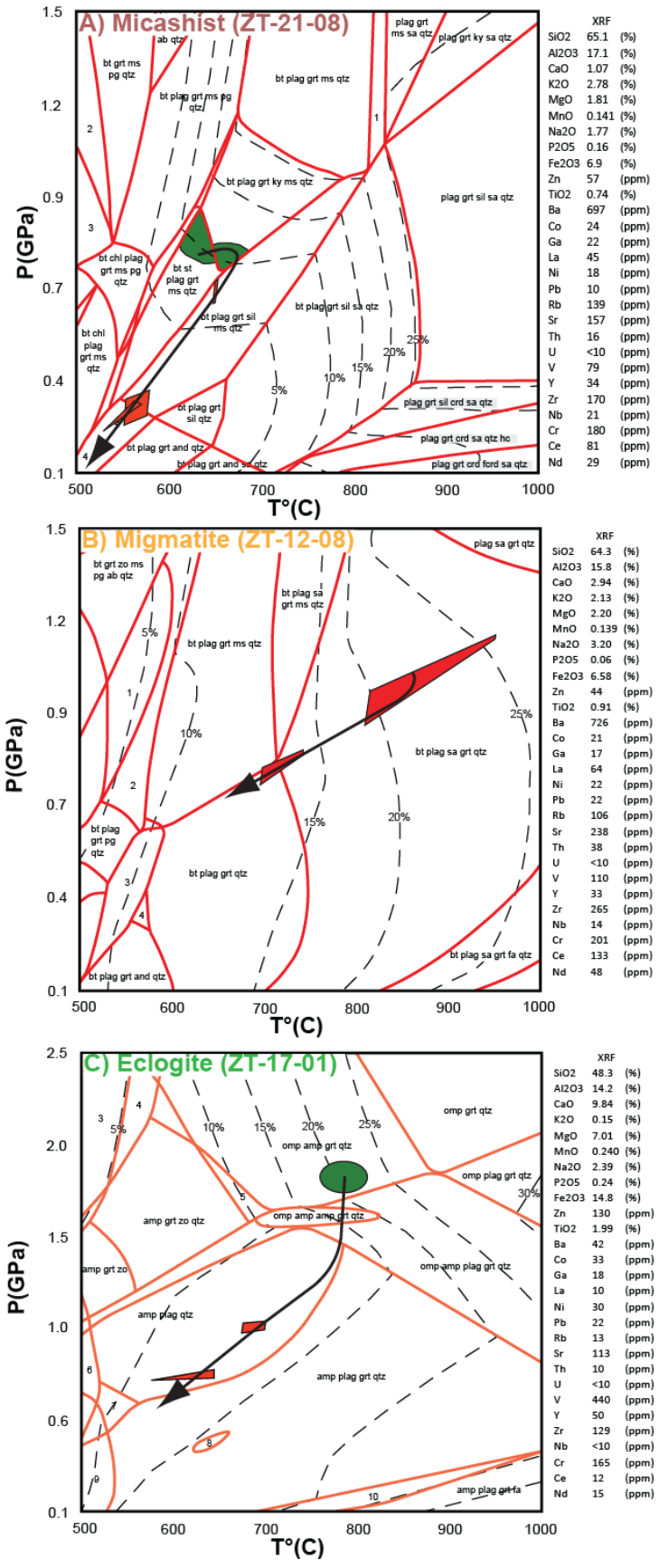
A) Micashist (ZT-21-08)
B) Migmatite (ZT-12-08)
C) Eclogite (ZT-17-01)
P(GPa)
T°(C)
XRF
SiO2 65.1 (%)
Al2O3 17.1 (%)
CaO 1.07 (%)
K2O 2.78 (%)
MgO 1.81 (%)
MnO 0.141 (%)
Na2O 1.77 (%)
P2O5 0.16 (%)
Fe2O3 6.9 (%)
Zn 57 (ppm)
TiO2 0.74 (%)
Ba 697 (ppm)
Co 24 (ppm)
Ga 22 (ppm)
La 45 (ppm)
Ni 18 (ppm)
Pb 10 (ppm)
Rb 139 (ppm)
Sr 157 (ppm)
Th 16 (ppm)
U <10 (ppm)
V 79 (ppm)
Y 34 (ppm)
Zr 170 (ppm)
Nb 21 (ppm)
Cr 180 (ppm)
Ce 81 (ppm)
Nd 29 (ppm)
SiO2 64.3 (%)
Al2O3 15.8 (%)
CaO 2.94 (%)
K2O 2.13 (%)
MgO 2.20 (%)
MnO 0.139 (%)
Na2O 3.20 (%)
P2O5 0.06 (%)
Fe2O3 6.58 (%)
Zn 44 (ppm)
TiO2 0.91 (%)
Ba 726 (ppm)
Co 21 (ppm)
Ga 17 (ppm)
La 64 (ppm)
Ni 22 (ppm)
Pb 22 (ppm)
Rb 106 (ppm)
Sr 238 (ppm)
Th 38 (ppm)
U <10 (ppm)
V 110 (ppm)
Y 33 (ppm)
Zr 265 (ppm)
Nb 14 (ppm)
Cr 201 (ppm)
Ce 133 (ppm)
Nd 48 (ppm)
SiO2 48.3 (%)
Al2O3 14.2 (%)
CaO 9.84 (%)
K2O 0.15 (%)
MgO 7.01 (%)
MnO 0.240 (%)
Na2O 2.39 (%)
P2O5 0.24 (%)
Fe2O3 14.8 (%)
Zn 130 (ppm)
TiO2 1.99 (%)
Ba 42 (ppm)
Co 33 (ppm)
Ga 18 (ppm)
La 10 (ppm)
Ni 30 (ppm)
Pb 22 (ppm)
Rb 13 (ppm)
Sr 113 (ppm)
Th 10 (ppm)
U <10 (ppm)
V 440 (ppm)
Y 50 (ppm)
Zr 129 (ppm)
Nb <10 (ppm)
Cr 165 (ppm)
Ce 12 (ppm)
Nd 15 (ppm)

Figure 3.2: P-T diagrams illustrating the metamorphic conditions of: (a) micashist from the lower unit, (b) migmatite from the upper unit and (c) eclogite from the upper unit. The P-T estimates are superimposed on isochemical phase diagrams. Dashed lines represent Isoplets of the pyrope content (in per cent) of garnet phase calculated using the garnet solution from Holland and Powell (1998). Numbered stability fields are as follow: A) 1= bt+plag+grt+ms+sa+qtz 2=bt+chl+grt+ms+pg+qtz 3=bt+chl+grt+zo+ms+pg+qtz 4=bt+plag+grt+and+ms+qtz B) 1=bt+plag+grt+zo+ms+pg+qtz 2=bt+plag+grt+ms+pg+qtz 3=bt+plag+grt+fst+qtz 4=bt+plag+grt+sil+qtz and C) 1=omp+amp+grt+lws 2= omp+amp+grt+lws+qtz 3=amp+grt+lws 4=amp+grt+lws+qtz 5= omp+amp+grt+zo+qtz 6=amp+grt+cld+qtz 7=amp+grt+mrg+qtz 8=amp+amp+plag+grt+qtz 9=amp+plag+grt+czo+qtz 10=amp+plag+grt+fa+qtz. All mineral abbreviations are following Kretz (1983) and Spear (1993). Green polygons are interpreted P-T estimates based on petrography, calculated mineral stability fields and garnet Isoplets. Red polygons are estimated P-T fields using conventional geothermobarometric calculations. Results from bulk rock XRF analyses used to compute the isochemical phase diagrams are reported beside each figure.

Ana No	mineral	Na2O	SiO2	Al2O3	MgO	Cl	K2O	CaO	TiO2	FeO	MnO	Cr2O3	Total
ZT-17-01 (Eclogite)													
ana1	cpx	0.71	53.74	2.26	12.82	0.03	0.01	22.79	0.16	8.93	0.11	0.06	101.61
ana2	cpx	0.71	52.80	2.41	12.79	0.00	0.02	22.80	0.22	8.58	0.15	0.05	100.53
ana3	grt	0.05	38.60	21.29	4.38	0.01	0.00	9.55	0.15	25.58	0.89	0.06	100.57
ana4	grt	0.18	38.32	21.14	4.30	0.00	0.04	9.71	0.20	25.19	0.89	0.00	99.99
ana5	plag	8.55	62.63	23.34	0.00	0.00	0.09	5.05	0.00	0.24	0.00	0.01	99.91
ana6	plag	7.78	60.57	24.40	0.00	0.00	0.05	6.46	0.09	0.38	0.03	0.00	99.77
ana9	amp	1.45	45.64	11.84	12.37	0.29	0.16	11.82	2.09	12.42	0.04	0.08	98.19
ana10	grt	0.03	38.97	21.58	4.14	0.01	0.01	9.78	0.10	25.86	0.75	0.05	101.28
ana11	plag	7.17	59.55	26.22	0.00	0.00	0.06	7.74	0.00	0.24	0.01	0.00	100.98
ana12	hbl	1.67	45.16	11.27	11.03	0.01	0.22	11.37	1.30	14.56	0.09	0.41	97.10
ana13	cpx	0.35	53.14	0.90	12.63	0.01	0.00	22.64	0.06	10.75	0.18	0.06	100.72
ana14	amp	0.99	49.49	6.66	12.87	0.01	0.08	11.60	0.79	15.10	0.10	0.02	97.72
ana15	plag	8.18	61.56	24.40	0.00	0.01	0.06	6.19	0.02	0.29	0.00	0.01	100.71
ana17	cpx	0.46	53.03	2.35	13.37	0.00	0.01	23.41	0.36	8.94	0.07	0.05	102.06
ana18	grt	0.00	38.76	21.53	4.99	0.00	0.01	9.04	0.06	26.17	0.65	0.03	101.23
ana19	cpx	0.35	53.26	1.53	13.40	0.01	0.00	23.32	0.20	9.56	0.13	0.04	101.80
ana20	cpx	0.46	54.57	1.41	13.53	0.01	0.01	22.92	0.10	9.32	0.11	0.07	102.50
ana21	amp	1.65	48.51	9.40	15.18	0.01	0.05	12.04	1.52	10.17	0.08	0.00	98.61
ana22	cpx	0.44	53.70	1.29	13.33	0.00	0.00	22.83	0.07	9.29	0.12	0.06	101.15
ana23	plag	7.61	60.25	25.40	0.00	0.00	0.03	7.42	0.00	0.46	0.00	0.03	101.20
ana24	grt	0.00	38.92	21.36	4.27	0.00	0.00	9.48	0.21	26.55	0.87	0.03	101.70
ana25	amp	1.35	46.31	11.04	12.94	0.03	0.11	11.88	1.74	13.02	0.03	0.10	98.60
ana28	cpx	1.87	52.93	4.68	11.91	0.00	0.00	21.11	0.26	7.64	0.04	0.00	100.45
ana29	grt	0.06	38.14	21.49	4.51	0.00	0.01	10.16	0.16	26.08	0.46	0.02	101.09
ana30	cpx	1.98	50.02	8.17	10.27	0.00	0.00	18.39	0.46	10.44	0.16	0.05	99.94
ana31	grt	0.04	39.12	21.51	4.10	0.01	0.00	9.76	0.18	26.32	0.72	0.05	101.80
ZT-21-08 (Micashist)													
an5	grt	0.00	37.46	20.95	2.60	0.01	0.00	2.19	0.02	35.93	1.88	0.02	101.04
an6	ms	0.84	46.43	37.58	0.45	0.02	9.38	0.09	0.13	1.63	0.05	0.01	96.61
an7	bt	0.11	34.43	18.57	8.55	0.26	7.78	0.12	1.57	23.25	0.23	0.01	95.06
an11	ms	0.80	47.58	36.74	0.53	0.00	9.60	0.02	0.06	1.03	0.01	0.01	96.37
an12	bt	0.05	31.50	19.44	8.28	0.28	6.03	0.03	1.27	24.93	0.14	0.07	92.05
an13	grt	0.01	37.36	21.08	1.58	0.00	0.00	2.03	0.02	35.34	3.35	0.06	100.82
an14	plag	7.62	59.87	25.61	0.00	0.01	0.05	7.21	0.00	0.57	0.07	0.02	101.07
an15	grt	0.01	37.17	20.98	2.13	0.01	0.01	2.21	0.00	35.14	2.71	0.05	100.42
an16	bt	0.14	35.30	19.15	8.38	0.09	8.64	0.00	1.81	21.07	0.05	0.00	94.83
an17	ms	0.00	37.32	21.00	1.23	0.01	0.05	2.14	0.02	32.50	5.77	0.00	100.04
an20	plag	8.33	62.23	24.17	0.00	0.00	0.06	5.67	0.01	0.01	0.02	0.02	100.53
an21	plag	8.15	62.26	24.59	0.00	0.03	0.09	5.66	0.01	0.00	0.00	0.01	100.81
ZT-12-08 (Migmatite)													
an1	bt	0.06	35.83	18.61	8.66	0.24	9.46	0.00	1.99	19.59	0.17	0.08	94.72
an2	grt	0.03	37.52	21.21	3.60	0.01	0.04	2.75	0.04	31.01	2.82	0.00	99.02
an3	ms	0.29	47.81	32.60	1.96	0.00	9.63	0.03	0.25	2.37	0.02	0.00	94.96
an4	plag	7.83	59.63	25.60	0.00	0.01	0.08	7.02	0.01	0.15	0.00	0.00	100.34
an5	grt	0.01	38.35	21.32	3.90	0.01	0.03	2.66	0.01	32.19	2.47	0.04	100.99
an6	bt	0.07	35.69	17.81	8.41	0.22	9.40	0.02	2.14	20.32	0.15	0.06	94.30
an7	plag	7.25	59.90	25.65	0.00	0.03	0.14	7.48	0.00	0.21	0.00	0.00	100.69

Table 3.1: Microprobe analyses of minerals from eclogite (ZT-17-01), micashist (ZT-21-08) and migmatite (ZT-12-08) used for PT estimates, reported as oxides weight %

For the micaschist sample, three P-T estimates have been used to reconstruct the retrograde P-T path. These estimates were petrographically-controlled with the highest pressure-temperature estimate based on microprobe analysis of well-preserved phases and the lowest metamorphic conditions based on retrogressed domains. These P-T estimates constrain the retrograde path and suggest peak conditions around 0.7 GPa and 650 °C. For the migmatite sample, two P-T estimates were used with the highest metamorphic conditions based on analysis of mineral inclusions in garnet and garnet core composition. The lower estimate was based on garnet rim composition and adjacent phases. These calculations are in accordance with the estimates based on the isochemical phase diagrams and constrain the peak metamorphic conditions to 0.9-1.2 GPa and 750-825 °C, yielding little insight into the retrograde path. For the eclogite, two P-T estimates were calculated. Temperature conditions of 750-800°C are based on omphacite inclusions in garnet, constrained from Grt-Cpx thermometer at pressure conditions of 1.6-1.8 GPa estimated from the omphacite stability in the phase diagram (Fig. 3.2). This was followed by isothermal decompression to 1.2 GPa as calculated from symplectitic and kelyphitic assemblages with the Grt-Cpx-Plg-Qtz and Grt-Amp-Plg-Qtz geobarometers.

Isochemical phase diagram modeling and conventional geothermobarometry give us insight on the pressure-temperature evolution of each rock. Nevertheless these P-T paths contain no temporal information. To resolve the timing of exhumation, a tactical set of thermochronometers was applied.

4. GEOCHRONOLOGY & THERMOCHRONOLOGY

4.1. Garnet Sm-Nd geochronology & elemental distribution

In order to assign timing constraint to the calculated P-T paths, several thermally-dependant radiometric systems were employed. The Sm-Nd radiometric dating system was used to date garnets from the eclogite (sample ZT-17-01). These garnets were subjected to major and trace element analysis. Major element core to rim composition profile were obtained by electron microprobe analysis. The results are presented in table 4.1 and figure 4.1. Trace element analysis was performed by laser ablation inductively-coupled plasma mass spectrometer (LA-ICPMS) consisting of a New Wave Nd:YAG 213 nm laser coupled to a quadrupole Thermo X Series 2 ICPMS at the Department of Earth Sciences, Laurentian University, Canada. The measurements were normalized to the Ca content obtained by electron microprobe. The ablation was done in a He atmosphere and Ar was mixed to the carrier gas before it entered the ICPMS. We used a 55 μm spot and a repetition rate of 10 Hz for the analysis. Energy density was kept constant at about 9 to 10 J/cm^2 and the beam width was 5 ns. Analysis time ranged between 50-60 seconds, including 30 seconds background acquisition. We used the NIST 614 synthetic glass standard that is doped with trace elements at a nominal concentration of about 1 ppm for external calibration. The quantification procedure is described in Heinrich et al. (2003). The results are presented in table 4.2 and normalized on the REE chondrite composition (Boynton, 1994) in figure 4.2.

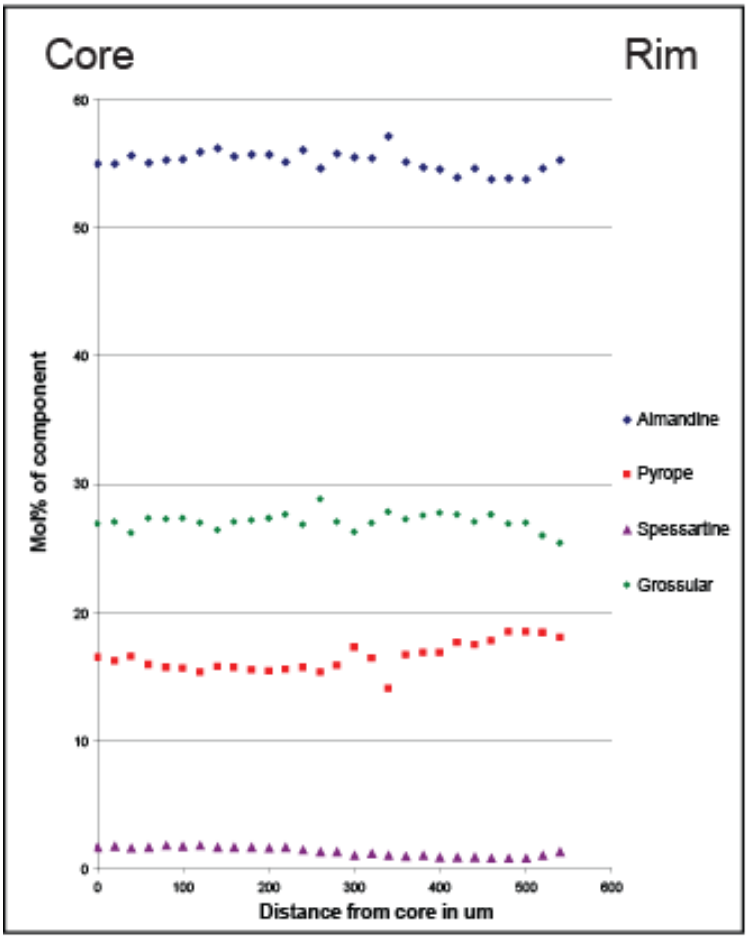

Figure 4.1: Eclogite garnet zoning profile of sample ZT-17-01 presented in mol% compositions of garnet end-members. The original growth zoning is only partially preserved and retrograde zoning is apparent at the rim.

distance from core (μm)	Fe Wt% element	Mg Wt% element	Mn Wt% element	Ca Wt% element	Almandine (mole %)	Pyrope (mole %)	Spessartine (mole %)	Grossular (mole %)	Fe # (ratio)	Mg # (ratio)
0	3.371	1.009	0.100	1.646	55.022309	16.477605	1.637991	26.862095	76.954371	23.045629
20	3.361	0.989	0.106	1.653	55.015064	16.192220	1.730569	27.062147	77.260444	22.739556
40	3.367	1.001	0.094	1.585	55.676031	16.550877	1.561437	26.211654	77.084888	22.915112
60	3.367	0.973	0.101	1.672	55.075686	15.915238	1.656496	27.352580	77.581306	22.418694
80	3.386	0.962	0.108	1.669	55.287152	15.700504	1.764932	27.247413	77.882769	22.117231
100	3.366	0.948	0.106	1.660	55.367219	15.590385	1.740497	27.301899	78.028592	21.971408
120	3.181	0.871	0.101	1.536	55.914473	15.312648	1.779539	26.993340	78.501661	21.498339
140	3.378	0.949	0.096	1.585	56.216118	15.800459	1.605488	26.377935	78.059969	21.940031
160	3.350	0.946	0.100	1.629	55.600561	15.705961	1.658423	27.035056	77.974019	22.025981
180	3.371	0.938	0.098	1.643	55.715057	15.509058	1.615218	27.160666	78.224990	21.775010
200	3.403	0.941	0.096	1.668	55.715078	15.405650	1.573445	27.305827	78.338735	21.661265
220	3.368	0.951	0.099	1.688	55.165516	15.570344	1.619343	27.644797	77.988048	22.011952
240	3.422	0.957	0.088	1.639	56.043466	15.671557	1.442029	26.842948	78.147456	21.852544
260	3.319	0.932	0.076	1.749	54.622166	15.333721	1.255765	28.788347	78.080871	21.919129
280	3.387	0.961	0.077	1.642	55.823912	15.842805	1.276100	27.057183	77.893776	22.106224
300	3.441	1.070	0.062	1.629	55.481861	17.248529	0.997504	26.272106	76.284289	23.715711
320	3.371	0.998	0.071	1.641	55.426482	16.414705	1.173673	26.985140	77.151400	22.848600
340	3.765	0.924	0.065	1.831	57.172688	14.029484	0.992751	27.805077	80.296269	19.703731
360	3.342	1.013	0.056	1.652	55.126957	16.710962	0.915719	27.246362	76.737965	23.262035
380	3.353	1.032	0.059	1.686	54.694437	16.833498	0.963521	27.508544	76.465841	23.534159
400	3.298	1.017	0.053	1.677	54.546809	16.829092	0.881826	27.742272	76.421885	23.578115
420	3.295	1.077	0.050	1.686	53.948052	17.626628	0.822551	27.602769	75.373095	24.626905
440	3.276	1.047	0.052	1.620	54.640173	17.458328	0.872318	27.029181	75.785450	24.214550
460	3.259	1.076	0.047	1.674	53.806540	17.767406	0.783920	27.642133	75.176154	24.823846
480	3.298	1.133	0.047	1.646	53.855302	18.504685	0.767111	26.872903	74.426910	25.573090
500	3.269	1.123	0.047	1.636	53.808444	18.483933	0.774028	26.933594	74.431698	25.568302
520	3.311	1.117	0.059	1.573	54.626686	18.431252	0.978430	25.963631	74.771732	25.228268
540	3.344	1.090	0.077	1.536	55.305325	18.024826	1.267980	25.401869	75.419626	24.580374

Table 4.1: Core to rim microprobe major element zonation profile in eclogite garnet (sample ZT-17-01).

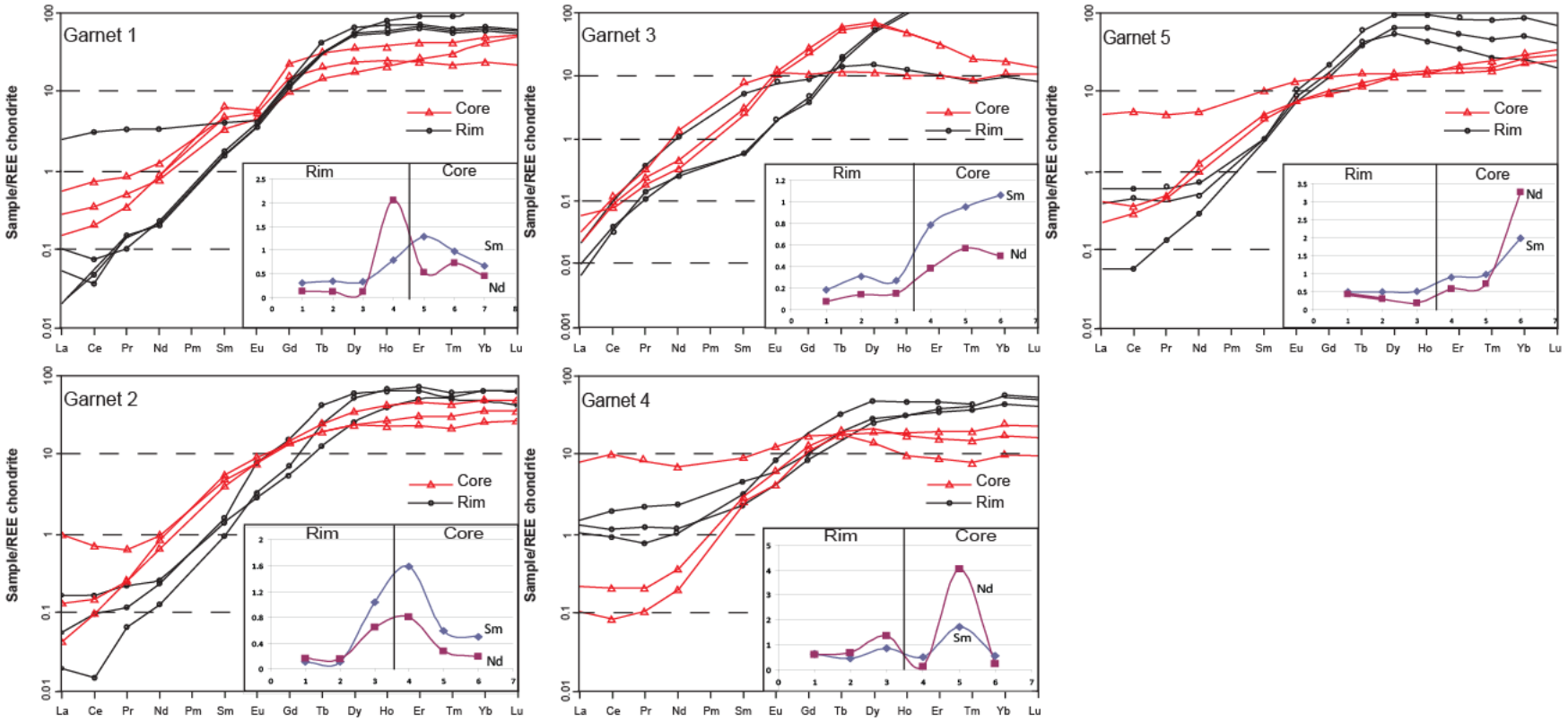

Figure 4.2: Chondrite normalized (Boynton, 1994) REE core and rim zonation patterns in five garnet from eclogite sample ZT-17-01. Lower right inset in each graph shows the core to rim concentration (ppm) of Sm and Nd in each garnet.

Location	Spot #	Ti	Sr	Y	Ba	La	Ce	Pr	Nd	Sm	Eu	Gd	Tb	Dy	Er	Yb	Lu
ZT-17-01_Garnet 1																	
Rim	1	463.4	15.5	125.3	15.650	0.031	0.058	0.013	0.137	0.314	0.320	3.944	2.103	22.660	15.910	15.040	2.128
Rim	2	377.2	0.4	113.0	0.012	0.016	0.029	0.018	0.127	0.360	0.303	3.494	1.608	19.180	14.580	13.880	1.880
Rim	3	465.1	0.1	122.9	-0.008	0.006	0.037	0.017	0.124	0.339	0.271	3.333	1.632	18.510	15.360	14.270	2.013
Rim	4	487.3	1.0	146.3	0.000	0.810	2.565	0.419	2.116	0.819	0.332	3.164	1.526	20.310	21.720	23.990	3.657
Core	5	1260.0	1.4	64.7	0.030	0.045	0.156	0.040	0.516	1.241	0.405	5.921	1.507	11.710	8.884	10.530	1.668
Core	6	1138.0	3.7	46.7	0.168	0.168	0.561	0.098	0.709	0.943	0.387	4.047	0.981	7.831	5.099	5.025	0.719
Core	7	719.8	0.4	41.2	0.004	0.080	0.263	0.057	0.436	0.644	0.335	2.521	0.711	5.772	5.563	8.873	1.652
ZT-17-01_Garnet 2																	
Rim	8	276.0	0.1	125.0	0.000	0.006	0.012	0.009	0.079	0.188	0.251	1.973	1.219	17.620	15.940	14.220	2.128
Rim	9	136.0	11.7	120.2	2.143	0.017	0.080	0.015	0.144	0.317	0.602	4.227	2.086	20.430	14.180	10.610	1.474
Rim	10	396.6	4.1	83.7	0.108	0.054	0.137	0.028	0.158	0.278	0.222	1.464	0.638	8.805	11.160	14.260	2.208
Core	11	1187.0	1.8	71.9	0.021	0.039	0.113	0.029	0.371	0.762	0.539	3.737	1.163	11.050	9.640	10.140	1.565
Core	12	18180.0	0.7	47.6	0.061	0.288	0.537	0.074	0.550	0.921	0.551	3.492	0.898	7.529	6.404	7.308	1.120
Core	13	763.4	1.8	38.4	0.314	0.013	0.074	0.030	0.485	1.029	0.664	3.484	0.941	7.391	4.862	5.361	0.838
ZT-17-01_Garnet 3																	
Rim	14	335.1	2.2	219.4	-0.041	0.003	0.033	0.013	0.174	0.113	0.150	1.266	0.947	18.200	39.690	63.800	10.110
Rim	15	350.2	0.3	202.5	0.000	0.002	0.028	0.018	0.160	0.115	0.157	1.057	0.886	17.360	34.560	52.190	7.944
Rim	16	400.6	3.4	26.2	1.381	0.007	0.085	0.045	0.667	1.063	0.620	2.467	0.703	5.145	2.211	2.087	0.270
Core	17	567.8	0.5	19.8	0.110	0.009	0.091	0.037	0.776	1.535	0.781	2.632	0.520	3.436	1.980	2.242	0.328
Core	18	540.3	1.2	85.7	0.128	0.007	0.073	0.028	0.269	0.569	0.857	6.888	2.509	19.630	6.268	3.393	0.408
Core	19	229.9	0.5	88.1	0.032	0.018	0.061	0.022	0.187	0.484	0.744	5.957	2.692	21.390	6.112	3.397	0.421
ZT-17-01_Garnet 4																	
Rim	20	1351.0	66.5	92.5	0.333	0.319	0.729	0.093	0.614	0.629	0.629	4.273	1.571	15.140	9.929	11.180	1.578
Rim	21	739.4	19.6	63.5	0.402	0.389	0.927	0.145	0.702	0.456	0.316	2.263	0.759	8.039	8.154	11.760	1.756
Rim	22	3959.0	151.0	69.5	1.033	0.462	1.581	0.272	1.392	0.881	0.449	2.599	0.894	9.255	7.297	9.341	1.359
Core	23	1190.0	0.6	35.9	-0.009	0.031	0.061	0.011	0.110	0.475	0.285	2.835	0.764	5.878	3.801	4.799	0.696
Core	24	2925.0	31.3	19.5	13.210	2.323	7.621	0.992	3.913	1.664	0.863	4.217	0.787	4.359	1.751	1.941	0.298
Core	25	316.4	20.0	32.7	0.017	0.062	0.152	0.023	0.200	0.535	0.427	3.285	0.911	6.133	3.088	3.518	0.504
ZT-17-01_Garnet 5																	
Rim	26	439.8	3.8	122.5	0.093	0.197	0.487	0.078	0.433	0.506	0.552	3.899	1.943	21.400	11.600	10.620	1.333
Rim	27	1608.0	5.9	174.7	0.246	0.118	0.372	0.051	0.303	0.501	0.809	5.842	2.900	31.070	19.330	18.130	2.347
Rim	28	369.7	0.8	90.2	0.035	0.018	0.047	0.017	0.178	0.519	0.663	4.421	2.112	17.730	7.465	5.557	0.667
Core	29	1787.0	5.0	30.3	0.100	0.123	0.270	0.055	0.548	0.870	0.532	2.451	0.574	4.685	3.656	4.624	0.738
Core	30	1018.0	3.7	32.7	0.155	0.065	0.220	0.051	0.699	0.949	0.539	2.298	0.540	4.700	4.311	6.273	1.082
Core	31	1105.0	23.6	32.6	0.000	44.750	120.200	16.540	70.100	14.530	3.445	8.832	0.891	5.791	3.693	4.884	0.794

Table 4.2: Rim and Core LA-ICPMS trace element zonation profile in eclogite garnets (sample ZT-17-01).

Major element garnet composition corresponds to almandine with significant grossular and pyrope contents. The major element distribution is very smooth with Mn decrease balanced by Mg increase from core to rim, and constant Fe and Ca. In the outermost part of the rims Mn and Fe concentrations increase, whereas Mg and Ca concentrations decrease as a consequence of resorption and diffusion during retrogression (Fig. 4.1 and Table 4.1). Trace element compositions on garnet from the eclogite all show a typical HREE enrichment profile and a slight core to rim disparity with LREE and MREE concentrations higher in the cores and higher HREE in the rims. The LREE are the most strongly zoned, MREE show little zoning and HREE show some zoning. The absence of a negative Eu anomaly suggests garnet growth in the absence of plagioclase for both core and rim. The distribution of Sm and Nd is presented in figure 4.2. The concentration of both Sm and Nd are higher in the garnet core than in the rim.

Garnet crystals from the eclogite were optically separated for ID-TIMS Sm-Nd geochronology, which was performed at the Laboratory of Geochronology, Center for Earth Sciences, University of Vienna, Austria. Before digestion, the handpicked garnet fractions were repeatedly rinsed, using acetone and de-ionized water in an ultrasonic bath, and the pure garnet fraction was additionally washed for 30 min in warm (70 °C) 2.5 N HCl. Handpicked garnet separates used for Sm-Nd analysis weighed 52 and 75 mg, respectively. Sample digestion for Sm-Nd analysis was performed in Savillex® beakers using an ultrapure 5:1 mixture of HF and $HClO_4$ for 10 days at 110 °C on a hot plate. For whole rock powders, a minimum dissolution time of 3 weeks was applied to ensure complete leaching of the REEs from refractory material such as zircon. After evaporating the acids, repeated treatment of the residue using 5.8 N HCl resulted in clear solutions for all samples. Upon cooling, 10% of the sample solution was split off and spiked for Sm and Nd concentration determination by isotope dilution (ID) using a mixed

REE tracer (^{147}Sm-^{150}Nd spike). The REE fraction was extracted using AG® 50W-X8 (200-400 mesh, Bio-Rad) resin and 4.0 N HCl. Nd and Sm were separated from the REE fraction using teflon-coated HdEHP and 0.24 and 0.8 N HCl, respectively, as elution media. Maximum total procedural blanks for both Sm and Nd were < 50 pg.

The extracted pure element fractions were loaded on Re filaments and run as metals using the Re double filament evaporation technique and a Finnigan® MAT262 for IDs, while Nd IC was measured on a ThermoFinnigan® Triton TI TIMS machine. A ^{143}Nd/^{144}Nd ratio of 0.511844 ± 0.000002 was determined for the La Jolla (Nd) international standard during the period of investigation. Within-run mass fractionation for Nd isotopes was corrected for relative to ^{146}Nd/^{144}Nd = 0.7219. Uncertainties on the Nd isotope ratios are quoted as $2\sigma_m$. For the ^{147}Sm/^{144}Nd ratios, a mean error of ±1% is applied, including blank contribution, uncertainties on spike composition, and machine drift; regression calculation is based on these uncertainties and the isochron calculations follow Ludwig (2003). Age calculations are based on a decay constant of 6.54 x 10^{-12} a^{-1} for ^{147}Sm (Lugmair & Marti, 1978); age errors are given at the 2σ level. For Nd, a continuous depletion of the upper mantle is assumed throughout geological time using the following Depleted Mantle (DM) model parameters: ^{147}Sm/^{144}Nd = 0.222, ^{143}Nd/^{144}Nd = 0.513114 (Michard et al., 1985).

The results from TIMS geochronology are summarized in table 4.3 and presented in figure 4.3. The Sm-Nd isochron is defined by one whole rock and two garnet fractions, one composed of "clean" garnet with very few and little inclusions and the second fraction composed of garnet with noticeable inclusions (under 10x magnification). The inclusions in the garnets are quartz, amphibole, clinopyroxene, plagioclase, rutile, titanite, epidote and zoisite. Since the isotopic ratio from the inclusion-bearing and inclusion-free garnet fractions both lie along the

same regression line as indicated by the rather low MSWD (= 3.7), any inclusions present in the "clean" garnet fraction does not distort the "true" garnet Sm-Nd age. This isochron gave an age of 337.2 ± 9.9 Ma and an epsilon Nd isotopic composition of +8.3. Sm-Nd garnet ages are commonly interpreted to represent cooling of the eclogite below 700 ± 50 °C (Tirone et al., 2005).

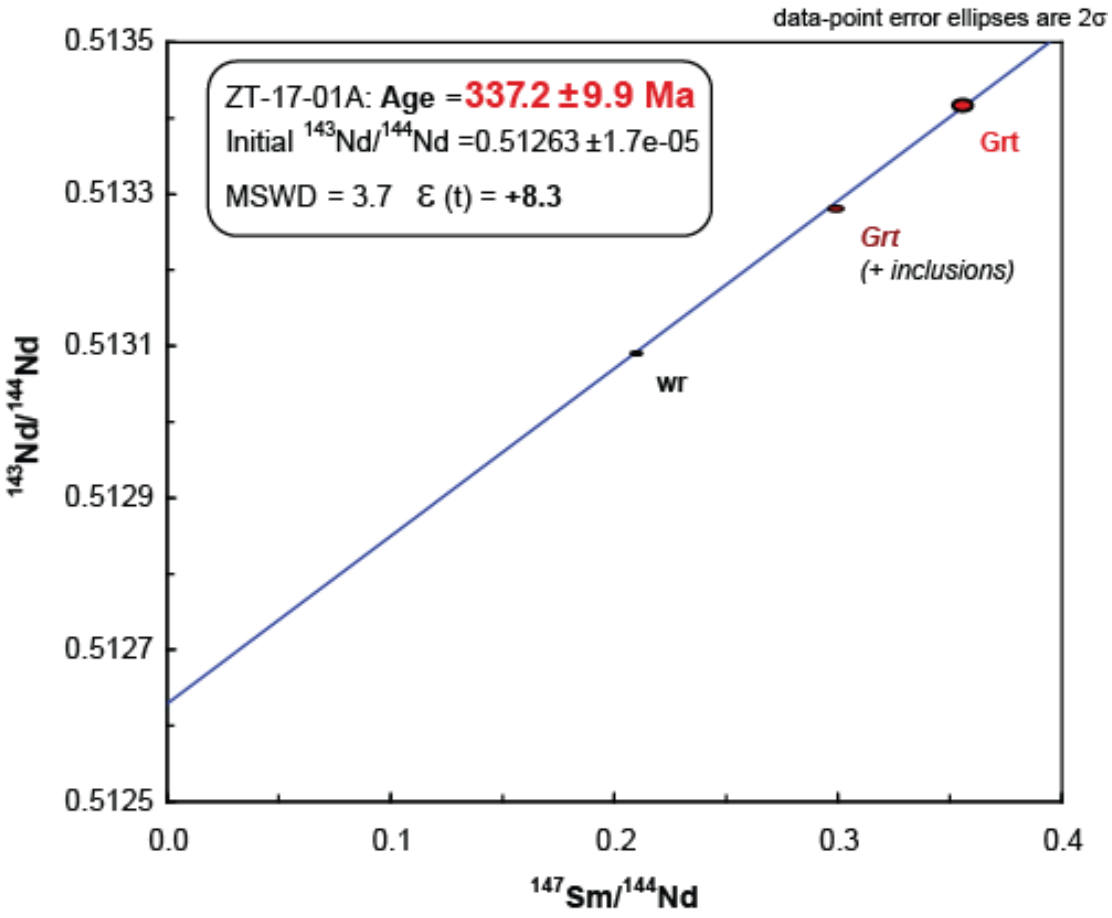

Figure 4.3: Sm-Nd isochron plot of the garnet analysis from eclogite sample ZT-17-01. Isochron is defined by a whole rock (wr) and two garnet fractions. See text for discussion.

sample	Sm (ppm)	Nd (ppm)	$^{147}Sm/^{144}Nd$	± 1 %	$^{143}Nd/^{144}Nd$	$\pm 2s_m$	Age	Initial $^{143}Nd/^{144}Nd$
Garnet "clean" (grt)	0.738	1.253	0.355950	0.003560	0.513421	0.000006		
Whole rock (wr)	4.090	11.859	0.208514	0.002085	0.513090	0.000001	337.2±9.9 Ma	0.51263±1.7e-05
Garnet "dirty" (grt dirty)	0.961	1.946	0.298688	0.002987	0.513283	0.000003		

Table 4.3: Summary of the Sm-Nd isotopic results from eclogite garnets (sample ZT-17-01)

4.2. U-Pb zircon geochronology

Zircon is the mineral of choice for dating high-temperature thermal event since its closure temperature (for the U-Pb system) is high (900°C; e.g. Mezger, 1990) and typically little affected by any lower-temperature events. It is based on these characteristics that we chose to use zircon dating to constrain the timing of the highest temperature event that affected the study area. Two distinct zircon populations were separated from the leucosome and melanosome portions of a 2 kg sample of migmatitic paragneiss (ZT-01-09) using standard mineral separation techniques. This particular sample was used because of the clear separation between the leucosome and melanosome at the outcrop scale. Felsic minerals such as quartz and feldspars concentrated into the coarse leucosome domain where we expected new zircon growth during anatexis, in contrast more mafic minerals such as biotite, garnet and also some quartz and plagioclase remained in the melanosome where we did not expect any zircon growth during anatexis. Under a binocular microscope, the zircon exhibited two distinct morphologies: the leucosome zircons are euhedral and elongated and the melanosome zircons are more equant and corroded. The zircon grains were pressed into pre-polished indium mounts with a piston-press assembly. Zircon standard AS3 (1099 ± 1 Ma, Paces & Miller, 1993) was used as a calibration standard. All measurements were made using the Cameca ims1270 ion microprobe facility at the University of California, Los Angeles, USA. Results are reported with 1σ errors, except for weighted mean ages that have 2σ errors (Table 4.4). The U-Pb measurements were made with an O^- beam according to the methods of Breeding et al. (2004) for the depth-profiling of unpolished crystals and Schmitt et al. (2003) for analyses of polished AS3 grains. U-Pb isotopic ratios and ages were calculated from measured ion intensities using in-house software written by C.D. Coath (ZIPS v3.0); Isoplot v3.0 (Ludwig, 2003) was used to plot $^{206}Pb/^{238}U$ weighted distribution diagram. We chose to report

the ages as weighted distribution diagram due to the high ion counts and ^{206}Pb radiogenic yields from these analyses (Fig. 4.4). A statistically rigorous assessment of U-Pb concordance is hampered by low ion intensities of ^{207}Pb, and a poor ^{207}Pb radiogenic yield (generally 50-90%) causing calculated $^{207}Pb/^{235}U$ ratios to be highly sensitive to corrections for common Pb. Nevertheless, no obvious signs of U-Pb discordance are observed.

The aim of this technique was to constrain the age of the anatectic event which should have been recorded in the leucosome zircons and not in the melanosome ones. Because zircons are often zoned, preserving a memory of all thermal events since their crystallization, we used a depth-profiling technique in order to distinguish between the rim and core of the analyzed zircons. We expected to find an age-depth relationship in the zircons but the age was homogeneous throughout each sample. Eleven leucosome (ZT-01-09B) and five melanosome (ZT-01-09A) zircons were analyzed. The melanosome zircon single-spot analyses ages spread from 360 ± 10 to 324 ± 8 Ma and yield a weighted mean $^{206}Pb/^{238}U$ age of 358 ± 17 Ma (MSWD: 1.8) while the leucosome zircon single spot ages spread from 374 ± 10 to 341 ± 9 Ma and gave a weighted mean $^{206}Pb/^{238}U$ age of 347 ± 7 Ma (MSWD: 1.4). Since both ages are within error, they may represent a single zircon population in which case the weighted average $^{206}Pb/^{238}U$ age is 351 ± 5 Ma (MSWD: 0.71). Because both zircon populations contain older, xenocrystic grain morphologies and younger neogrowth, it appears that a distinction in two age populations may be credible. At the 1.5% reproducibility of the SIMS technique, it is difficult to confidently resolve between two populations 10 m.y. apart in the Paleozoic age range; further work could resolve this issue.

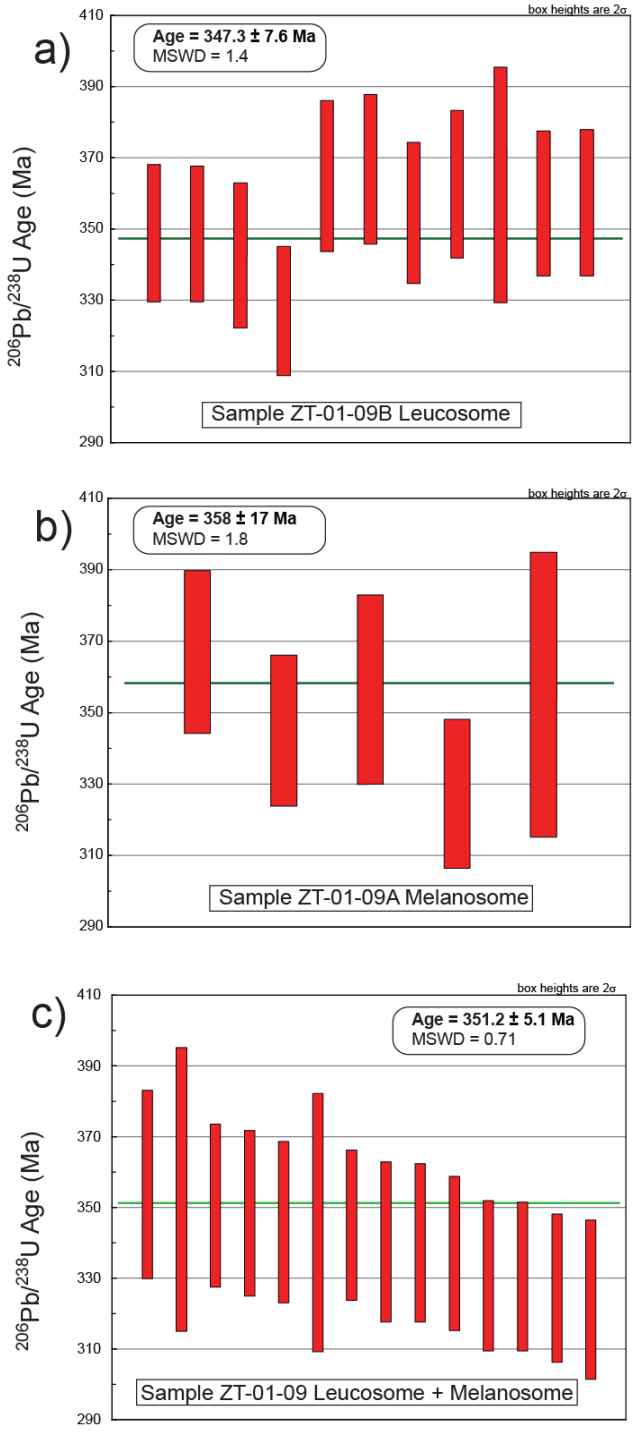

Figure 4.4: Weighted mean $^{206}Pb/^{238}U$ age diagram from ion-probe analyses for: (a) zircons from the anatectic leucosome of migmatite (ZT-01-09B); (b) zircons from the melanosome part of the migmatites (ZT-01-09A); and (c) both zircon populations treated as if part of a single population. Red vertical boxes represent error for single zircons analysis.

Analysis	206Pb/ 238U	1 std err (%)	207Pb/ 235U	1 std err (%)	207Pb/ 206Pb	1 std err (%)	U O/U	Th/U	U (ppm)	Th (ppm)	Radiogenic 206Pb (%)	Radiogenic 207Pb (%)	Correlation coefficient	206Pb/ 238U (Ma)	1 std err abs
ZT-01-09-B (Leucosome)_1	0.05482	0.00145	0.37760	0.01519	0.04996	0.00146	9.11	0.025	340.5	9.5	98.5	80.2	0.687	344.0	8.9
ZT-01-09-B (Leucosome)_2	0.05478	0.00143	0.34690	0.03049	0.04593	0.00367	9.16	0.086	321.8	30.6	96.1	57.8	0.440	343.8	8.8
ZT-01-09-B (Leucosome)_3	0.05388	0.00153	0.34340	0.02162	0.04622	0.00259	9.18	0.117	336.7	43.3	98.5	78.1	0.454	338.3	9.4
ZT-01-09-B (Leucosome)_4	0.05153	0.00136	0.28540	0.02229	0.04017	0.00290	9.31	0.093	398.2	41.1	97.7	67.5	0.381	323.9	8.3
ZT-01-09-B (Leucosome)_5	0.05722	0.00160	0.40920	0.02247	0.05187	0.00229	8.93	0.146	353.4	56.1	97.0	67.1	0.605	358.7	9.7
ZT-01-09-B (Leucosome)_6	0.05752	0.00158	0.38490	0.02789	0.04854	0.00313	9.06	0.047	342.2	17.9	97.5	69.9	0.464	360.5	9.6
ZT-01-09-B (Leucosome)_7	0.05567	0.00149	0.37540	0.01514	0.04890	0.00145	9.16	0.024	337.5	9.0	99.2	88.2	0.677	349.2	9.1
ZT-01-09-B (Leucosome)_8	0.05688	0.00156	0.38710	0.01759	0.04937	0.00178	8.94	0.019	618.8	13.4	99.0	84.9	0.608	356.6	9.5
ZT-01-09-B (Leucosome)_9	0.05686	0.00249	0.35540	0.21360	0.04533	0.02625	9.19	0.278	322.1	98.9	78.0	16.1	0.530	356.5	15.2
ZT-01-09-B (Leucosome)_10	0.05608	0.00153	0.36480	0.03705	0.04718	0.00441	9.10	0.038	275.0	11.6	91.0	36.5	0.420	351.7	9.3
ZT-01-09-B (Leucosome)_11	0.05611	0.00155	0.37570	0.01709	0.04857	0.00161	9.10	0.153	284.1	47.9	98.8	82.6	0.692	351.9	9.4
ZT-01-09-A (Melanosome)_1	0.05978	0.00157	0.41730	0.01628	0.05063	0.00144	9.13	0.015	1546.3	24.1	96.9	66.0	0.684	374.3	9.6
ZT-01-09-A (Melanosome)_2	0.05677	0.00145	0.38750	0.01273	0.04950	0.00098	9.22	0.023	1108.3	28.0	99.3	90.1	0.799	355.9	8.8
ZT-01-09-A (Melanosome)_3	0.05833	0.00182	0.39340	0.11800	0.04892	0.01400	9.18	0.016	1628.8	28.7	92.3	41.4	0.482	365.5	11.1
ZT-01-09-A (Melanosome)_4	0.05432	0.00143	0.37870	0.03077	0.05055	0.00374	9.12	0.026	1042.7	30.4	97.9	73.9	0.425	341.0	8.7
ZT-01-09-A (Melanosome)_5	0.05813	0.00274	0.45040	0.05560	0.05619	0.00485	9.13	0.017	1600.0	30.0	99.0	86.4	0.861	364.3	16.7

Table 4.4: Summary of SIMS U-Pb isotopic data from migmatite zircons (sample ZT-01-09)

4.3. U-Pb monazite geochronology

To assist in constraining the timing of metamorphism of the basement sequence, we conducted U-Pb geochronology on monazite from the migmatites of the upper structural unit. Monazites from two migmatite samples (ZT-12-08, ZT-08-09) were analyzed in situ from 100 μm thick rock sections. Sample ZT-12-08 was selected because it was also used for the P-T constraint work while sample ZT-08-09 was selected because of its location a few meters away from the eclogite outcrop. The samples were analyzed by laser ablation inductively-coupled plasma mass spectrometer (LA-ICPMS) consisting of a New Wave Nd:YAG 213 nm laser coupled to a quadrupole Thermo X Series 2 ICPMS at the Department of Earth Sciences, Laurentian University, Canada. The ablation was done in a He atmosphere and Ar was mixed to the carrier gas before it entered the ICPMS. We used a 30 μm spot and a repetition rate of 10 Hz for the analysis. Energy density was kept constant at about 6 to 7J/cm^2 and the beam width is 5 ns. Analysis time ranged between 50-60 seconds, including 30 seconds background acquisition. We used the 91500 zircon standard with a U-Pb age of 1065.4 ± 0.6 Ma (e.g. Wiedenbeck et al., 1995 and Yuan et al., 2004) for external calibration. The data were corrected for common Pb by using the correction routine in Andersen (2001) and the results are plotted using Isoplot v3 (Ludwig, 2003).

Monazite is an accessory mineral that can form during metamorphism and is therefore widely used to date metamorphic events (e.g. Catlos et al., 2002). In polymetamorphosed terranes it offers the advantage of being easily recrystallized and therefore several metamorphic pulses of different intensity can be recorded by different monazite populations. The obvious drawback is that no quantitative temperature information on the dated thermal event can be deduced. In both samples most monazites were located in the melanosome part of the

migmatites, often included in biotite crystals. All monazites were imaged by SEM before analysis and only large grains with sharp edges and no visible zoning were selected. Few monazite were present as inclusion within garnet grains, however their small size (<30 μm) prevented any accurate laser analysis. Eleven monazite grains were analyzed from sample ZT-12-08 (Table 4.5) and yielded two distinct age populations (Fig. 4.5). The oldest and most prominent age is at 340 ± 11 Ma (n: 7, MSWD: 0.92) while the second population gave an age of 300 ± 16 Ma (n: 4, MSWD: 1.4). Another 13 monazites were analysed from sample ZT-08-09 and concentrate into one population at ca. 380 Ma. Figure 4.6 shows three isochron plots of the monazite analysis from sample ZT-08-09; a) $^{238}U/^{206}Pb$ isochron with monazite grains n°23 and 88 removed giving ages of 385 ± 6 Ma (n: 11, MSWD: 1.4), b) $^{235}U/^{207}Pb$ isochron with all analysed monazite grains giving an age of 383 ± 7 Ma (n: 13, MSWD: 1.2), c) $^{232}Th/^{208}Pb$ isochron with monazite grains n°23, 70, 88 and 8 removed giving an age of 378 ± 18 Ma (n: 9, MSWD: 2.9). Few monazite grains were removed in two of these plots since the data points were falling off the main regression line.

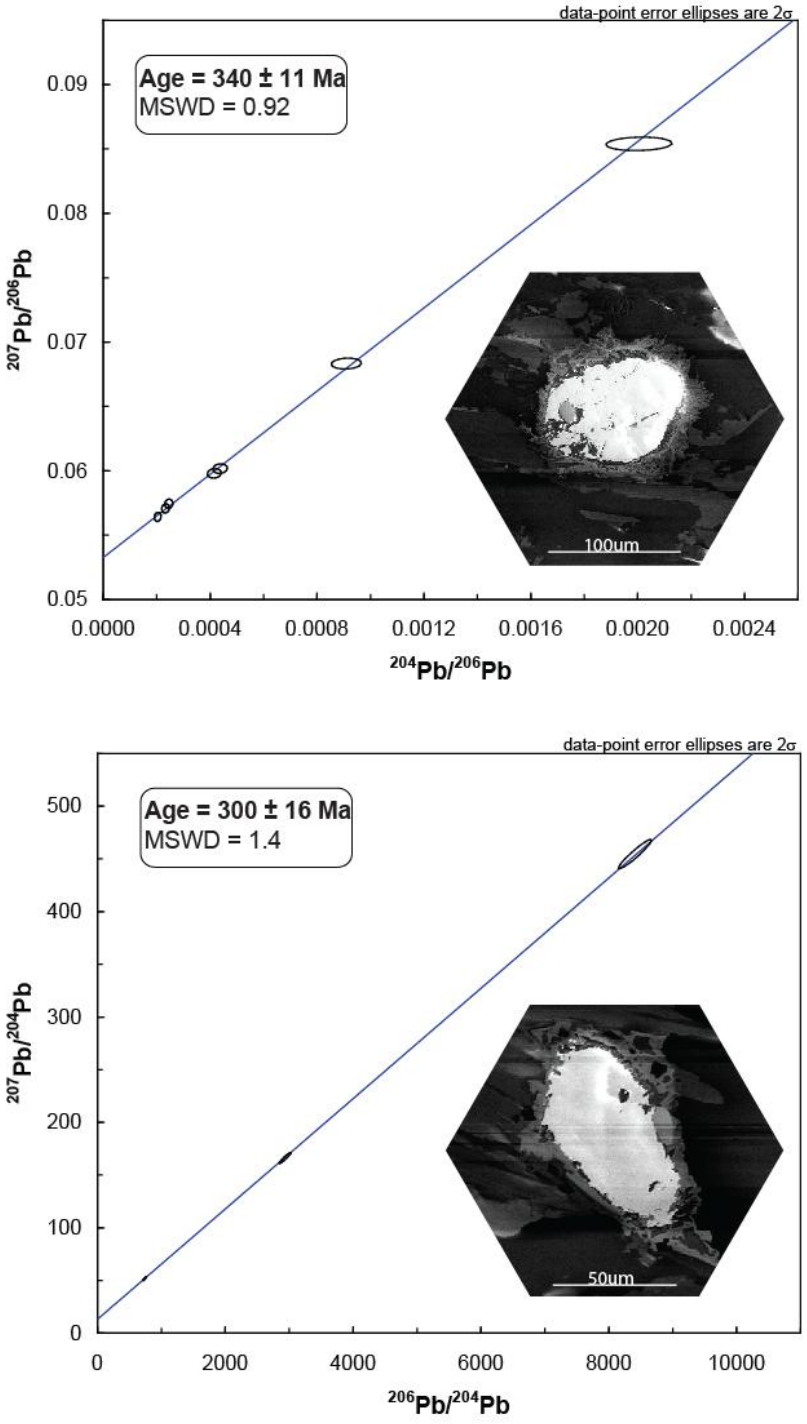

Figure 4.5: Pb-Pb isochron plots of the monazite LA-ICPMS analysis from sample ZT-12-08 (upper unit migmatites). (a) Inverse ^{207}Pb-^{206}Pb isochron for the oldest monazite population (n: 7). (b) ^{207}Pb-^{206}Pb isochron for the younger monazite population (n: 4). Lower right insets are SEM photomicrograph of representative monazites crystals.

Analysis	$^{207}Pb/^{206}Pb$	2σ	$^{206}Pb/^{204}Pb$	2σ	$^{207}Pb/^{204}Pb$	err	$^{204}Pb/^{206}Pb$	err	$^{207}Pb/^{206}Pb$	2σ
Sample ZT-12-08 older grains										
Monazite 1	0.0601642	0.0014493	2288.7300000	460.3410000	137.6996095	460.3410000	0.0004369	0.0021723	0.0601642	0.0014493
Monazite 1, spot 2	0.0853968	0.0031936	498.6530000	38.5950000	42.5833705	38.5950001	0.0020054	0.0259101	0.0853968	0.0031936
Monazite 3	0.0570810	0.0009333	4303.7800000	1373.5400000	245.6640662	1373.5400000	0.0002324	0.0007280	0.0570810	0.0009333
Monazite 5	0.0683304	0.0018151	1099.3200000	109.6310000	75.1169753	109.6310000	0.0009097	0.0091215	0.0683304	0.0018151
Monazite 7	0.0598047	0.0017818	2409.0300000	278.8360000	144.0713164	278.8360000	0.0004151	0.0035863	0.0598047	0.0017818
Monazite 8	0.0564245	0.0013922	4918.4400000	1617.0400000	277.5205178	1617.0400000	0.0002033	0.0006184	0.0564245	0.0013922
Monazite 10	0.0574342	0.0014521	4086.0700000	1697.1600000	234.6801616	1697.1600000	0.0002447	0.0005892	0.0574342	0.0014521
Sample ZT-12-08 yonger grains										
Monazite 11	0.0566101	0.0007873	2935.8100000	335.9670000	166.1964977	335.9670000	0.0003406	0.0029765	0.0566101	0.0007873
Monazite 11, spot 2	0.0701793	0.0042024	738.3850000	106.6350000	51.8193424	106.6350001	0.0013543	0.0093778	0.0701793	0.0042024
Monazite 9	0.0540496	0.0012217	8409.9800000	1417.1100000	454.5560550	1417.1100000	0.0001189	0.0007057	0.0540496	0.0012217
Monazite 2	0.1075840	0.0052080	263.4060000	24.5785000	28.3382711	24.5785006	0.0037964	0.0406860	0.1075840	0.0052080

Analysis	$^{206}Pb/^{204}Pb$	2σ	$^{238}U/^{204}Pb$	2σ	$^{207}Pb/^{204}Pb$	2σ	$^{235}U/^{204}Pb$	2σ	$^{232}Th/^{204}Pb$	2σ
Sample ZT-08-09										
Monazite 1	236.5843892	4.7316878	3024.1398024	120.9655921	27.6311298	1.3815565	21.9331288	0.8773252	28750.9589965	1150.0383599
Monazite 18	2748.2297540	54.9645951	43507.5523611	1740.3020944	160.3114942	8.0155747	315.5465068	12.6218603	392481.8054017	15699.2722161
Monazite 25	389.8127057	7.7962541	5573.3506892	222.9340276	34.9549673	1.7477484	40.4217485	1.6168699	64496.9811553	2579.8792462
Monazite 3	1795.2180599	35.9043612	26804.8104260	1072.1924170	101.6100531	5.0805027	194.4068061	7.7762722	207097.3853869	8283.8954155
Monazite 32	3724.1293162	74.4825863	59757.1410744	2390.2856430	216.3711138	10.8185557	433.3996307	17.3359852	536108.8658883	21444.3546355
Monazite 35	3307.7447548	66.1548951	54262.6395089	2170.5055804	187.5996980	9.3799849	393.5497498	15.7419900	453490.0020299	18139.6000812
Monazite 44	4786.2788939	95.7255779	78843.1201986	3153.7248079	281.1298070	14.0564904	571.8241964	22.8729679	642448.6551360	25697.9462054
Monazite 46	8042.0618401	160.8412368	129746.1041343	5189.8441654	442.5280428	22.1264021	941.0074277	37.6402971	996145.6750066	39845.8270003
Monazite 89	1719.7920118	34.3958402	28204.4768600	1128.1790744	108.7905685	5.4395284	204.5581437	8.1823257	186491.2649494	7459.6505980
Monazite 23	4133.2415316	82.6648306	62179.6085088	2487.1843404	235.2000956	11.7600048	450.9690202	18.0387608	319356.9083630	12774.2763345
Monazite 70	7289.9722546	145.7994451	115524.8420031	4620.9936801	415.5095139	20.7754757	837.8651146	33.5146046	836353.5337092	33454.1413484
Monazite 88	3715.0983817	74.3019676	54415.7046656	2176.6281866	208.8886101	10.4444305	394.6598830	15.7863953	458586.5709024	18343.4628361
Monazite 8	9206.0044206	184.1200884	148701.9301178	5948.0772047	511.3616487	25.5680824	1078.4880339	43.1395214	1112209.7953199	44488.3918128

Table 4.5: Summary of the LA-ICPMS U-Pb isotopic data from migmatite monazites (sample ZT-12-08 and ZT-08-09)

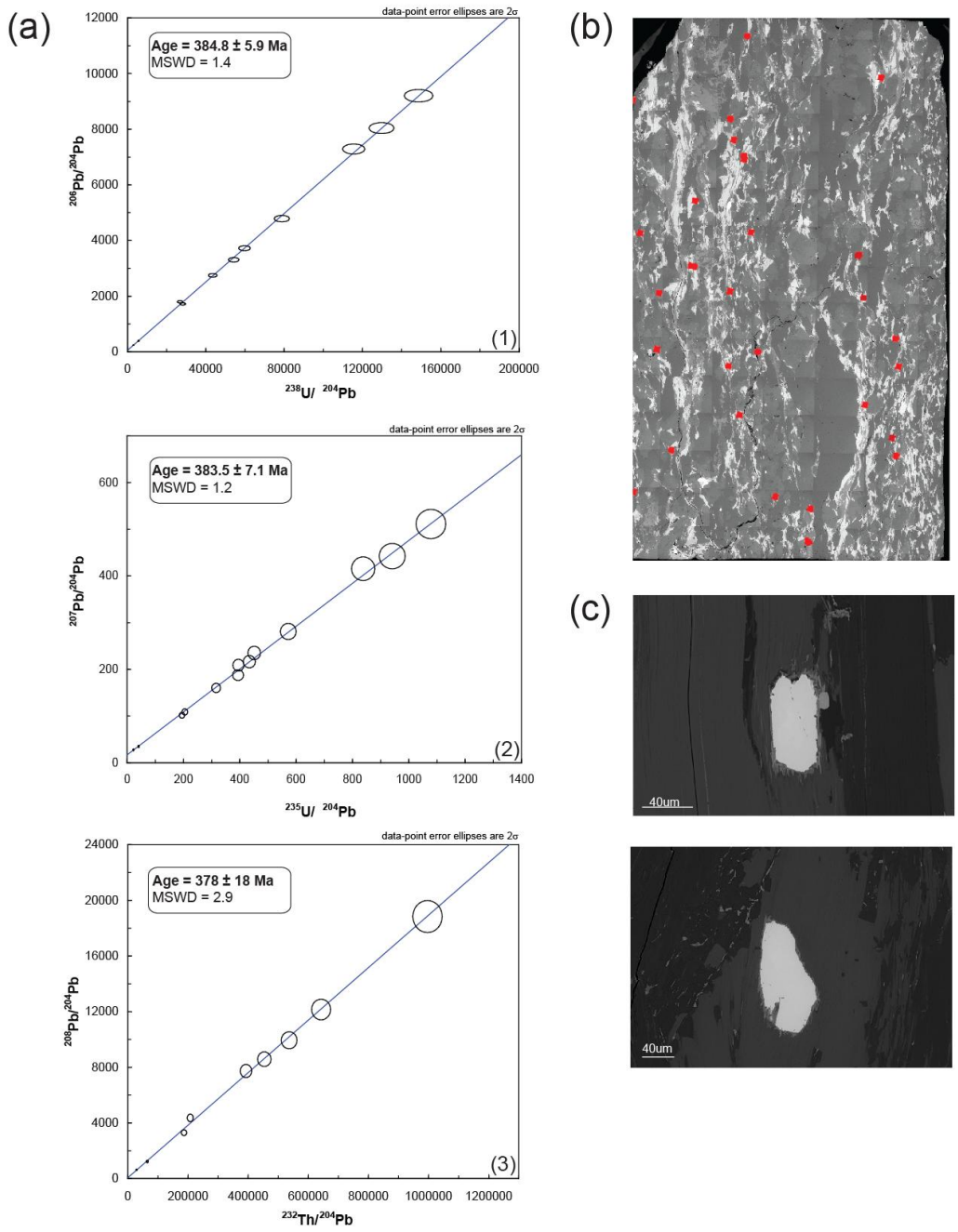

Figure 4.6: (a) Pb-Pb isochron plots of the monazite LA-ICPMS analysis from sample ZT-08-09 (upper unit migmatites). (1) $^{238}U/^{206}Pb$ isochron with monazite grains n°23 and 88 removed (n: 11). (2) $^{235}U/^{207}Pb$ isochron with all analysed monazite grains (n: 13). (3) ^{232}Th-^{208}Pb isochron with monazite grains n°23, 70, 88 and 8 removed (n: 9). (b) Reconstructed SEM scan of sample ZT-08-09 thick section showing (red squares) the emplacement of all monazites. Note that all monazites are contained within biotite crystals. (c) Representative SEM photomicrograph of monazite crystals. Note that monazites are aligned along the main fabric.

4.4. $^{40}Ar/^{39}Ar$ thermochronology

In order to constrain the timing of the lower temperature cooling evolution of the basement sequence, we conducted $^{40}Ar/^{39}Ar$ thermochronology studies on micas from the lower unit micashists and upper unit migmatites. Biotite and muscovite were handpicked from the micaschist (ZT-03-08; ZT-14-08; ZT-21-08; ZT-26-08) and migmatites (ZT-08-08 and ZT-12-08) units and hornblende was handpicked from the amphibolites (ZT-05-08; ZT-10-08 and ZT-17-08). These mineral separates of 99% purity (size fractions of >150 μm) were loaded into machined Al discs and irradiated with flux monitor Fish Canyon Tuff sanidine (28.02 Ma; Renne et al., 1998) for 10 hours in the central thimble at the 1 MW TRIGA Reactor at the USGS, Denver, USA. In the nuclear reactor a small portion of the ^{39}K was transformed to ^{39}Ar through interaction with fast neutron. The sample was then heated in steps in an ultrahigh vacuum system at the New Mexico Institute of Mining and Technology Geochronology Laboratory, USA. The argon extracted at each step was purified and analyzed isotopically using a MAP 215-50 mass spectrometer on line with an automated all-metal extraction system. The flux monitor crystals (in a copper planchet) were fused with a 50W Synrad CO_2 continuous laser within an ultrahigh vaccum argon extraction system. Evolved gases were purified using two SAES GP-50 getter (one at 450 °C, one at 20 °C). J-factors were determined to a precision of 0.1% (2σ) by analyzing a minimum of four single crystal aliquots from each radial position around the irradiation sample trays. The unknown minerals were step-heated in a double-vacuum Mo resistance furnace while the glass samples were step-heated using a defocused CO_2 laser. Argon isotopic compositions were determined using an electron multiplier with an overall sensitivity of $8x10^{-17}$ moles/pA for the furnace and $4.5x10^{-17}$ moles/pA for the laser. Routine measurement of the extraction system,

mass spectrometer blanks, and backgrounds took place throughout the course of the analyses. Errors are reported at the 2σ confidence level. The results are presented in table 4.6 and as spectra (Fig. 4.7) where the width of each bar (thermal increment) represents the proportion of evolved gas, and the height represents the uncertainty associated with the apparent age. The integrated age is an average cooling age for the sample calculated by summing the isotopic measurements of all steps with an uncertainty calculated by quadratically combining errors of isotopic measurements of all steps. Plateau ages are defined for this investigation as the portion of an age spectrum composed of contiguous increments representing >70% of gas released which result in concordant ages (Mahon, 1996).

Unfortunately none of the obtained Ar release spectra displayed a plateau age; ages reported are therefore integrated ages. Hornblendes age spectra show integrated ages varying from 418 to 542 Ma with no plateau age, low K/Ca ratio and large variation between each incremental Ar release. The quality of these data is very poor and could results from complex mixture of probably inherited or excess Ar. We therefore believe these hornblende results to be unreliable and un-interpretable. The biotite age spectra show integrated ages varying from 144 to 243 Ma with no plateau ages. A saddle-shaped in the Ar step release is weakly defined but consistent in almost all spectra excepted ZT-14-08 and ZT-26-08 which record the youngest ages. From a spatial perspective (Fig. 3.2) it appears that integrated biotite ages are younger toward the north. From the K/Ca spectra it appears that the three increments in all biotite Ar spectra are from degassing of a low potassium phase and not from biotite. The consistent low K/Ca ratios throughout the degassing process for sample ZT-12-08 indicate that the degassed biotite might contain a large chlorite component. Muscovite age spectra yield integrated ages varying from 250 to 310 Ma with again no defined plateau ages. A saddle-shaped in the Ar step

release is strongly defined in all spectra. From a spatial perspective (Fig. 3.2) integrated muscovite ages are seemingly older toward the east. The saddle-shape present in both biotite and muscovite Ar spectras might results from a mixture of several populations of micas defining a retentive and a less-retentive reservoir of Ar (Foster & Lister, 2004). From petrographic observations the two muscovite and biotite populations can be seen at the thin section scale with earlier micas often found at an angle to the main foliation and enclosed within plagioclase and quartz crystals. From figure 3.3 it is clear that two generations of biotite coexist, one found in the pressure shadow of garnet crystals and on defining the main foliation and wrapping around the first one. For the biotite, the retentive population has an apparent maximum age between 200 and 260 Ma while for the muscovite the retentive population has an apparent maximum age between 280 and 335 Ma. The cooling ages of the younger biotite and muscovite population would need further diffusion modeling analysis to be resolved.

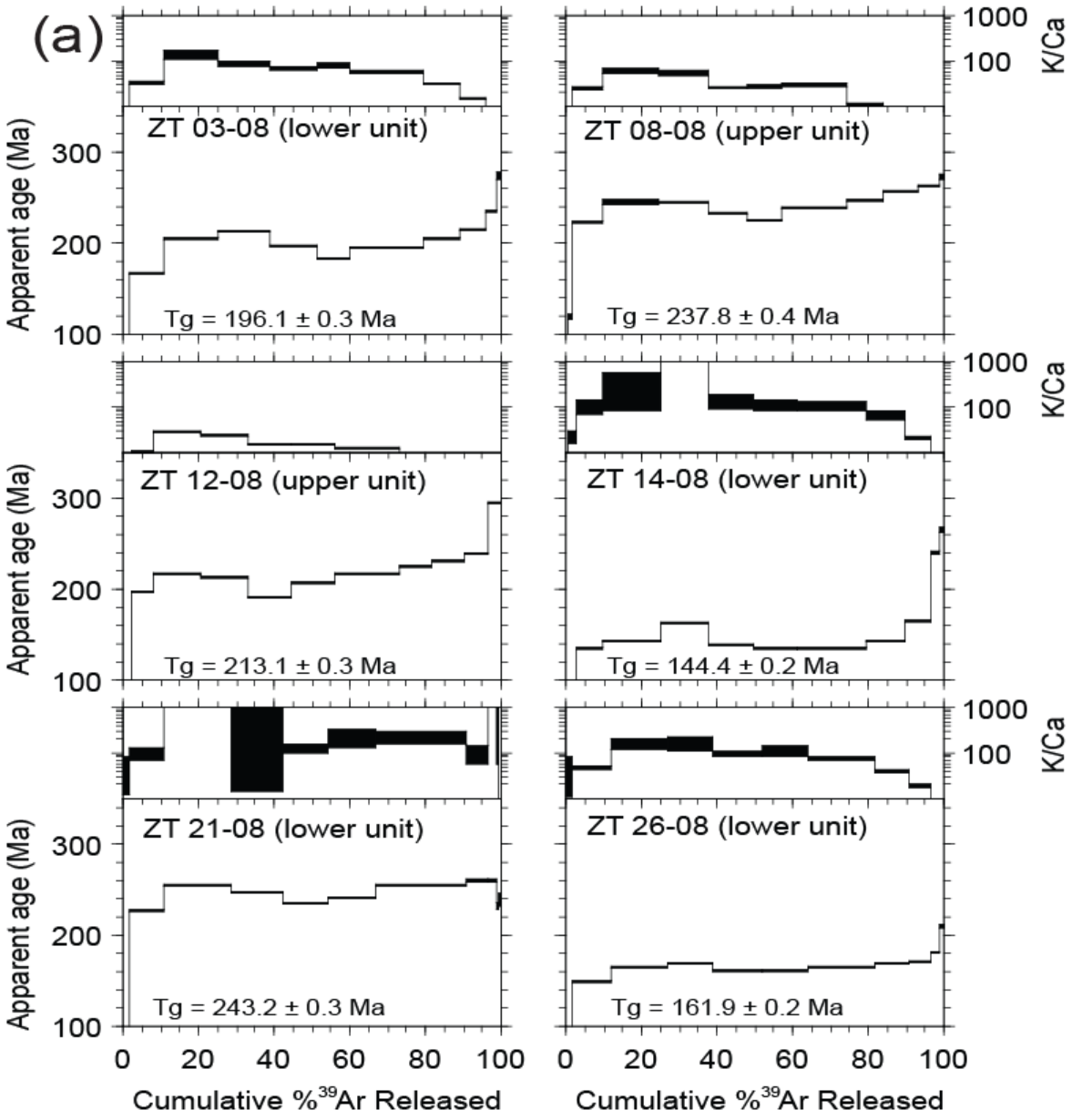

Figure 4.7: $^{40}Ar/^{39}Ar$ spectra for a) biotite from migmatites (upper unit) and micashist (lower unit); b) hornblende from amphibolites (upper unit); c) muscovite from micashist (lower unit).

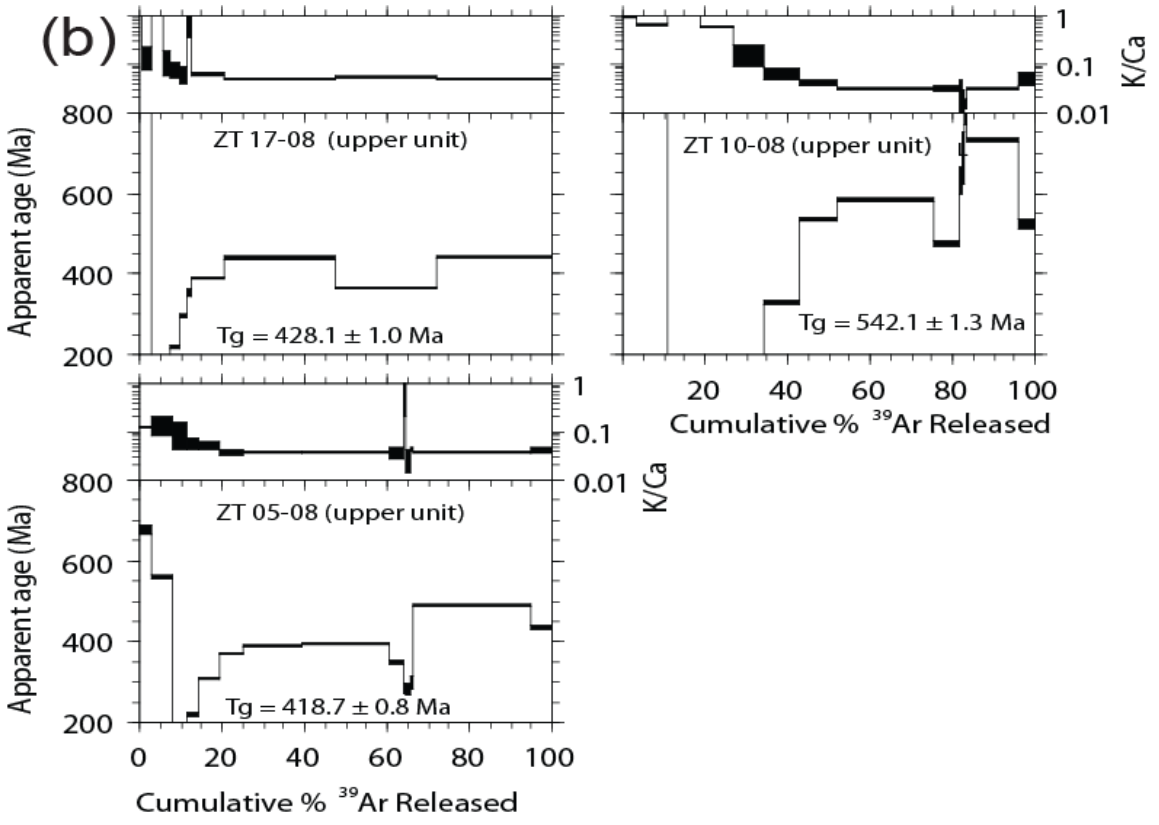
(b)
ZT 17-08 (upper unit)
Tg = 428.1 ± 1.0 Ma
ZT 10-08 (upper unit)
Tg = 542.1 ± 1.3 Ma
ZT 05-08 (upper unit)
Tg = 418.7 ± 0.8 Ma
Apparent age (Ma)
K/Ca
Cumulative % 39Ar Released

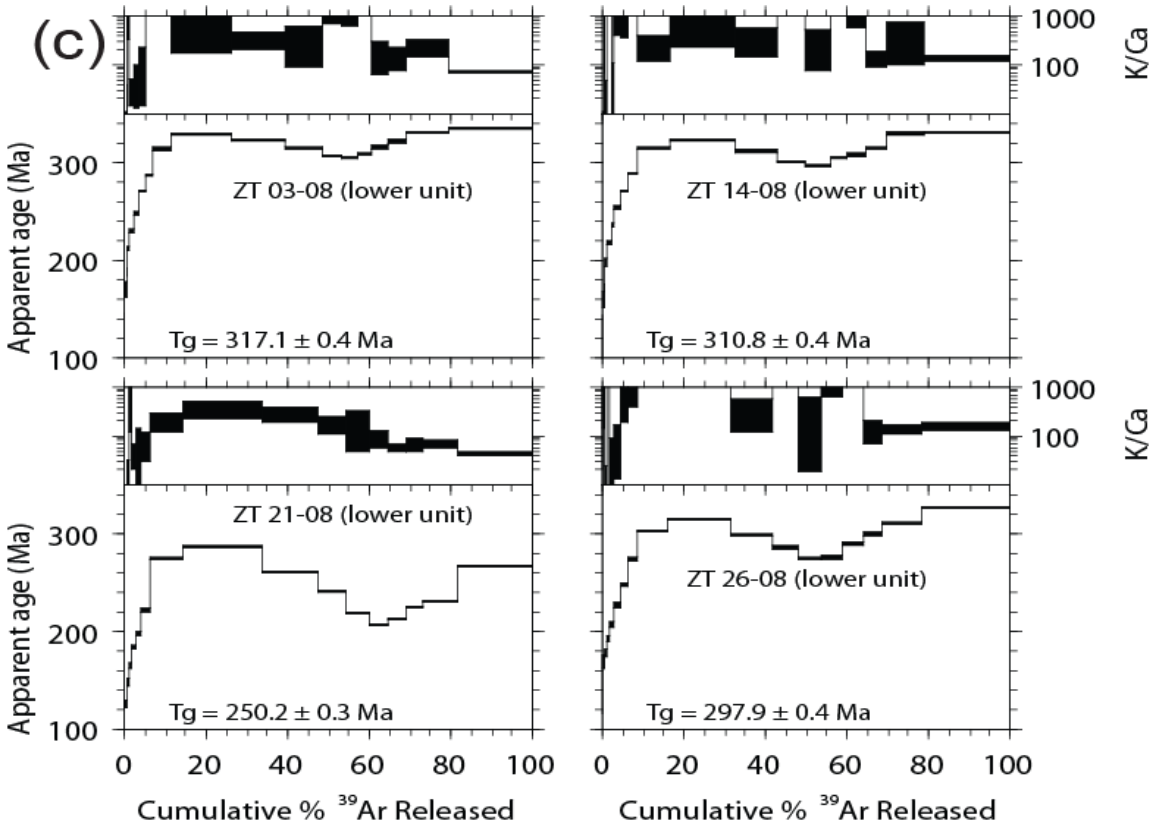
(c)
ZT 03-08 (lower unit)
Tg = 317.1 ± 0.4 Ma
ZT 14-08 (lower unit)
Tg = 310.8 ± 0.4 Ma
ZT 21-08 (lower unit)
Tg = 250.2 ± 0.3 Ma
ZT 26-08 (lower unit)
Tg = 297.9 ± 0.4 Ma
Apparent age (Ma)
K/Ca
Cumulative % 39Ar Released

ID	Temp	$^{40}Ar/^{39}Ar$	$^{37}Ar/^{39}Ar$	$^{36}Ar/^{39}Ar$	$^{39}Ar_K$	K/Ca	$^{40}Ar^*$	^{39}Ar	Age	±1s
	(°C)			(x 10^{-3})	x 10^{-15} mol)		(%)	(%)	(Ma)	(Ma)
ZT 03-08, Muscovite, 3.65 mg, J=0.0023612±0.07%,										
A	580	70.68	0.1003	166.743	0.42	5.09	30.33	0.30	89.06	3.88
B	630	47.53	0.0773	31.458	0.19	6.60	80.46	0.43	155.93	5.68
C	680	46.79	0.0817	18.197	0.26	6.25	88.52	0.61	168.31	4.01
D	730	50.68	0.0252	15.285	0.54	20.25	91.09	0.99	186.61	2.26
E	780	55.84	0.0053	11.062	0.97	96.93	94.15	1.68	211.05	1.33
F	810	59.46	0.0163	7.293	1.16	31.29	96.38	2.50	228.90	1.17
G	840	64.75	0.0093	9.173	1.46	54.76	95.81	3.54	246.60	1.08
H	880	71.14	0.0046	9.290	2.46	111.59	96.14	5.28	270.03	0.89
I	900	74.70	0.0013	6.445	2.90	405.73	97.45	7.33	286.11	0.88
J	930	82.74	0.0012	8.264	6.30	441.16	97.05	11.80	313.18	0.65
K	960	85.38	0.0008	3.298	20.92	622.88	98.86	26.63	327.83	0.54
L	990	83.23	0.0015	1.073	18.14	332.27	99.62	39.48	322.53	0.57
M	1020	80.93	0.0014	1.554	12.89	352.03	99.43	48.62	313.80	0.52
N	1040	78.94	0.0016	2.149	6.93	318.94	99.20	53.53	306.03	0.62
O	1070	78.53	0.0019	2.454	5.66	270.64	99.08	57.54	304.23	0.60
P	1100	79.69	0.0002	2.911	4.93	2633.99	98.92	61.03	307.92	0.64
Q	1140	81.53	0.0030	2.247	5.33	168.79	99.19	64.81	315.21	0.68
R	1180	83.26	0.0034	2.630	6.35	149.51	99.07	69.31	320.98	0.59
S	1250	85.75	0.0022	2.248	14.44	228.20	99.23	79.54	330.25	0.56
T	1650	86.44	0.0073	1.918	28.86	70.10	99.35	100.00	333.05	0.49
Integrated age ± 2s			n=20		141.11	139.11		K2O=6.29%	317.12	0.80
ZT 21-08, Muscovite, 2.75 mg, J=0.0022895±0.08%,										
A	580	187.27	0.9495	617.107	0.03	0.54	2.71	0.02	20.87	40.65
B	630	48.91	0.2933	102.500	0.14	1.74	38.15	0.15	75.48	7.56
C	680	43.03	0.2330	62.013	0.09	2.19	57.46	0.24	99.32	9.85
D	730	33.33	0.1318	20.822	0.20	3.87	81.58	0.42	108.94	4.76
E	780	33.79	0.0893	8.629	0.44	5.71	92.48	0.83	124.63	2.26
F	810	41.01	0.0273	14.067	0.54	18.67	89.87	1.33	146.13	2.03
G	840	44.21	0.0108	9.356	0.67	47.15	93.75	1.95	163.52	1.58
H	880	50.60	0.0116	14.111	1.27	43.90	91.76	3.11	182.24	1.10
I	900	54.00	0.0070	12.775	1.46	73.32	93.01	4.46	196.32	0.96
J	930	60.55	0.0072	11.727	2.58	71.20	94.28	6.83	221.56	0.85
K	960	73.40	0.0025	5.387	8.58	203.54	97.83	14.73	274.56	0.51
L	990	75.60	0.0014	1.257	21.24	368.86	99.51	34.26	286.65	0.51
M	1020	68.08	0.0018	1.053	14.52	287.24	99.54	47.62	260.17	0.39
N	1040	62.54	0.0029	1.078	7.58	174.65	99.49	54.60	240.24	0.45
O	1070	56.38	0.0028	1.374	6.07	183.15	99.28	60.18	217.51	0.50
P	1100	53.48	0.0057	1.890	4.80	89.45	98.96	64.59	206.30	0.42
Q	1140	55.17	0.0093	2.226	5.08	55.09	98.81	69.26	212.14	0.48
R	1180	58.11	0.0075	2.091	4.82	68.32	98.94	73.70	223.05	0.52
S	1250	59.89	0.0077	2.094	9.02	66.52	98.97	81.99	229.56	0.37
T	1650	70.02	0.0127	1.777	19.58	40.02	99.25	100.00	266.36	0.54
Integrated age ± 2s			n=20		108.72	72.59		K2O=6.63%	250.19	0.68
ZT 14-08, Muscovite, 3.23 mg, J=0.0023083±0.06%,										
A	580	58.66	0.0855	124.944	0.40	5.96	37.09	0.30	88.39	3.40
B	630	51.50	0.0698	42.267	0.18	7.31	75.76	0.43	155.55	5.84
C	680	44.64	0.0786	15.657	0.25	6.49	89.65	0.62	159.36	4.18
D	730	44.61	0.0171	5.123	0.48	29.92	96.61	0.97	171.05	2.07
E	780	51.82	0.0193	6.218	0.86	26.48	96.46	1.61	196.98	1.66
F	810	57.61	0.0016	7.280	1.01	311.21	96.27	2.36	217.27	1.31
G	840	62.87	0.0099	8.861	1.22	51.55	95.84	3.26	234.90	1.32
H	880	68.38	0.0035	10.766	2.05	145.43	95.35	4.79	252.89	1.00
I	900	73.29	0.0033	11.250	2.19	154.30	95.46	6.41	270.07	0.91
J	930	77.91	0.0010	9.818	3.58	503.11	96.28	9.06	288.04	0.78
K	960	84.81	0.0021	8.961	10.18	244.98	96.88	16.61	313.28	0.58
L	990	85.46	0.0009	2.293	22.18	578.92	99.21	33.04	322.42	0.51
M	1020	81.87	0.0015	1.179	13.92	347.93	99.57	43.35	311.04	0.53
N	1040	79.23	0.0004	2.107	9.04	1298.89	99.21	50.05	300.78	0.55
O	1070	77.70	0.0017	2.137	8.28	293.69	99.19	56.18	295.34	0.51
P	1100	80.33	-0.0001	2.824	5.73	-	98.96	60.42	303.92	0.61
Q	1140	81.06	0.0019	2.625	6.08	271.28	99.04	64.92	306.69	0.67
R	1180	82.97	0.0039	2.430	7.03	132.09	99.13	70.13	313.58	0.67
S	1250	87.24	0.0013	1.550	12.55	399.53	99.48	79.42	329.38	1.16
T	1650	87.30	0.0039	1.579	27.78	130.40	99.47	100.00	329.54	0.56
Integrated age ± 2s			n=20		135.00	188.71		K2O=6.95%	310.85	0.78

ZT 26-08, Muscovite, 3.23 mg, J=0.0023188±0.07%,

A	580	78.31	0.1311	179.285	0.22	3.89	32.40	0.21	103.11	6.35
B	630	59.40	0.2136	30.677	0.10	2.39	84.77	0.30	199.24	12.31
C	680	46.18	0.0551	12.932	0.16	9.26	91.74	0.45	169.05	7.28
D	730	45.54	0.0118	12.045	0.37	43.14	92.19	0.80	167.55	3.68
E	780	46.25	0.0317	6.321	0.65	16.09	95.97	1.40	176.70	2.10
F	810	50.39	0.0009	6.173	0.83	559.74	96.38	2.18	192.49	1.61
G	840	54.91	0.0115	8.551	1.05	44.36	95.40	3.16	206.79	1.57
H	880	60.65	0.0057	10.615	1.68	89.91	94.83	4.73	225.81	1.17
I	900	65.93	-0.0025	8.996	1.76	-	95.97	6.37	246.94	1.32
J	930	72.73	0.0030	7.584	2.82	170.44	96.92	9.01	273.08	0.91
K	960	80.59	0.0007	5.991	7.80	716.08	97.80	16.30	302.78	0.54
L	990	82.41	0.0006	1.861	16.22	895.57	99.33	31.45	313.51	0.55
M	1020	77.66	0.0015	1.104	11.22	336.12	99.58	41.94	297.53	0.50
N	1040	74.17	0.0003	1.210	6.62	1976.77	99.52	48.13	285.00	0.59
O	1070	71.53	0.0016	2.368	5.99	314.67	99.02	53.72	274.31	0.54
P	1100	71.62	0.0018	1.873	5.73	276.59	99.23	59.07	275.14	0.68
Q	1140	75.48	0.0011	1.800	5.38	467.05	99.30	64.11	289.06	0.64
R	1180	78.23	0.0037	1.745	4.90	136.31	99.34	68.69	298.87	0.74
S	1250	81.42	0.0038	2.072	10.74	133.14	99.25	78.73	309.81	0.51
T	1650	85.72	0.0034	1.511	22.76	151.05	99.48	100.00	325.49	0.54
Integrated age ± 2s			n=20		107.00	177.75		K2O=5.49%	297.94	0.75

ZT 17-08, Hornblende, 13.52 mg, J=0.0023114±0.06%,

A	900	1014.80	0.3775	1880.307	0.30	1.35	45.25	0.91	1305.35	16.81
B	1000	444.47	3.6287	242.787	0.80	0.14	83.93	3.34	1123.83	5.27
C	1050	36.71	0.3889	11.470	0.79	1.31	90.86	5.75	134.00	1.70
D	1080	40.14	4.3774	9.153	0.67	0.12	94.17	7.77	151.52	1.89
E	1100	58.09	6.7184	10.926	0.65	0.08	95.40	9.75	218.37	2.05
F	1110	79.03	8.4024	12.656	0.55	0.06	96.15	11.43	293.46	2.95
G	1120	96.43	3.1166	13.449	0.40	0.16	96.15	12.64	350.97	3.75
H	1180	106.02	8.2555	12.308	2.80	0.06	97.22	21.12	387.48	1.22
I	1220	121.09	10.1796	11.800	8.70	0.05	97.82	47.49	439.32	2.26
J	1260	98.02	9.3757	6.736	8.27	0.05	98.77	72.54	366.46	0.74
K	1650	121.87	10.0555	13.056	9.06	0.05	97.52	100.00	440.60	1.60
Integrated age ± 2s			n=11		33.01	0.06		K2O=0.41%	428.14	1.93

ZT 10-08, Hornblende, 5.71 mg, J=0.0023557±0.07%,

A	900	832.39	0.4686	1049.615	0.44	1.09	62.75	3.48	1447.49	19.65
B	1000	349.76	0.8371	199.788	0.95	0.61	83.14	10.97	941.74	5.74
C	1050	24.92	0.4666	12.328	1.02	1.09	85.53	19.04	88.37	1.35
D	1080	27.81	0.9219	8.390	1.03	0.55	91.36	27.13	104.91	1.27
E	1100	41.99	3.1801	10.695	0.96	0.16	93.10	34.70	159.24	1.63
F	1120	87.64	8.3777	15.621	1.05	0.06	95.53	42.99	326.44	2.12
G	1150	153.16	12.7632	29.708	1.21	0.04	94.96	52.49	535.62	2.37
H	1180	165.62	16.8946	25.314	2.98	0.03	96.33	75.98	581.47	1.51
I	1200	131.13	16.6921	21.473	0.73	0.03	96.22	81.72	474.30	3.48
J	1220	178.66	18.3666	17.958	0.14	0.03	97.88	82.78	629.21	16.87
K	1240	208.07	32.8011	66.546	0.07	0.02	91.96	83.37	684.36	31.50
L	1260	317.96	34.8686	102.139	0.03	0.01	91.61	83.57	960.81	96.42
M	1400	219.81	16.8351	40.189	1.62	0.03	95.23	96.35	730.28	2.55
N	1650	153.28	10.4888	43.900	0.46	0.05	92.10	100.00	521.27	5.23
Integrated age ± 2s			n=14		12.70	0.05		K2O=0.36%	542.06	2.47

ZT 05-08, Hornblende, 11.84 mg, J=0.0022964±0.08%,

A	900	382.43	4.2869	629.589	0.67	0.12	51.45	3.12	674.34	6.14
B	1000	168.64	3.8256	41.263	1.14	0.13	92.96	8.42	555.99	2.66
C	1050	48.46	5.1531	13.486	0.67	0.10	92.66	11.53	177.62	2.24
D	1080	57.51	8.8242	9.252	0.65	0.06	96.52	14.54	217.70	1.86
E	1100	82.21	10.1045	11.582	1.17	0.05	96.86	19.97	304.91	1.47
F	1120	99.74	13.7584	12.054	1.15	0.04	97.57	25.31	367.07	1.65
G	1150	105.80	14.0786	12.051	3.06	0.04	97.74	39.52	387.81	1.18
H	1180	106.21	14.1572	9.037	4.65	0.04	98.59	61.11	392.23	0.92
I	1200	92.66	14.1507	10.155	0.63	0.04	98.03	64.04	344.86	2.78
J	1220	77.77	6.0341	17.992	0.21	0.08	93.81	65.00	280.51	6.54
K	1240	81.75	19.0870	40.680	0.18	0.03	87.49	65.84	277.77	7.66
L	1260	82.20	12.2825	20.873	0.15	0.04	93.78	66.52	296.36	8.52
M	1350	135.85	13.3373	11.050	6.21	0.04	98.41	95.33	486.99	1.01
N	1650	122.37	12.5715	22.378	1.01	0.04	95.45	100.00	432.02	2.25
Integrated age ± 2s			n=14		21.54	0.04		K2O=0.30%	418.70	1.59

ZT 14-08, Biotite, 2.42 mg, J=0.002302±0.09%,

A	650	40.61	0.2039	105.306	0.64	2.50	23.43	0.64	39.09	2.44
B	750	21.06	0.0225	7.975	2.75	22.64	88.82	3.36	76.00	0.47
C	850	34.46	0.0049	3.618	6.89	103.46	96.90	10.17	133.56	0.30
D	920	36.33	0.0017	1.641	15.23	303.33	98.67	25.23	143.01	0.24
E	1000	40.99	0.0011	0.914	12.77	462.06	99.34	37.86	161.60	0.26
F	1075	35.09	0.0037	1.105	12.12	136.28	99.07	49.84	138.84	0.24
G	1110	33.83	0.0047	1.054	11.94	108.00	99.08	61.65	134.05	0.24
H	1180	34.08	0.0050	0.850	18.32	102.50	99.26	79.76	135.26	0.24
I	1210	36.18	0.0080	1.067	10.19	63.60	99.13	89.84	143.09	0.25
J	1250	41.77	0.0257	1.734	6.82	19.85	98.79	96.58	163.69	0.37
K	1300	62.24	0.1330	1.693	2.33	3.84	99.21	98.88	239.78	0.91
L	1680	75.59	0.8602	24.072	1.13	0.59	90.68	100.00	264.46	1.38
Integrated age ± 2s			n=12		101.14	25.80		K2O=6.97%	144.44	0.42

ZT 12-08, Biotite, 3.87 mg, J=0.0023166±0.07%,

A	650	36.75	0.2336	72.254	0.85	2.18	41.96	0.63	63.32	1.70
B	750	26.99	0.2221	9.653	2.41	2.30	89.50	2.43	98.21	0.53
C	850	51.43	0.0503	6.120	8.07	10.14	96.49	8.45	196.29	0.38
D	920	55.83	0.0188	2.458	16.39	27.13	98.70	20.68	216.73	0.36
E	1000	54.41	0.0222	1.888	16.75	23.00	98.98	33.19	212.07	0.39
F	1075	48.66	0.0368	1.717	15.62	13.88	98.97	44.84	190.76	0.35
G	1110	52.90	0.0362	2.043	15.45	14.09	98.87	56.37	206.29	0.32
H	1180	55.45	0.0435	1.755	22.49	11.72	99.07	73.15	216.08	0.40
I	1210	57.56	0.1018	1.795	11.78	5.01	99.09	81.94	223.86	0.42
J	1250	59.58	0.2162	2.439	11.69	2.36	98.83	90.66	230.70	0.37
K	1300	61.46	0.3292	2.275	8.57	1.55	98.95	97.06	237.80	0.46
L	1680	78.85	0.4127	8.337	3.94	1.24	96.92	100.00	294.11	0.77
Integrated age ± 2s			n=12		134.00	5.65		K2O=5.74%	213.15	0.55

ZT 21-08, Biotite, 3.8 mg, J=0.0023105±0.06%,

A	650	69.54	0.0255	212.764	0.36	20.01	9.61	0.30	27.64	4.29
B	750	29.04	0.0112	20.216	1.79	45.42	79.44	1.80	93.64	0.78
C	850	61.12	0.0054	10.381	11.06	94.11	94.98	11.04	227.05	0.45
D	920	66.77	0.0003	4.800	21.21	1799.03	97.88	28.76	253.66	0.44
E	1000	64.48	0.0010	3.896	16.19	501.48	98.22	42.29	246.33	0.40
F	1075	60.93	0.0040	3.757	14.51	126.03	98.18	54.41	233.52	0.42
G	1110	62.46	0.0024	3.563	15.55	216.96	98.32	67.40	239.32	0.43
H	1180	66.45	0.0024	3.606	28.27	216.67	98.40	91.01	253.80	0.45
I	1210	68.07	0.0054	4.224	7.02	93.99	98.17	96.87	258.99	0.56
J	1250	68.53	0.0013	6.279	2.56	384.60	97.31	99.01	258.49	0.81
K	1300	60.73	0.0193	5.857	0.70	26.49	97.16	99.60	230.53	2.14
L	1680	73.68	0.3484	42.979	0.48	1.46	82.80	100.00	237.92	3.17
Integrated age ± 2s			n=12		119.71	123.01		K2O=5.24%	243.24	0.64

ZT 26-08, Biotite, 3.98 mg, J=0.0023157±0.06%,

A	650	33.96	-0.0790	103.019	0.63	-	10.37	0.41	14.65	2.87
B	750	27.76	0.0114	29.485	2.33	44.87	68.61	1.92	77.84	0.77
C	850	39.00	0.0113	7.363	15.80	44.99	94.42	12.18	147.59	0.28
D	920	41.90	0.0032	2.394	22.97	159.08	98.31	27.10	164.32	0.29
E	1000	43.22	0.0032	2.611	18.73	157.99	98.22	39.27	169.12	0.34
F	1075	40.97	0.0055	2.907	19.94	92.22	97.90	52.22	160.21	0.32
G	1110	41.06	0.0046	2.986	18.62	110.91	97.85	64.31	160.47	0.30
H	1180	41.94	0.0071	2.324	27.43	72.01	98.36	82.12	164.55	0.54
I	1210	42.76	0.0134	1.712	13.52	38.06	98.82	90.91	168.39	0.30
J	1250	43.31	0.0286	1.343	9.56	17.87	99.10	97.11	170.90	0.36
K	1300	45.30	0.0856	0.529	3.02	5.96	99.67	99.07	179.36	0.66
L	1680	57.32	0.2195	13.932	1.43	2.32	92.85	100.00	209.67	1.15
Integrated age ± 2s			n=12		153.98	46.03		K2O=6.42%	161.86	0.46

ZT 08-08, Biotite, 3.1 mg, J=0.0023536±0.07%,										
A	650	29.05	0.0701	66.867	0.74	7.28	32.02	0.61	39.07	1.67
B	750	36.20	0.1081	25.087	1.43	4.72	79.55	1.80	118.29	1.18
C	850	58.15	0.0210	8.532	10.13	24.25	95.67	10.21	221.96	0.46
D	920	62.40	0.0087	2.592	17.66	58.95	98.78	24.88	244.37	1.25
E	1000	62.17	0.0097	2.747	15.99	52.40	98.70	38.16	243.33	0.39
F	1075	59.18	0.0200	3.255	12.16	25.54	98.38	48.26	231.64	0.39
G	1110	57.16	0.0191	3.874	11.24	26.76	98.00	57.60	223.41	0.43
H	1180	60.52	0.0175	2.776	20.65	29.13	98.65	74.75	237.16	0.46
I	1210	62.99	0.0485	2.123	11.16	10.52	99.01	84.02	247.07	0.42
J	1250	65.30	0.0850	2.507	11.52	6.00	98.88	93.59	255.21	0.45
K	1300	66.69	0.2082	1.571	6.34	2.45	99.33	98.86	261.39	0.53
L	1680	74.56	0.5143	18.806	1.37	0.99	92.61	100.00	271.71	1.54
Integrated age ± 2s			n=12		120.39	12.06		K2O=6.34%	237.75	0.71
ZT 03-08, Biotite, 3.19 mg, J=0.002288±0.08%,										
A	650	21.14	0.0665	45.447	1.30	7.68	36.53	0.92	31.59	1.36
B	750	29.78	0.0907	33.321	1.45	5.62	66.97	1.95	80.48	1.13
C	850	46.47	0.0159	14.640	12.78	32.02	90.69	10.99	166.03	0.40
D	920	53.46	0.0038	3.797	20.51	133.33	97.90	25.52	204.02	0.44
E	1000	55.89	0.0059	4.562	19.26	86.24	97.59	39.15	212.13	0.44
F	1075	52.31	0.0078	7.968	17.47	65.64	95.50	51.52	195.21	0.43
G	1110	49.69	0.0066	10.408	12.27	76.88	93.81	60.20	182.78	0.34
H	1180	51.66	0.0092	7.306	27.50	55.43	95.82	79.67	193.52	0.31
I	1210	53.52	0.0170	4.517	14.11	29.96	97.51	89.66	203.47	0.33
J	1250	55.82	0.0345	2.912	9.02	14.79	98.47	96.04	213.67	0.42
K	1300	61.20	0.0654	2.215	4.51	7.80	98.94	99.23	234.06	0.60
L	1680	78.81	0.3075	25.031	1.09	1.66	90.65	100.00	273.13	1.59
Integrated age ± 2s			n=12		141.26	31.82		K2O=7.43%	196.08	0.58

Notes:
Isotopic ratios corrected for blank, radioactive decay, and mass discrimination, not corrected for interfering reactions.
Errors quoted for individual analyses include analytical error only, without interfering reaction or J uncertainties.
Integrated age calculated by summing isotopic measurements of all steps.
Integrated age error calculated by quadratically combining errors of isotopic measurements of all steps.
Plateau age is inverse-variance-weighted mean of selected steps.
Plateau age error is inverse-variance-weighted mean error (Taylor, 1982) times root MSWD where MSWD>1.
Plateau error is weighted error of Taylor (1982).
Decay constants and isotopic abundances after Steiger and Jäger (1977).
symbol preceding sample ID denotes analyses excluded from plateau age calculations.
Weight percent K_2O calculated from ^{39}Ar signal, sample weight, and instrument sensitivity.
Ages calculated relative to FC-2 Fish Canyon Tuff sanidine interlaboratory standard at 28.02 Ma
Decay Constant (LambdaK (total)) = 5.543e-10/a
Correction factors:
$(^{39}Ar/^{37}Ar)_{Ca}$ = 0.0007 ± 5e-05
$(^{36}Ar/^{37}Ar)_{Ca}$ = 0.00028 ± 2e-05
$(^{38}Ar/^{39}Ar)_{K}$ = 0.013
$(^{40}Ar/^{39}Ar)_{K}$ = 0.01 ± 0.002

Table 4.6: $^{40}Ar/^{39}Ar$ isotopic data for muscovite, biotite and hornblende from the western Tatra.

4.5. Modeling retrograde diffusion profiles in garnet

In high-grade metamorphic rocks, garnet is often considered the best mineral from which to derive quantitative temperature-time information from retrograde diffusion zoning (e.g. Weyer et al., 1999). Modeling garnet zoning profiles is based on simple thermo-kinetic laws and several assumptions. The first assumption to model retrograde zoning profile is that the garnet crystals do not retain any prograde zoning before undergoing their retrograde path. In other words, the garnets must have stayed long enough at their peak temperature conditions to be fully homogenized. First-order rim to rim major element profiles were of the garnets were obtained to unsure that this assumption was meet and that the only zoning observed was at the rims. The second assumption is that garnet in the migmatites was mainly exchanging cations with biotite and that the volume diffusion in garnet is much slower than in biotite which is modeled as infinitely fast. It is therefore assumed that diffusion within the garnet crystal is the main control of the diffusion rate and that no zoning builds up in the neighboring biotite. The thermodynamic equations are based on an Arrhenius equation with an equilibrium constant that is function of a changing temperature. These equations have been first described in Lasaga (1983) and are also presented in others (e.g. Weyer et al., 1999; Dachs & Proyer, 2002; Robl et al., 2007). We used the Thermal History software developed by Robl et al. (2007; http://wegener.uni-graz.at/publication/publication.html). Our hope in using such an open-source program is to allow for easy comparison and reproducibility of our results. In our calculations we applied a cooling curve linear in 1/T (Dodson, 1986). The starting temperature was estimated from geothermometry (see section 3). All diffusion profiles were obtained using the dataset from Ganguly et al. (1998). This dataset was chosen because it represents the most recent estimate for

the Fe-Mg exchange between garnet and biotite. All other parameters were specific to each garnet-biotite mineral pair and are summarized in table 4.7. Figure 4.8 shows the results of these modeled profiles for 4 garnets from two migmatites (ZT-12-08 & ZT-08-08). Sample ZT-12-08 was also used for monazite U-Pb dating and both samples were used for biotite $^{40}Ar/^{39}Ar$ thermochronology. No modeling was performed for garnets from the lower unit micashist since a remnant of prograde zoning was clearly noticeable from EMP transect. Figure 4.8 also shows electron microprobe transects across the same garnets. A summary of the measured transect is showed in table 4.8.

Electron microprobe analysis was performed using a Cameca SX-100 operated by the Bureau of Geology and Mineral Resources, New Mexico Institute of Mining & Technology, USA. The probe is equipped with high-speed, backscatter electron detectors and 3 wavelength dispersive (WD) spectrometers, each outfitted with multiple analyzing crystals, for precise quantitative analysis of a wide range of elemental abundances. Polished thin sections were prepared and treated with a conductive carbon coating to prevent charging during electron bombardment. During analysis, heating of a tungsten filament held at negative potential produced and accelerated electrons toward the sample. A series of magnetic electron lenses focused and concentrated a 15kV, 10nA electron beam to a minimum resolution of 1 micron. This bombardment produced backscattered electrons (BSE), secondary electrons, X-rays, and cathodoluminescence; the analyses conducted for this study utilized the backscattered electrons and X-rays to acquire both qualitative and quantitative information about sample composition. Backscattered electrons (incident electrons deflected back from the surface with high energy) were used for imaging of samples. The brightness of the image produced is proportional to the amount of deflected electrons, which is a function of the mean atomic number (Z) of the mineral.

This allows visual discrimination of compositionally distinct mineral phases within the separates. Interactive BSE images were used during EMP analysis to assess the purity and homogeneity of mineral phases and to assist the targeting of phases for quantitative analysis of composition. Comparison of the X-rays generated from the sample during electron bombardment and detected by the 3 WD spectrometers with those of known standards allowed precise characterization of the mineral phase from each sample

(a)

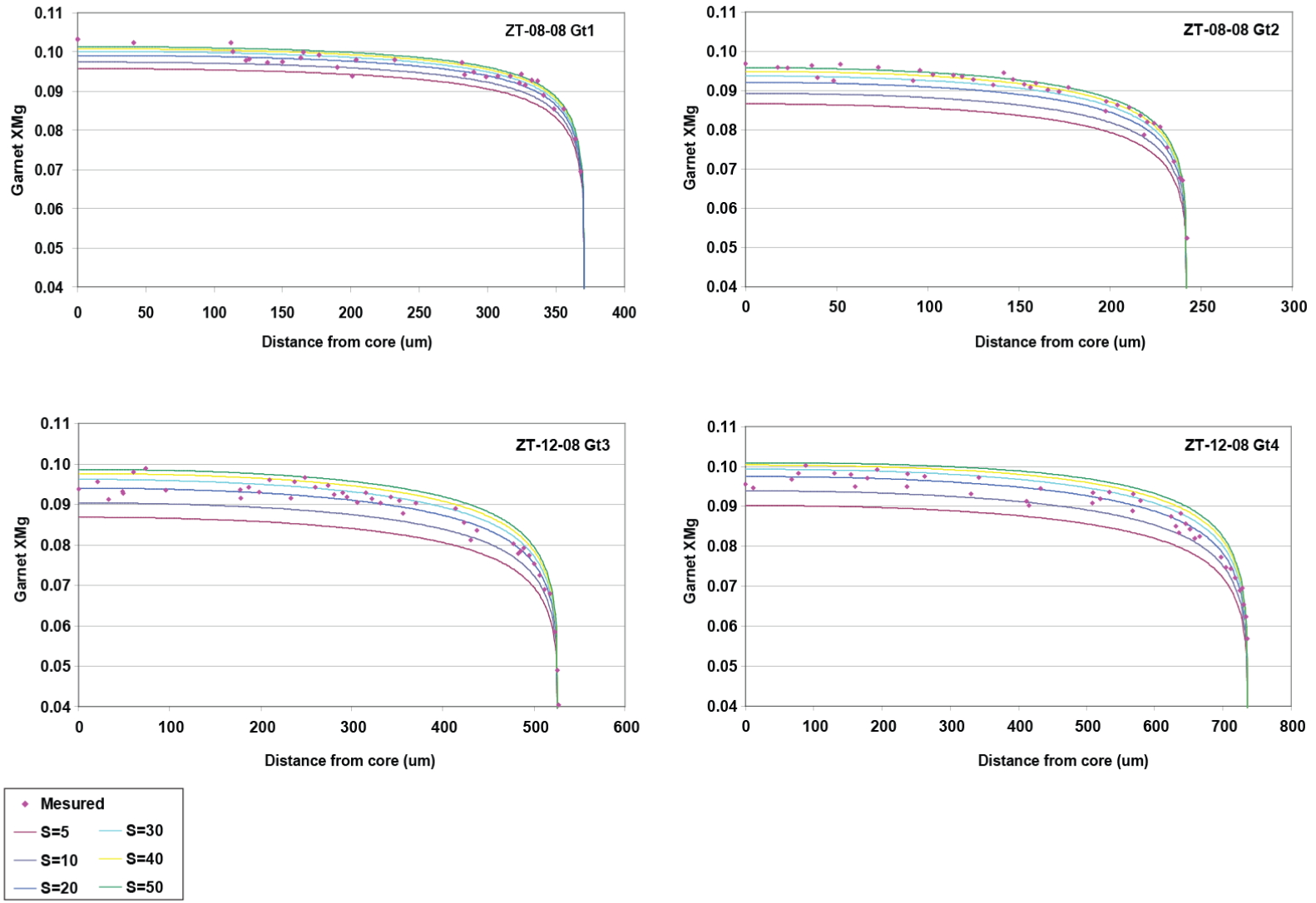
ZT-08-08 Gt1
ZT-08-08 Gt2
ZT-12-08 Gt3
ZT-12-08 Gt4
Garnet XMg
Distance from core (um)
Mesured
S=5
S=10
S=20
S=30
S=40
S=50

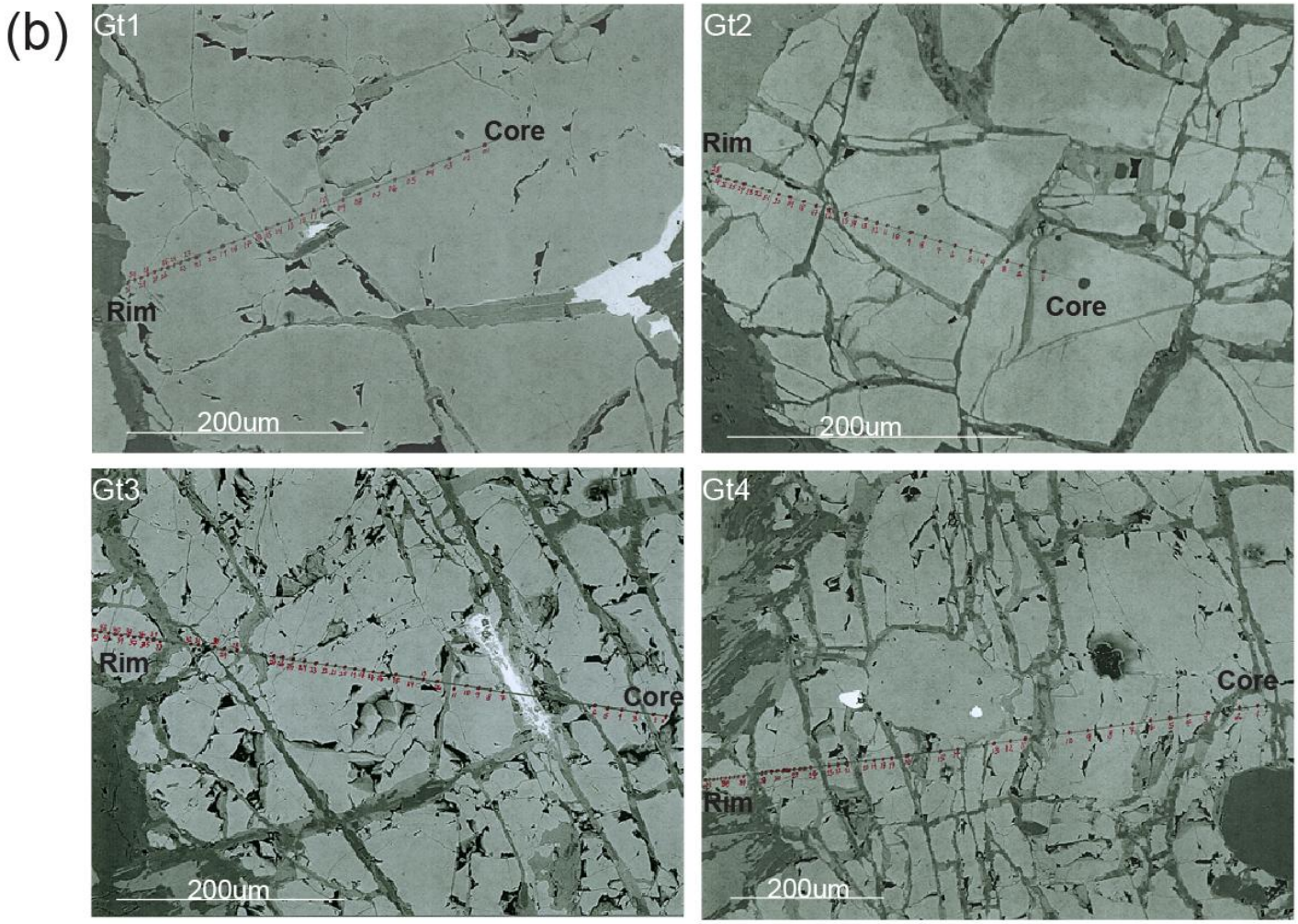

Figure 4.8: (a):Mg diffusion profiles for four garnets from migmatites (from sample ZT-08-08 and ZT-12-08) modeled for different cooling rates (curves) and compared to EMP measured values (dots). Cooling rates range from the lowest curve at 5°/Ma to the highest at 50°/Ma with intermediate curves representing 10°/Ma, 20°/Ma, 30°/Ma and 40°/Ma. (b) SEM images of garnets with the location of the analyzed transects.

Parameter name	Value			
Garnet Label	ZT-08-08_ Grt1	ZT-08-08_ Grt2	ZT-12-08_ Grt3	ZT-12-08_ Grt4
Radius (μm)	371	242.5	527	737
Temperature Step (K)	1	1	1	1
Number of Nodes	301	301	301	301
XMg Biotite	0.256	0.256	0.25	0.25
Section (mm)	0	0	0	0
VBt	0.3	0.6	0.9	0.9
VGt	0.7	0.4	0.1	0.1
Diffusion Constants				
D0Fe (m2/s)	3.50E-09	3.50E-09	3.50E-09	3.50E-09
QFe (J/mol)	274186	274186	274186	274186
D0Mg (m2/s)	4.66E-09	4.66E-09	4.66E-09	4.66E-09
QMg (J/mol)	254220	254220	254220	254220
Reference	Ganguly et al. 1998	Ganguly et al. 1998	Ganguly et al. 1998	Ganguly et al. 1998
Cooling History				
Cooling	(Dodson,1986)	(Dodson,1986)	(Dodson,1986)	(Dodson,1986)
Start Temperature (K)	1123	1123	1123	1123
End Temperature (K)	400	400	400	400
Cooling Rate (K/my)	5, 10, 20, 30, 40, 50	5, 10, 20, 30, 40, 50	5, 10, 20, 30, 40, 50	5, 10, 20, 30, 40, 50
Cooling Rate at K (K)	973	973	973	973

Table 4.7: Parameters used in the software Thermal History (Robl et al., 2007) for garnet diffusion modeling

Spot #	Distance from core (μm)	MgO Wt% Oxide	FeO Wt% Oxide	CaO Wt% Oxide	MnO Wt% Oxide	Mg Wt% element	Fe Wt% element	XMg (ratio)
ZT-08-08-grt1_1	0.00	4.688	31.594	2.544	1.989	2.827	24.558	0.103
ZT-08-08-grt1_2	0.00	4.688	31.594	2.544	1.989	2.827	24.558	0.103
ZT-08-08-grt1_3	123.11	4.513	32.266	2.633	1.965	2.722	25.081	0.098
ZT-08-08-grt1_4	125.33	4.552	32.452	2.655	1.854	2.745	25.225	0.098
ZT-08-08-grt1_5	112.00	4.628	31.502	2.586	2.031	2.791	24.487	0.102
ZT-08-08-grt1_6	41.24	4.628	31.502	2.586	2.031	2.791	24.487	0.102
ZT-08-08-grt1_7	138.67	4.480	32.276	2.586	1.897	2.702	25.088	0.097
ZT-08-08-grt1_8	149.78	4.524	32.492	2.718	1.911	2.728	25.256	0.097
ZT-08-08-grt1_9	113.40	4.596	32.054	2.627	2.068	2.772	24.916	0.100
ZT-08-08-grt1_10	163.11	4.559	32.346	2.598	1.911	2.749	25.143	0.099
ZT-08-08-grt1_11	176.44	4.557	32.076	2.579	1.879	2.748	24.933	0.099
ZT-08-08-grt1_12	164.95	4.576	31.970	2.603	1.928	2.759	24.850	0.100
ZT-08-08-grt1_13	189.78	4.437	32.390	2.652	1.876	2.676	25.177	0.096
ZT-08-08-grt1_14	203.61	4.492	32.103	2.693	2.057	2.709	24.954	0.098
ZT-08-08-grt1_15	200.89	4.339	32.530	2.689	1.834	2.617	25.286	0.094
ZT-08-08-grt1_16	231.96	4.462	31.838	2.700	1.992	2.691	24.748	0.098
ZT-08-08-grt1_17	280.93	4.407	31.747	2.659	2.143	2.658	24.677	0.097
ZT-08-08-grt1_18	324.74	4.249	31.672	2.760	2.169	2.562	24.619	0.094
ZT-08-08-grt1_19	355.67	3.859	32.024	2.728	2.546	2.327	24.892	0.085
ZT-08-08-grt1_20	283.11	4.374	32.646	2.670	1.950	2.638	25.376	0.094
ZT-08-08-grt1_21	289.78	4.374	32.354	2.640	1.903	2.638	25.149	0.095
ZT-08-08-grt1_22	298.67	4.340	32.595	2.815	1.961	2.617	25.336	0.094
ZT-08-08-grt1_23	307.56	4.305	32.270	2.685	1.975	2.596	25.084	0.094
ZT-08-08-grt1_24	316.44	4.330	32.474	2.523	1.998	2.611	25.242	0.094
ZT-08-08-grt1_25	323.11	4.243	32.480	2.570	1.956	2.559	25.247	0.092
ZT-08-08-grt1_26	327.56	4.212	32.430	2.561	2.014	2.540	25.208	0.092
ZT-08-08-grt1_27	332.00	4.278	32.441	2.475	2.017	2.580	25.217	0.093
ZT-08-08-grt1_28	336.44	4.244	32.275	2.491	2.126	2.559	25.088	0.093
ZT-08-08-grt1_29	340.89	4.092	32.491	2.527	2.078	2.468	25.255	0.089
ZT-08-08-grt1_30	348.33	3.962	32.887	2.549	2.159	2.389	25.563	0.085
ZT-08-08-grt1_31	364.00	3.548	32.604	2.632	2.471	2.140	25.343	0.078
ZT-08-08-grt1_32	368.00	3.165	32.927	2.589	2.890	1.909	25.594	0.069
ZT-08-08-grt2_1	0.00	4.404	31.840	2.819	1.972	2.656	24.749	0.097
ZT-08-08-grt2_2	17.71	4.348	31.790	2.933	2.046	2.622	24.711	0.096
ZT-08-08-grt2_3	23.00	4.287	31.406	2.792	1.791	2.585	24.412	0.096
ZT-08-08-grt2_4	36.46	4.351	31.665	3.089	2.008	2.624	24.613	0.096
ZT-08-08-grt2_5	39.36	4.157	31.372	2.913	1.769	2.507	24.386	0.093
ZT-08-08-grt2_6	48.45	4.217	32.094	3.079	1.855	2.543	24.947	0.093
ZT-08-08-grt2_7	52.08	4.344	31.505	2.931	2.072	2.620	24.489	0.097
ZT-08-08-grt2_8	72.92	4.318	31.593	3.019	2.017	2.604	24.557	0.096
ZT-08-08-grt2_9	92.09	4.236	32.247	2.871	1.937	2.554	25.066	0.092
ZT-08-08-grt2_10	95.83	4.291	31.650	3.041	2.009	2.588	24.602	0.095
ZT-08-08-grt2_11	103.00	4.298	32.144	2.897	1.930	2.592	24.986	0.094
ZT-08-08-grt2_12	113.91	4.304	32.205	2.927	1.901	2.595	25.033	0.094
ZT-08-08-grt2_13	118.75	4.201	31.541	3.100	1.979	2.533	24.517	0.094
ZT-08-08-grt2_14	124.82	4.205	31.871	2.998	1.853	2.536	24.774	0.093
ZT-08-08-grt2_15	135.73	4.143	31.949	3.049	1.955	2.498	24.834	0.091
ZT-08-08-grt2_16	141.67	4.240	31.535	2.919	2.024	2.557	24.512	0.094
ZT-08-08-grt2_17	146.64	4.213	31.950	3.117	1.946	2.541	24.835	0.093
ZT-08-08-grt2_18	153.00	4.620	35.566	3.333	2.102	2.786	27.646	0.092
ZT-08-08-grt2_19	156.25	4.078	31.658	2.995	2.065	2.459	24.608	0.091
ZT-08-08-grt2_20	159.36	4.173	32.023	3.012	1.924	2.516	24.892	0.092
ZT-08-08-grt2_21	165.73	4.115	32.197	3.065	1.933	2.481	25.027	0.090
ZT-08-08-grt2_22	172.09	4.054	31.905	3.135	1.923	2.445	24.800	0.090
ZT-08-08-grt2_23	177.08	4.105	31.917	2.950	2.214	2.475	24.809	0.091
ZT-08-08-grt2_24	197.55	3.860	32.316	3.153	2.146	2.328	25.119	0.085
ZT-08-08-grt2_25	197.92	3.914	31.762	3.181	2.248	2.360	24.689	0.087
ZT-08-08-grt2_26	203.91	3.915	32.149	3.262	2.074	2.361	24.990	0.086
ZT-08-08-grt2_27	210.27	3.882	32.151	3.126	2.072	2.341	24.991	0.086
ZT-08-08-grt2_28	216.64	3.814	32.383	3.139	2.271	2.300	25.171	0.084
ZT-08-08-grt2_29	218.75	3.521	31.976	3.061	2.649	2.123	24.855	0.079
ZT-08-08-grt2_30	220.27	3.747	32.581	3.075	2.264	2.260	25.325	0.082
ZT-08-08-grt2_31	223.91	3.716	32.421	3.043	2.292	2.241	25.201	0.082
ZT-08-08-grt2_32	227.55	3.657	32.324	2.990	2.487	2.205	25.126	0.081
ZT-08-08-grt2_33	231.18	3.375	32.049	3.071	2.596	2.035	24.912	0.076
ZT-08-08-grt2_34	234.82	3.229	32.334	2.946	2.749	1.947	25.133	0.072
ZT-08-08-grt2_35	238.45	3.006	32.130	2.906	3.144	1.813	24.975	0.068
ZT-08-08-grt2_36	239.58	2.958	31.906	3.087	3.301	1.784	24.801	0.067
ZT-08-08-grt2_37	242.09	2.313	32.411	2.990	4.051	1.395	25.193	0.052

ZT-12-08-grt3_1	0.00	4.766	35.715	1.213	2.168	2.874	27.761	0.094
ZT-12-08-grt3_2	21.00	4.646	34.126	1.131	1.717	2.802	26.526	0.096
ZT-12-08-grt3_3	32.49	4.402	34.035	1.131	1.841	2.655	26.456	0.091
ZT-12-08-grt3_4	47.95	4.740	35.795	1.077	2.171	2.858	27.824	0.093
ZT-12-08-grt3_5	48.59	4.528	34.381	1.174	1.828	2.731	26.725	0.093
ZT-12-08-grt3_6	60.08	4.715	33.658	1.079	1.802	2.843	26.163	0.098
ZT-12-08-grt3_7	73.87	4.764	33.660	1.112	1.760	2.873	26.164	0.099
ZT-12-08-grt3_8	95.89	4.748	35.720	1.097	2.112	2.863	27.765	0.093
ZT-12-08-grt3_9	177.32	4.514	33.893	1.255	1.804	2.722	26.345	0.094
ZT-12-08-grt3_10	178.08	4.635	35.679	1.192	2.166	2.795	27.733	0.092
ZT-12-08-grt3_11	186.52	4.527	33.773	1.193	1.819	2.730	26.252	0.094
ZT-12-08-grt3_12	198.01	4.481	33.877	1.172	1.827	2.702	26.333	0.093
ZT-12-08-grt3_13	209.51	4.618	33.736	1.185	1.760	2.785	26.223	0.096
ZT-12-08-grt3_14	232.88	4.663	35.923	1.177	2.257	2.812	27.923	0.091
ZT-12-08-grt3_15	237.09	4.547	33.397	1.180	1.805	2.742	25.960	0.096
ZT-12-08-grt3_16	248.59	4.687	33.968	1.200	1.750	2.826	26.404	0.097
ZT-12-08-grt3_17	260.08	4.568	34.077	1.159	1.793	2.755	26.488	0.094
ZT-12-08-grt3_18	273.87	4.556	33.827	1.148	1.859	2.747	26.294	0.095
ZT-12-08-grt3_19	280.77	4.506	34.330	1.124	1.883	2.717	26.685	0.092
ZT-12-08-grt3_20	289.97	4.488	34.027	1.130	1.905	2.706	26.449	0.093
ZT-12-08-grt3_21	294.52	4.665	35.808	1.191	2.286	2.813	27.834	0.092
ZT-12-08-grt3_22	306.06	4.368	34.038	1.161	1.917	2.634	26.458	0.091
ZT-12-08-grt3_23	315.25	4.493	34.045	1.159	1.945	2.709	26.463	0.093
ZT-12-08-grt3_24	322.15	4.450	34.327	1.207	2.024	2.684	26.683	0.091
ZT-12-08-grt3_25	331.34	4.355	34.031	1.174	1.906	2.626	26.452	0.090
ZT-12-08-grt3_26	342.84	4.402	33.757	1.216	1.864	2.655	26.240	0.092
ZT-12-08-grt3_27	352.03	4.399	34.128	1.218	1.935	2.653	26.528	0.091
ZT-12-08-grt3_28	356.16	4.409	35.522	1.247	2.460	2.659	27.611	0.088
ZT-12-08-grt3_29	370.43	4.363	34.062	1.152	1.944	2.631	26.477	0.090
ZT-12-08-grt3_30	414.10	4.269	33.907	1.349	2.195	2.574	26.356	0.089
ZT-12-08-grt3_31	423.30	3.921	32.522	1.331	1.979	2.365	25.280	0.086
ZT-12-08-grt3_32	430.66	4.049	35.557	1.290	2.613	2.442	27.639	0.081
ZT-12-08-grt3_33	437.09	3.962	33.738	1.348	2.223	2.389	26.225	0.083
ZT-12-08-grt3_34	477.32	3.849	34.223	1.346	2.512	2.321	26.602	0.080
ZT-12-08-grt3_35	483.07	3.737	34.324	1.402	2.606	2.254	26.680	0.078
ZT-12-08-grt3_36	485.45	3.944	35.928	1.340	3.103	2.378	27.927	0.078
ZT-12-08-grt3_37	488.82	3.780	34.091	1.345	2.652	2.279	26.499	0.079
ZT-12-08-grt3_38	494.56	3.668	33.935	1.355	2.615	2.212	26.378	0.077
ZT-12-08-grt3_39	500.31	3.562	33.967	1.330	2.903	2.148	26.403	0.075
ZT-12-08-grt3_40	506.06	3.436	34.095	1.378	3.018	2.072	26.502	0.073
ZT-12-08-grt3_41	511.80	3.293	34.481	1.341	3.176	1.986	26.802	0.069
ZT-12-08-grt3_42	517.55	3.167	33.743	1.382	3.308	1.910	26.229	0.068
ZT-12-08-grt3_43	523.30	2.723	34.041	1.353	3.837	1.642	26.460	0.058
ZT-12-08-grt3_44	525.40	2.366	35.581	1.348	5.277	1.427	27.657	0.049
ZT-12-08-grt3_45	527.00	1.791	32.928	1.449	5.793	1.080	25.595	0.040
ZT-12-08-grt4_1	0.00	4.829	35.488	1.060	2.083	2.912	27.585	0.095
ZT-12-08-grt4_2	12.00	4.509	33.439	1.002	2.350	2.719	25.992	0.095
ZT-12-08-grt4_3	67.80	4.922	35.657	1.015	2.028	2.968	27.716	0.097
ZT-12-08-grt4_4	78.09	4.785	34.057	1.034	1.666	2.886	26.473	0.098
ZT-12-08-grt4_5	88.52	4.901	34.097	1.033	1.617	2.955	26.504	0.100
ZT-12-08-grt4_6	130.26	4.800	34.168	1.076	1.574	2.895	26.559	0.098
ZT-12-08-grt4_7	154.61	4.781	34.121	1.061	1.721	2.883	26.522	0.098
ZT-12-08-grt4_8	161.02	4.816	35.648	1.055	1.988	2.904	27.709	0.095
ZT-12-08-grt4_9	178.96	4.754	34.279	1.066	1.675	2.867	26.645	0.097
ZT-12-08-grt4_10	192.87	4.812	33.911	1.070	1.750	2.902	26.359	0.099
ZT-12-08-grt4_11	237.29	4.799	35.484	1.141	2.010	2.894	27.582	0.095
ZT-12-08-grt4_12	238.09	4.740	33.812	1.127	1.668	2.858	26.282	0.098
ZT-12-08-grt4_13	262.43	4.740	34.001	1.203	1.699	2.858	26.429	0.098
ZT-12-08-grt4_14	330.51	4.650	35.127	1.306	2.164	2.804	27.304	0.093
ZT-12-08-grt4_15	342.43	4.609	33.176	1.373	1.734	2.779	25.788	0.097
ZT-12-08-grt4_16	412.00	4.418	34.147	1.300	1.892	2.664	26.543	0.091
ZT-12-08-grt4_17	415.25	4.513	35.289	1.372	2.209	2.722	27.430	0.090
ZT-12-08-grt4_18	432.87	4.492	33.393	1.374	1.761	2.709	25.957	0.094
ZT-12-08-grt4_19	508.47	4.543	35.302	1.283	2.311	2.740	27.440	0.091
ZT-12-08-grt4_20	509.39	4.489	33.798	1.288	1.983	2.707	26.271	0.093
ZT-12-08-grt4_21	519.83	4.391	33.682	1.339	1.849	2.648	26.181	0.092
ZT-12-08-grt4_22	533.74	4.482	33.687	1.299	1.939	2.703	26.185	0.094
ZT-12-08-grt4_23	567.80	4.474	35.580	1.246	2.359	2.698	27.657	0.089
ZT-12-08-grt4_24	568.52	4.486	33.890	1.280	1.990	2.705	26.343	0.093
ZT-12-08-grt4_25	578.96	4.383	33.815	1.270	1.915	2.643	26.285	0.091
ZT-12-08-grt4_26	624.17	4.212	34.111	1.199	2.089	2.540	26.515	0.087
ZT-12-08-grt4_27	631.13	4.090	34.145	1.172	2.097	2.466	26.541	0.085
ZT-12-08-grt4_28	635.59	4.200	35.790	1.186	2.493	2.533	27.820	0.083

Table 4.8: Summary of electron microprobe analysis of core to rim major cation zonation profile in garnets from migmatite (ZT-12-08 and ZT-08-08)

If the assumptions stated above were entirely correct the measured and calculated zoning profiles should mimic each other perfectly, however, the measured profiles show some scatter. As a first order approximation the curvature of the natural Mg# profile is in very good agreement with modeled diffusion profiles. Between 32 and 45 electron microprobe analyses were made on each garnet with a spatial resolution between each analyses increasing toward the margin. Apparent "gaps" in the analyses of some garnets are due to excluded chlorite-filled cracks within some garnets. The apparent scatter in the natural Mg# profile is probably a consequence Fe-Mg exchange between the garnet and inclusions such as biotite and chlorite. The effect of such diffusion within the garnet are however local and do not affect the first-order shape of the profile. For all garnets the measured retrograde compositional profile of the Mg# at the rim is bracketed by modeled compositional profiles with cooling rates from 10 to 50 °/Ma. Garnet 1 and 2 show the best agreement with cooling rates in the order of 30 to 40 °/Ma while garnet 3 and 4 best fit with cooling rates around 20 to 30 °/Ma. An average of these analyses hence indicates a cooling rate of ~30 °/Ma for the migmatites of the upper tectonic unit.

5. DISCUSSION

5.1. Interpretation of isotopic results & P-T-t evolution

This study was undertaken in order to constrain the timing and conditions of exhumation of lower and mid-crustal rocks that compose the Variscan metamorphic core of the Western Tatra Mountains. The Western Tatras were chosen because Alpine uplift has presented a unique opportunity to examine a relatively complete section of Variscan crust, arguably part of the Bohemian Massif, within which eclogitic boudins are preserved. To unravel the thermal evolution of the Western Tatra several isotopic dating system were used that resulted in a progression of ages with a strong modal population at ca. 340 Ma. A summary of all obtained radiogenic ages is presented as a probability diagram in figure 5.1. The oldest age population at ca. 380 Ma was obtained by U-Pb monazite geochronology from the upper unit migmatites close to the eclogite lenses. The interpretation of this age is problematic since the only other published ages from the Western Tatra which fall within error is a 369 ± 19 Ma age from TIMS analysis of zircons from a granite body (Poller et al., 2000). This may suggest that the ca. 380 Ma monazite age is derived from the protolith and is not related to a metamorphic event. Such an interpretation is however inconsistent with the nature of the monazites analyzed, which are mostly clear, subhedral-shaped and often aligned along the foliation. Middle Devonian ages from detrital zircons are however common in the flysh sequence of the Barrandian (Prague) Basin within the Moldanubian zone (Strnad & Mihaljevic, 2005). Moreover, metamorphism and exhumation in the Gory Sowie Block from the Sudete Mountains of eastern Bohemia has been constrained to ca. 380 Ma (Gordon et al., 2005; Schneider et al., 2006) and instead argues in favor of a possible thermal event around this period at least in eastern Bohemia.

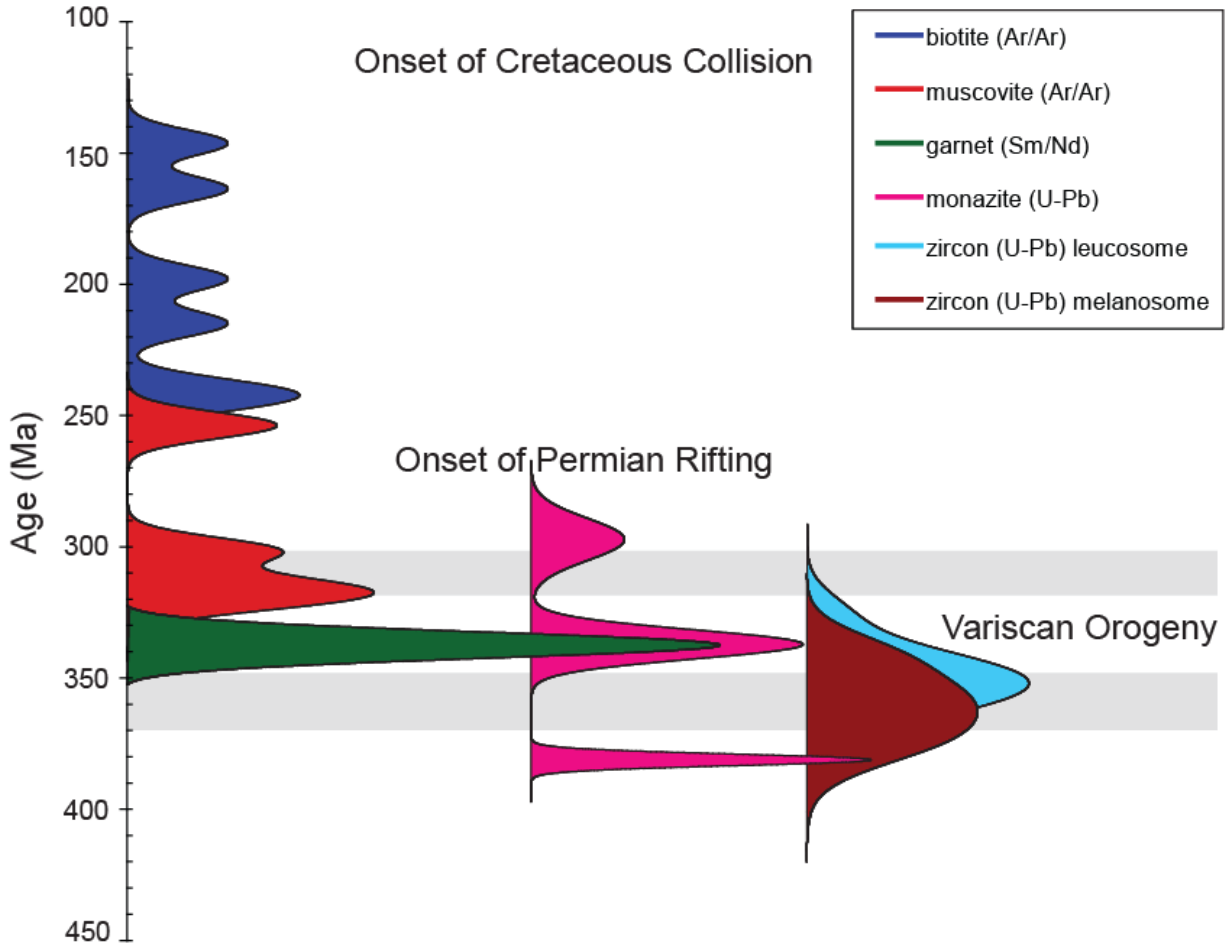

Figure 5.1: Probability curves of all radiogenic ages obtained in this study. Shaded grey bands represent time of known igneous intrusive activity in the area. Biotite, muscovite and garnet ages are reported to the far left. Further right are the monazite ages and to the far right are the zircon ages.

Our U-Pb SIMS dating of two distinct zircon populations from a migmatite revealed an equal amount of age populations. The oldest zircon U-Pb age of 358 ± 17 Ma was obtained from the melanosome portion of an upper unit migmatites and is slightly younger than our oldest monazite ages. There are two possible interpretations for this age, as it could represent a crystallization age since it is comparable to U-Pb ages around ca. 360 Ma obtained by Poller et al. (2000) for orthogneisses and granites in the same area and by Burda (2007) for monazite and zircon from migmatites on the Polish side of the western Tatra. This 358 ± 17 Ma age is associated with a large error because of a large variability in the single zircon ages and should, therefore, not be interpreted as representing a single event. Following this first interpretation, this age can best be described as an average of the crystallization ages of the zircons from the sedimentary protolith of the migmatite. Alternatively this 358 ± 17 Ma age could represent an early partial melting event as hypothesized by Burda & Gaweda (2009) who obtained similar zircon and monazite ages from leucosomal migmatites and leucogranite on the Polish side of the Western Tatra.

The second, younger zircon population U-Pb age of 347 ± 8 Ma from the migmatititic leucosomes is indistinguishable from our monazite U-Pb age of 340 ± 11 Ma which was obtained from the migmatites away from the eclogite and our garnet Sm-Nd age of 337 ± 10 Ma from the eclogite, which is enveloped by the migmatite. As noted above, these migmatites contain older monazite of ca. 380 Ma age. Nevertheless Three methods yield evidence of a significant thermal event at ca. 340 Ma. The Sm-Nd age of eclogite garnet likely represents cooling below 700 ± 50 °C (Tirone et al., 2005). Similar ages have been found in other parts of the Tatric unit (e.g. Finger et al., 2003), in the eastern and southeastern Bohemian Massif (e.g.

Stipska et al., 2004; Gordon et al., 2005; Schulmann et al., 2005) and Hohe Tauern window (Eichhorn et al., 2000). We interpret these ages as representing a widespread anatectic event during the Variscan orogeny, likely driven by isothermal decompression of the lower-middle crust, as suggested by the kelyphitic textures observed in the eclogite.

Although our $^{40}Ar/^{39}Ar$ are disturbed, total gas muscovite and biotite cooling ages become younger toward the northwest, which is structurally downward. In a general sense, this is consistent with the inverted metamorphic pattern previously described. The muscovite $^{40}Ar/^{39}Ar$ total gas release ages cluster between 250 to 310 Ma due to their mixed nature but show maximum ages of 280 to 335 Ma. The partial resetting of these ages might be linked to the widespread granitic intrusions. A (weak?) thermal event around ca. 300 Ma is also consistent with our younger U-Pb monazite population dated at 300 ± 16 Ma. Granite magmatism is abundant in the neighboring High Tatra (Poller & Todt, 2001) which stand structurally immediately above, suggesting an intimate connection between igneous activity and the thermal history of the western Tatra. The biotite $^{40}Ar/^{39}Ar$ ages scatter between 130 and 270 Ma also due to their mixed nature and show maximum ages of 200 to 260 Ma. These ages are considerably younger than those reported by Janák (1994), who obtained single grained in-situ laser probe Ar ages from biotite in migmatites from the nearby High Tatras, 25km to the east. Reported single spot cooling ages spread from 288 to 340 Ma and the oldest ages from biotite inclusions in garnet and the core of large biotite grains, while younger ages are more typical of smaller grains. The spread of ages found in the laser probe analyses does not fully explain the variability obtained from our furnace data, and indicates a complex lower-temperature thermal history and in particular different thermal histories between the Western and High Tatra. Along the eastern margin of the Bohemia, Variscan $^{40}Ar/^{39}Ar$ ages of muscovite and biotite are 340-320 Ma (e.g.

Dallmeyer et al., 1992; Fritz et al., 1996; Schneider et al., 2006; Marnheine et al., 2002); these data are more consistent with our muscovite cooling age population. From our data, it is unclear if the biotite Ar systematics retained any memory of its Variscan history. This resetting could have resulted from both the Permian rifting event and Late Jurassic sediment accumulation coupled with Cretaceous nappe stacking, which could have achieved 4 km of burial (Kohut & Sherlock, 2003).

Coupling our thermochronometric ages with the cooling rates calculated by diffusion modeling in garnet gives an estimate of the thermal evolution of the units (Fig. 5.2). From our calculations it appears that the 30 °/Ma cooling rate is plausible with regard to the thermochronology but the $^{40}Ar/^{39}Ar$ would need better precision in order to firmly establish that the calculated cooling rate is suitable. This estimated cooling rate is much lower than those calculated in modern orogens where it can reach 100 °C/Ma (e.g. Zeck et al., 1992; Foster et al., 2009) but comparable to other estimates from the Variscan belt such as the Black Forest Massif (e.g. Weyer et al., 1999) and Brittany Massif (e.g. Brown & Dallmayer, 1996). Substantially higher cooling rates of (100 to 150 °C/Ma) have been calculated for eclogites in the Bohemian Massif (Medaris et al., 2006). However we believe that these published cooling rates from Medaris et al. (2006) characterize the first stage of exhumation of the eclogite from lower to middle crustal conditions while our calculated rates reflect exhumation from the middle to upper crust. This is consistent with the two-stage exhumation model proposed for many high-grade metamorphic terranes (e.g. Rivers et al., 2002; Walsh & Hacker, 2004; Stipska et al., 2004) where lower crustal material is first exhumed to the middle crust where it re-equilibrates and undergoes supra-Barrovian metamorphism before being exhumed to the upper crust during a second stage.

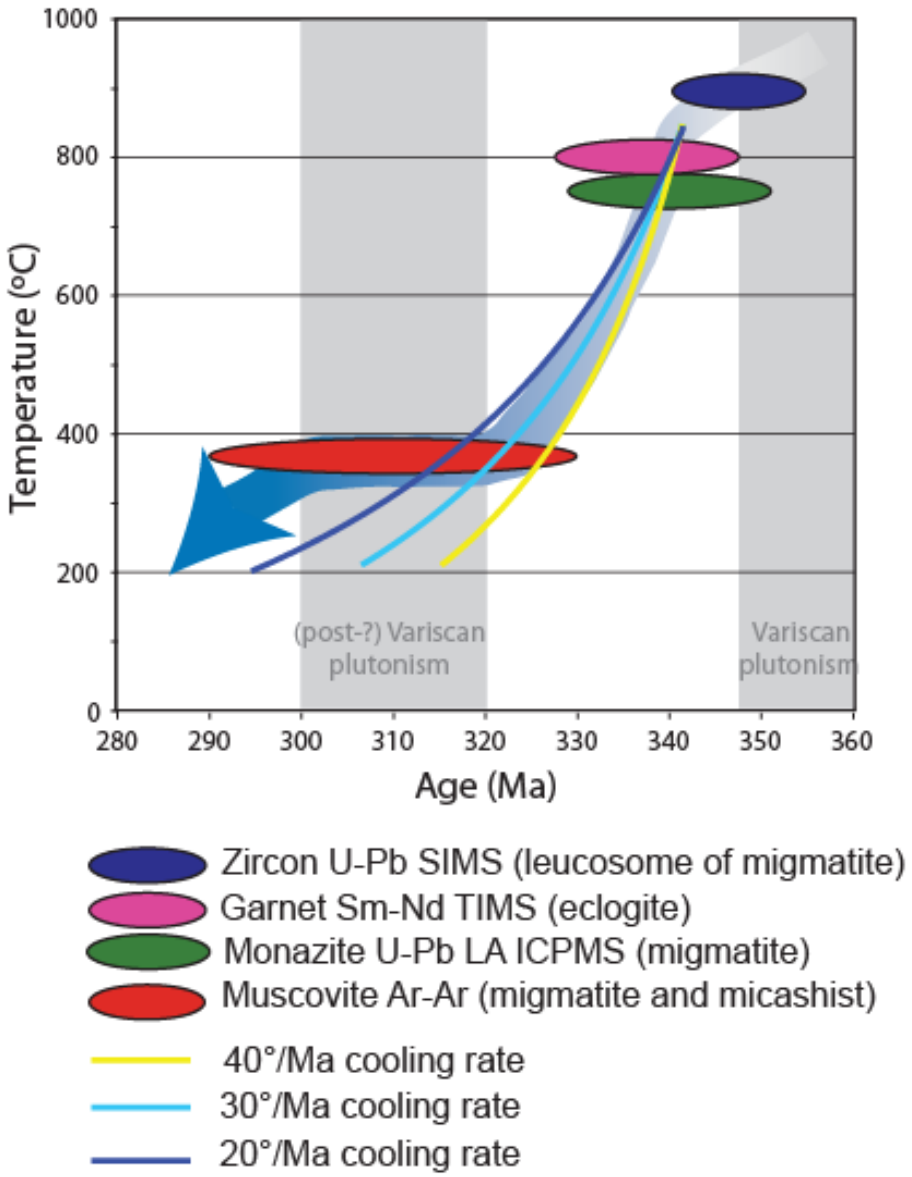

Figure 5.2: Temperature-time evolution of the Western Tatra mountain metamorphic core based on results from this study. Note that the monazite 340 Ma age has been associated with a temperature of 800°C but the ellipse could in fact stretch from 800 to 400°C (Cocherie & Albarède 2001; Suzuki et al., 1994; Smith & Giletti, 1997). Shaded grey bands represent time of known igneous intrusive activity in the area. Cooling rates are based on garnet profile modeling from migmatites (ZT-08-08 and ZT-12-08).

It has been suggested by Dunlap (2000) that the disparity in cooling rates between modern and ancient orogens is a result of partial resetting of thermochronometers by long residence in a thermal window below the closure temperature of radiogenic systems. The calculated cooling rate in this study however is mainly based on diffusion modeling in garnet and therefore should not be affected by such process. The rate of 30 °/Ma therefore appear as moderate cooling, and it is to be noted that this cooling rate is non-linear and proportional to 1/T: the cooling is therefore more rapid close to the peak temperature and progressively slows down as the temperature decreases.

A comparison of the P-T path estimated for the three lithologies that define the Western Tatra reveals dissimilar pressure-temperature evolutions (Fig. 5.3). The middle amphibolite facies lower unit composed of micaschist is inferred to have experienced peak metamorphic conditions at 7 kbar and 650 °C and subsequent cooling and exhumation. The upper unit migmatites experienced metamorphic conditions at 11 kbar and 825 °C while the eclogite, also from the upper unit, experienced pressure conditions of 1.8 GPa followed by isothermal decompression to 1.2 GPa and moderate rates of exhumation. Such a disparity in metamorphic histories for rock units that are now in proximity is puzzling especially since eclogite-bearing amphibolites are found enclosed in migmatites. This observation suggests that eclogite experienced different prograde metamorphic conditions than the migmatites. The two would then have likely been "mixed" during the exhumation process, most likely under mid-crustal conditions. From the thermochronology it appears that both rock types were at these conditions at ca. 340 Ma, at a time when anatexis could have resulted from biotite dehydration-melting reactions (Janák et al., 1999). An alternative hypothesis could be that both eclogites and

migmatites shared the same P-T path but that the migmatites were completely recrystallised due to partial melting at mid-crustal conditions whereas mafic eclogites remained less affected by low-pressure overprint due to their refractive nature. This has been suggested from many (U)HP metamorphic terranes where gneisses contain only minor (U)HP relics in contrast to eclogites (e.g. Western Gneiss Region, Norwegian Caledonides (Dobrzhinetskaya et al., 1995), Saxonian Erzgebirge, Germany (Nasdala & Massonne, 2000), Kokchetav Massif, Kazakhstan (Sobolev & Shatsky, 1990), Dabie Shan-Sulu terrane, China (Liu et al., 2002), and Pohorje, Slovenia (Janák et al. 2009). The P-T evolution of the micashist composing the lower unit is consistent with the scenario of the upper unit being thrust over the lower unit during Variscan collision. Overthrusting would have contributed to the burial and heating of the lower unit coeval with exhumation of the upper unit.

The data obtained support and improve the resolution of previous P-T-t estimates (Janák, 1994, Janák et al., 1996, 1999) from the Western Tatra. In particular, the timing of the mid-crustal to upper-crustal residence of the rock units has been improved by this contribution. The timing of initial high-pressure metamorphism and eclogite formation is however still unconstrained. This high-pressure event had been hypothesized to occur during Caledonian to Eo-Variscan (450 to 400 Ma) events (Burchart, 1968). It now appears more credible that this event happened ca. 360 to 365 Ma (Burda, 2007; Burda & Gaweda, 2009; this study). Our own geochronologic data do not support any metamorphic event before ca. 385 Ma.

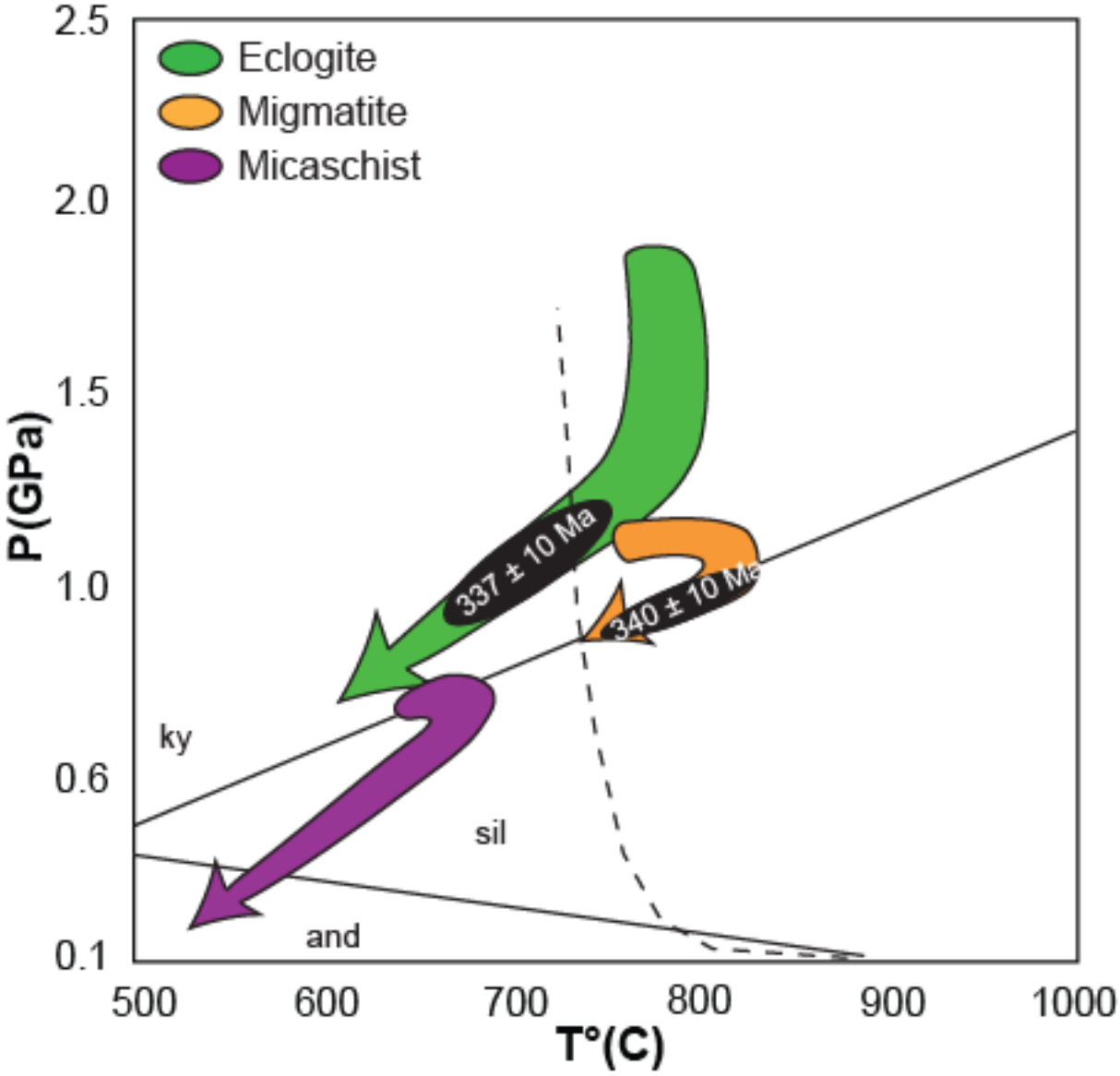

Figure 5.3: P-T-t diagram showing the P-T evolutions calculated from isochemical phase modeling and geothermobarometry with estimated time. Dashed curved represent the dehydration curve of biotite. Straight solid lines represents the aluminosilicate univariant lines after Spear (1993)

The post-Variscan history is only roughly constrained with a Permian rifting event around 280 to 260 Ma (Finger et al., 2003) and followed by Alpine deformation in the Cretaceous. Although recognized in other parts of the Alpine-Carpathian belt, the Permian rifting event seems to have had little to no influence on the rest of the Variscan massifs. Based on the age distribution obtained from $^{40}Ar/^{39}Ar$ dating of biotite presented in figure 5.1 it appears that both the Permian rifting and Cretaceous collision events have had a high enough thermal influence in the Western Tatra to partially reset the Ar systematics in biotite.

5.2. Tectonic implications

A plausible scenario that would explain the contrasting P-T path may be compatible with a tectonic evolution following a heterogeneous mid-crustal extrusion system as numerically modeled by Beaumont et al. (2006) and as recently proposed for part of the nearby Bohemian Massif (Stipska et al., 2008). There are several reasons to consider the high-grade metamorphic rocks from the Tatra to be genetically tied to the Moldanubian crust along southeastern Bohemia. Firstly, the presence of similar lithologies, such as heterogeneously intercalated amphibolite facies migmatites, orthogneisses, micashists and amphibolites with preserved Variscan-aged eclogites and HT granulites (e.g. Stipska et al., 2004). Protolith ages of these sequences cluster around ca. 500 Ma on both sides of the Bohemia-Brunia suture, documenting an extensive Late Cambrian-EarlyOrdovician magmatic event (Kröner et al., 2001; Kohút et al., 2008). Geochemical signatures of the most abundant amphibolite suite in the Tatra and in Moldanubia show indistinguishable enriched MORB signatures (Gaweda et al., 2000; Floyd et al., 2000). Reconstructions of P-T paths from eastern Bohemia and the Tatra illustrate contrasting metamorphic histories between granulite and eclogite facies rocks and host migmatite (Stipska et

al., 2008; this work). Moreover, eclogites show re-equilibration with the migmatites at mid-crustal levels. The temperature-time evolution of the eastern margin of the Bohemian Massif is also quite similar to the Tatras. Sm-Nd garnet cooling ages cluster around 340 Ma (e.g. Beard et al., 1992; Medaris et al., 1998) and the metamorphic peak is interpreted to be around 350-340 Ma (Friedl et al., 2003; Schulmann et al., 2005). The only first-order difference is that of the regional structure. In the middle crustal rocks of the Moldanubian zone, the overall planar and linear fabric is mostly subhorizontal with occasional steep planar fabrics preserving high-pressure assemblages (Pressler et al., 2007; Schulmann et al., 2008). In marked contrast, after removal of Alpine tectonic rotation (Jurewicz, 2005) the pre-Alpine fabric of the Tatra is estimated to be at a moderately steep angle (65°-70°).

All these similarities suggest that the middle and lower crustal rocks exposed in the Tatra Mountains are an eastern extension of the Moldanubian crust synchronously exhumed under similar conditions. One model of lower crustal extrusion for Moldanubia has been proposed by Schulmann et al. (2008). In this model the Bohemia microcontinent is thought to have collided with the microcontinent Brunia, the latter of which has been modeled as a rigid indentor over which the ductile Moldanubian crust would have flowed and exhumed the Variscan lower crust. In this model the middle crust acts according to the heterogeneous channel flow model from numerical modeling of Beaumont et al. (2006). Such a model works well for the western Tatra and explains how rocks from different depths could have mingled in their retrograde path under mid-crustal conditions coeval with anatexis (Fig. 5.4).

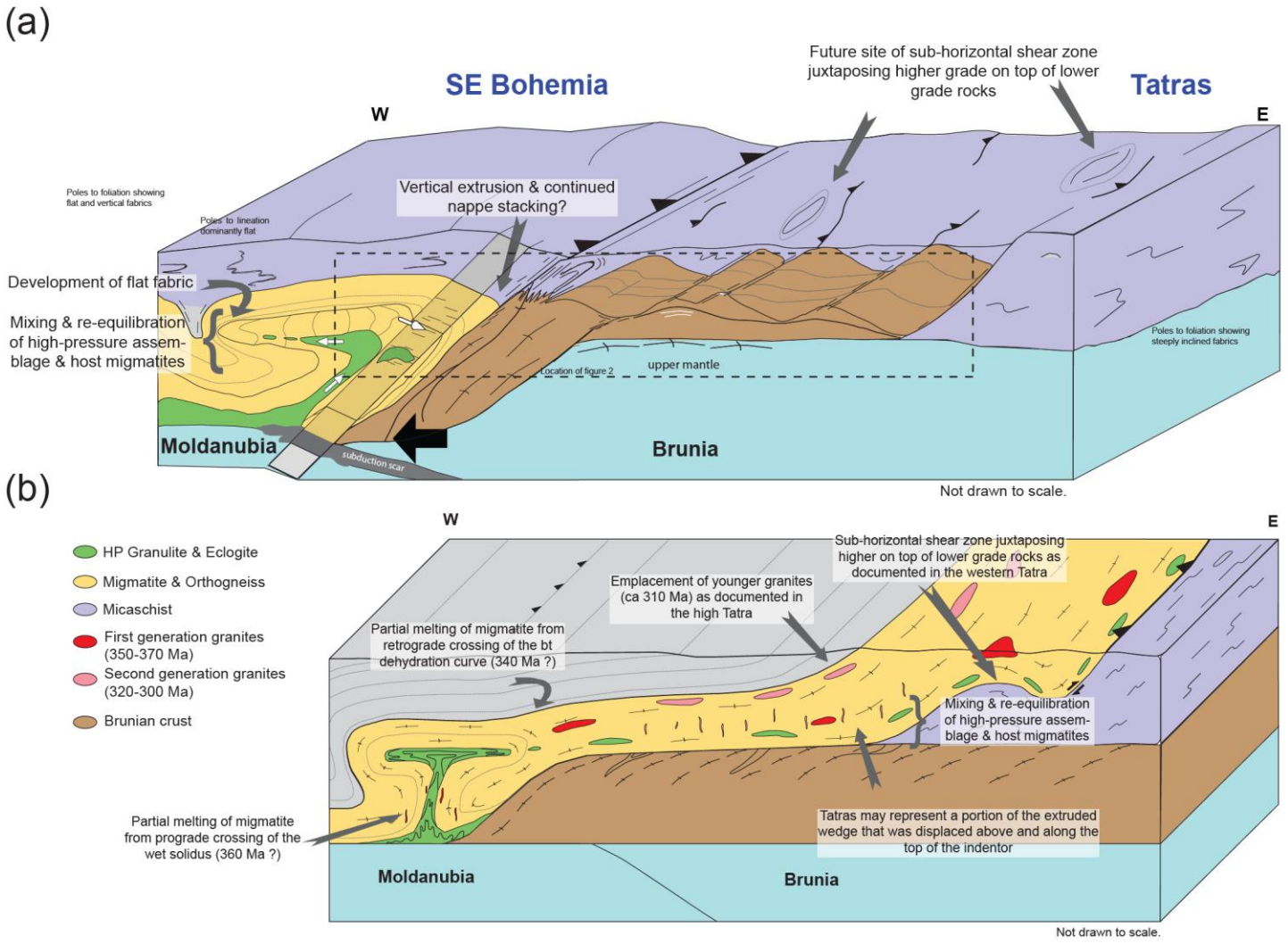

Figure 5.4: Tectonic model linking the evolution of the western Tatra to the SE Bohemian Massif. In this model lower crustal assemblages are mixing with mid-crustal material within an heterogeneous extrusion corridor were ductile material migrate above the rigid Brunian indentor. (a) The Bohemia-Brunia suture zone at ca. 350-340 Ma. (b) Close up of the Bohemia-Brunia suture zone (location of the dashed box in figure a) at ca 340-310 Ma.

Except for a major structural discontinuity between the upper and lower units, which caused an inverted metamorphic pattern, the Tatra lacks the widespread flat fabric found in many granulite terranes such as the Western Gneiss Region of Norway (e.g. Engvik & Andersen, 2000), the Grenville province (e.g. Rivers et al., 2002) and the Bohemian Massif (e.g. Stipska et al., 2008). If indeed Brunia behaved as an indentor with Bohemia during the Variscan, the Tatra represent a portion of the extruded Moldanubian wedge that was displaced above and along the top of the indentor (i.e. orogenic front). Kinematics in the moderately dipping fabric suggests that this portion of the middle crustal shear zone was a structural ramp that facilitated extrusion to shallower levels. Following Variscan shortening Permian rifting separated the Tatra from the rest of the southeastern Bohemian domains with significant strike-slip component. Later Alpine deformation further convoluted the relation between the two terranes leading to their contemporaneous disposition.

6. CONCLUSIONS

1. The P-T-t paths obtained for the migmatitic, eclogitic and micaschists lithologies that compose the Western Tatra metamorphic core show that the upper unit lithologies presently juxtaposed, underwent dissimilar metamorphic evolutions and most probably share only their retrograde path, possibly homogenizing under mid-crustal conditions. This crustal mixing occurred around ca. 340 Ma coeval with anatexis and was followed by cooling at a rate of ~ 30 °C/Ma.
2. Exhumation of the deep crustal root took place in a two-stage process. The timing of the first high-pressure metamorphic event, before exhumation commenced, is still unresolved and is likely constrained to occur between ca. 360 Ma and 380 Ma.
3. The thermal influence of the post-Variscan, Permian rifting and Cretaceous collision events in the Western Tatra was more significant than previously documented, which disturbed biotite and possibly even muscovite Ar systematics, indicating reheating to as much as 300 to 350°C.
4. Based on numerous geologic, geochemical and geochronologic similarities we suggest that the Moldanubia-Tatra system evolved as a coherent and ductile extruded segment of the mid-crust during the Variscan orogeny.
5. Extrusion was tectonically forced by the action of a rigid indenter into the weak Moldanubian crust. The Tatra separated from Moldanubia during Permian rifting only to be joined again during the course of Alpine collision.

ACKNOWLEDGEMENTS

Many thanks go to Lynn Heizler, Neila Dunbar, Patricia Hunt, William Zhe and Patrik Konečný for technical assistance with SEM and EMPA. We are also grateful to Matt Heizler for help with the Ar-Ar thermochronometric analysis, to Axel Schmidtt for technical assistance with ion microprobe depth-profiling and would also like to thank Tara Kell for help with XRF analysis, Jiri Mrazek for thin section cutting and finally Jenna Hojnowski and Daniel Holm for field work assistance.

REFERENCES

Andersen, T., 2002. Correction of common Pb lead in U-Pb analyses that do not report Pb-204. *Chemical Geology*, **192**, 59-79.

Beard, B. L., Medaris, L. G., Johnson, C. M., Brueckner, H. K. & Mısar, Z., 1992. Petrogenesis of Variscan high-temperature group A eclogites from the Moldanubian Zone of the Bohemian Massif, Czechoslovakia. *Contributions to Mineralogy & Petrology*, **111**, 468–483.

Beaumont, C., Nguyen, M. H., Jamieson, R. A. & Ellis, S., 2006. Crustal flow modes in large hot orogens. In: *Channel Flow, Ductile Extrusion & Exhumation in Continental Collision Zones, Special Publication*, **268** (eds Law, R. D., Searle, M. P. & Godin, L. et al.,). 91–145.

Berman, R.G., 1990. Mixing properties of Ca-Mg-Fe-Mn garnets. *American Mineralogist*, **75**, 328-344.

Bezák, V., Jacko, S., Janák, M., Ledru, P., Petrik, I. & Vozárová, A., 1997. Main Hercynian lithospheric units of the Western Carpathians. In: *Geological evolution of the Western Carpathians, Monograph* (eds Grecula, P., Hovorka, D., Putis, M.). 261-268. Bratislava: Mineralia Slovaca.

Boynton, W. V., 1984. Cosmochemistry of the rare earth elements: meteorite studies. In: *Rare Earth Element Geochemistry* (eds Henderson P.). Elsevier, Amsterdam, 63-114.

Breeding, C. M., Ague, J. J., Grove, M. & Rupke, A. L., 2004. Isotopic and chemical alteration of zircon by metamorphic fluids: U-Pb age depth-profiling of zircon crystals from Barrow's garnet zone, northeast Scotland. *American Mineralogist*, **89**, 7, 1067-1077.

Bromley, A. V. & Holl, J. 1986. Tin mineralization in southwest England. In: Mineral Processing at a crossroads (eds Wills, B.A. & Barley, R.W.) Martinus Nijhoff, Dordrecht, 159-262.

Brown, M. & Dallmayer, R. D., 1996. Rapid Variscan exhumation & the role of magma in core complex formation: southern Brittany metamorphic belt, France. *Journal of Metamorphic Geology*, **14**, 3, 361 – 379.

Burchart, J., 1968. Rubidium strontium isochron ages of the crystalline core of the Tatra Mountains, Poland. *American Journal of Science*, **266**, 895-907.

Burda, J. & Gaweda, A., 2009. Shear-influenced partial melting in the Western Tatra metamorphic complex: Geochemistry & geochronology. *Lithos*, **110**, 373–385.

Burda, J., 2007. U-Pb zircon & monazite dating of partial melting in migmatitic metapelites from the Western Tatra Mts. *Granitoids in Poland, AM Monograph*, **1**, 333-340.

Catlos, E. J., Gilley, L.D. & Harrison, T. M., 2002. Interpretation of monazite ages obtained via in situ analysis. *Chemical Geology*, **188**, 193-215.

Cocherie A. & Albarède F., 2001. An improved U-Th-Pb age calculation for electron-probe dating of monazite. *Geochimica and Cosmochimica Acta*, **65**, 4509-4522.

Connolly, J. A. D., 1990. Multivariable phase diagrams: an algorithm based upon generalized thermodynamics. *American Journal of Science*, **290**, 666-718.

Dallmeyer, D., Neubauer, F. & Hock, V., 1992. $^{40}Ar/^{39}Ar$ mineral age controls on the chronology of late-Paleozoic tectonothermal activity in the southeastern Bohemian Massif, Austria (Moldanubian and Moravosilesian zone). *Tectonophysics*, **210**, 135–153.

Dachs, E., & Proyers, A., 2002. Constraints on the duration of high-pressure metamorphism in the Tauern Window from diffusion modeling of discontinuous growth zones in eclogite garnet. *Journal of Metamorphic Geology*, **20**, 769–780.

Dobrzhinetskaya, L.F., Eide, E.A., Larsen, R.B., Sturt, B.A., Tronnes, R.G., Smith, D.C., Taylor, W.R. & Posukhova, T.V., 1995. Microdiamond in high-grade metamorphic rocks of the Western Gneiss Region, Norway, *Geology*, **23**, 597-600.

Dodson, M.H., 1986. Closure profiles in cooling systems. *Materials Science Forum*, **7**, 145–154. Dudek, A. & Fediuková, E., 1974. Eclogites of the Bohemian Moldanubicum. *Neues Jahrbbuch für Mineralogie Abhandlungen*, **121**, 127–159.

Dunlap, J. W., 2000. Nature's diffusion experiment: The cooling-rate cooling-age correlation. *Geology*, **28**, 2, 139-142.

Ellis, D. J., & Green, E. H., 1979. An experimental study of the effect of Ca upon garnet-clinopyroxene Fe - Mg exchange equilibria. *Contributions to Mineralogy & Petrology*, **71**, 13-22.

Engvik, A. K. & Andersen, T. B., 2000. Evolution of Caledonian deformation fabrics under eclogite & amphibolite facies at Vardalsneset, Western Gneiss Region, Norway. *Journal of Metamorphic Geology*, **18**, 241–257.

Ferry, J. M. & Spear, F. S., 1978. Experimental calibration of the partitioning of Fe & Mg between biotite & garnet. *Contributions to Mineralogy & Petrology*, **66**, 113-117.

Finger, F. & von Quadt, A., 1995. U/Pb ages from zircons from a plagiogranite-gneiss in the south-eastern Bohemian Massif, Austria – further evidence for an important early Paleozoic rifting episode in the eastern Variscides. *Schweizerische Mineralogische und Petrographische Mitteilungen*, **75**, 265–270.

Finger, F., Tichomirowa, M., Pin, C. & Hanžl, P., 2000. Relics of an early Panafrican metabasite–metarhyolite formation in the Brno Massif, Moravia, Czech Republic. *International Journal of Earth Sciences*, **89**, 328–335.

Finger, F., Broska, L., Haunschmid, B., Hrasko, L., Kohút, M., Krenn, E., Petrík, I., Riegler, G. & Uher, P., 2003. Electron-microprobe dating of monazites from Western Carpathian basement granitoids: plutonic evidence for an important Permian rifting event subsequent to Variscan crustal anatexis. *International Journal of Earth Sciences*, **92**, 86–98.

Floyd, P. A., Winchester, J. A., Seston, R., Kryza, R. & Crowley, Q. G., 2000 Review of geochemical variation in Lower Palaeozoic metabasites from the NE Bohemian Massif intracratonic rifting & plumeridge interaction. In: *Quantification & Modelling in the Variscan Belt of Central Europe* (eds Franke, W., Haak, V., Oncken, O., Tanner, D.), Geological Society of London, Special Volume, **179**, 155-174.

Foster, D. A., Goscombe, B. D. & Gray, D. R., 2009. Rapid exhumation of deep crust in an obliquely convergent orogen: The Kaoko Belt of the Damara Orogen. *Tectonics*, **28**, 4, 1-24.

Forster, M. A. & Lister, G. S. 2004. The interpretation of $^{40}Ar/^{39}Ar$ apparent age spectra produced by mixing: application of the method of asymptotes and limits. *Journal of Structural Geology*, **26**, 2, 287-305.

Franke, W., 2000: The mid-European segment of the Variscides: tectonostratigraphic units, terrane boundaries and plate tectonic evolution, In: *Quantification & Modelling in the Variscan Belt of Central Europe* (eds Franke, W., Haak, V., Oncken, O., Tanner, D.), Geological Society of London, Special Volume, **179**, 35-61.

Friedl, G., Cooke, R., Finger, F., McNaughton, N. J. & Fletcher, I., 2003. U-Pb SHRIMP dating & trace element investigations on multiple zircons from a South-Bohemian granulite. *Journal of the Czech Geological Society*, **48**, 51.

Friedl, G., Finger, F., Paquette, J. L., von Quadt, A., McNaughton, N. J. & Fletcher, I. R., 2004. Pre-Variscan geological events in the Austrian part of the Bohemian Massif deduced from U–Pb zircon ages. *International Journal of Earth Sciences*, **93**, 802–823.

Fritz, H., Dallmeyer, R. D. & Neubauer, F., 1996. Thick-skinned v. thin-skinned thrusting: rheology controlled thrust propagation in the Variscan collisional belt (the Southeastern Bohemian Massif, Czech Republic – Austria). *Tectonics*, **15**, 1389–1413.

Fritz, H., Neubauer, F., Janák, M. & Putiš, M. 1992. Variscan mid-crustal thrusting in the Carpathians II: Kinematics & fabric evolution of the Western Tatra basement. *Terra Nova*, **4**, 24.

Fuchs, G., 1986. Zur Diskussion um den Deckenbau der Böhmischen Masse, *Jahrbuch der Geologischen Bundesanstalt*, **129**, 41–49.

Ganguly, J., Cheng, W. & Chakraborty, S., 1998. Cation diffusion in aluminosilicate garnets; experimental determination in pyrope–almandine diffusion couples. *Contributions to Mineralogy & Petrology*, **131**, 171–180.

Ganguly, J. & Saxena, S. K., 1984. Mixing properties of aluminosilicate garnets: constraints from natural & experimental data, & applications to geothermobarometry. *American Mineralogist*, **69**, 88-97.

Gordon, S. M., Schneider, D. A., Manecki, M. & Holm, D. K., 2005. Exhumation and metamorphism of an ultrahigh-grade terrane: geochronometric investigations of the Sudete Mountains (Bohemia), Poland and Czech Republic. *Journal of the Geological Society (London)*, **162**, 841–855.

Graham, C. M., & Powell, R., 1984. A garnet-hornblende geothermometer: calibration, testing, & application to the Pelona Schist, Southern California. *Journal of Metamorphic Geology*, **2**, 13-21.

Heinrich, C. A., Pettke, T., Halter, W. E., Aigner-Torres, M., Audeta, A., Gunther, D., Hattendorf, B., Bleinder, D., Guillong, M. & Horn, I., 2003. Quantitative multi-element analysis of minerals, fluid & melt inclusions by laser-ablation inductively-coupled-plasma mass-spectrometry. *Geochimica & Cosmochimica Acta*, **67**, 3473-3496.

Hodges, K. V. & Crowley, P. D., 1985. Error estimation & empirical geothermobarometry for pelitic systems. *American Mineralogist*, **70**, 702-709.

Hoisch, T. D., 1990. Empirical calibration of six geobarometers for the mineral assemblage quartz + muscovite + biotite + plagioclase + garnet. *Contributions to Mineralogy & Petrology*, **104**, 225-234.

Holdaway, M. J., Dutrow, B. L., & Hinton, R. W., 1988. Devonian & Carboniferous metamorphism in west-central Maine: The muscovite-almandine geobarometer & the staurolite problem revisited. *American Mineralogist*, **73**, 20-47.

Holland, T.J.B. & Powell, R., 1998. An internally consistent thermodynamic dataset for phases of petrological interest. *Journal of Metamorphic Geology*. **16**, 309-343.

Janák, M. & Onstott, T. C., 1993. Pre-Alpine tectono-thermal evolution of the metamorphism in the Tatras Mts., Western Carpathians: P-T paths & $^{40}Ar/^{39}Ar$ laser probe dating. Terra *Nova*, **5** (Suppl. 1), 238 (abstract).

Janák, M., 1994. Variscan uplift of the crystalline basement. Tatra Mts., Central Western Carpathians: evidences from $^{40}Ar/^{39}Ar$ laser probe dating of biotite & P-T-t paths. *Geologica Carpathica*, **45**, 293-300.

Janák, M., O'Brien, J.P., Hurai, V. & Reutel, C., 1996. Metamorphic evolution & fluid composition of the garnet-clinopyroxene amphibolites from the Tatras Mountains, Western Carpathians. *Lithos*, **39**: 57-79.

Janák, M., Hurai, V., Ludhová, L., O'Brien, J. P. & Horn, E. E., 1999. Dehydration melting & devolatilization during exhumation of high-grade metapelites: the Tatra Mountains, Western Carpathians. *Journal of Metamorphic Geology*, **17**, 379-395.

Janák, M., Plašienka , D., Frey, M., Cosca, M., Schmidt, S. T., Lupták, B. & Méres, Š. 2001. Cretaceous evolution of a metamorphic core complex, the Veporic unit, Western Carpathians (Slovakia): P-T conditions and in situ $^{40}Ar/^{39}Ar$ UV laser probe dating of metapelites. *Journal of Metamorphic Geology*, **19**, 197-216.

Janák, M., Cornell, D.H., Froitzheim, N., De Hoog, J. C. M., Broska, I., Vrabec, M. & Hurai, V. 2009. Eclogite-hosting metapelites from the Pohorje Mountains (Eastern Alps): P-T evolution, zircon geochronology and tectonic implications. *European Journal of Mineralogy*, **21**, 1191-1212.

Janoušek, V., Farrow, C. M. & Erban, V., 2006. Interpretation of whole-rock geochemical data in igneous geochemistry: introducing Geochemical Data Toolkit (GCDkit). *Journal of Petrology*, **47**, 6, 1255-1259

Jeřábek, P., Janák, M., Farad, S.W., Finger, F. & Konečný, P. 2008. Polymetamorphic evolution of pelitic schists and an evidence for Permian low-pressure metamorphism in the Vepor Unit, West Carpathians. *Journal of Metamorphic Geology*, **26**, 465-485.

Jurewicz, E., 2005. Geodynamic evolution of the Tatra Mts. & the Pieniny Klippen Belt (Western Carpathians): problems & comments. *Acta Geologica Polonica*, **55**, 3, 295-338.

Kohn, M. J., & Spear, F. S., 1990. Two new barometers for garnet amphibolites with applications to eastern Vermont. *American Mineralogist*, **75**, 89-96.

Kohút, M. & Janák, M., 1994. Granitoids of the Tatra Mts., Western Carpathians: field relations and petrogenetic implications. *Geologica Carpathica*, **45**, 5, 301-311.

Kohùt, M., Poller, U., Gurk, C. & Todt, W., 2008. Geochemistry & U-Pb detrital zircon ages of metasedimentary rocks of the Lower Unit, Western Tatra Mountains (Slovakia). *Acta geologica Polonica*, **58**, 4, 371-384.

Kohùt, M., & Sherlock, S.C., 2003. Laser microprobe ^{40}Ar-^{39}Ar analysis of pseudotachylyte & host-rocks from the Tatra Mountains, Slovakia: evidence for late Paleogene seismic/tectonic activity. *Terra Nova*, **15**, 417-424

Kossmat, F. 1927. Gliederung des varistschen Gebirgsbaues. *ABH Sachsischen Geology Landesamts*, **1**, 1-36.

Kováč, M., Král', J., Márton, E., Plašienka, D. & Uher, P., 1994. Alpine uplift history of the Central Western Carpathians: geochronological, paleomagnetic, sedimentary & structural data. *Geologica Carpathica*, **45**, 83-96.

Koziol, A. M., 1989. Recalibration of the garnet - plagioclase - Al_2SiO_5 - quartz (GASP) geobarometer & applications to natural parageneses. *EOS*, **70**, 493.

Kretz, R., 1983. Symbols of rock-forming minerals. *American Mineralogist*, **68**, 277–279.

Kröner, A., Jaeckel, P., Hegner, E. & Opletal, M., 2001. Single zircon ages & whole-rock Nd isotopic systematics of early Palaeozoic granitoid gneisses from the Czech & Polish Sudetes (Jizerské hory, Krkonoše Mountains & Orlice-Snežník Complex). *International Journal of Earth Sciences*, **90**, 304-324.

Liu, F., Xu, Z., Liou, J.G., Katayama, I., Masago, H., Maruyama, S. & Yang, J., 2002. Ultrahigh-pressure mineral inclusions in zircons from gneissic core samples of the Chinese Continental Scientific Driling Site in eastern China. *European Journal of Mineralogy*, **14**, 499-512.

Ludwig, K., 2003. User manual for Isoplot 3.00, *Berkeley Geochronology Center Special Publication*, **4**.

Lugmair, G. W. & Marti, L., 1978. Lunar initial $^{143}Nd/^{144}Nd$ differential evolution of the lunar crus and mantle. *Earth and Planetary Science Letters*, **39**, 349-357.

Maluski, H., Rajlich, P. & Matte, P., 1993. ^{40}Ar ^{39}Ar dating of the Inner Carpathians Variscan basement & Alpine mylonitic overprint. *Tectonophysics*, **223**, 313-337.

Mahon, K.I., 1996. The New "York" regression: Application of an improved statistical method to geochemistry, *International Geology Review*, **38**, 293-303.

Marheine, D., Kachlik, V., Maluski, H., Patocka, F. & Zelazniewicz, A., 2002. The $^{40}Ar/^{39}Ar$ ages from the West Sudetes (NE Bohemian Massif): constraints on the Variscan polyphase tectonothermal development. In: *Paleozoic Amalgamation of Central Europe. Special Publications*, **201** (eds Winchester, J.A., Pharaoh, T.C. & Verniers, J.) Geological Society, London, 133–155.

Medaris, L. G., Ghent, E. D., Wang, H. F., Fournelle, J. H. & Jelínek, E., 2006. The Spačice eclogite: constraints on the P–T–t history of the Gföhl granulite terrane, Moldanubian Zone, Bohemian Massif. *Mineralogy & Petrology*, **86**, 203-220.

Medaris, L. G., Fournelle, J. H., Ghent, E. D., Jelínek, E. & Mísař, Z., 1998. Prograde eclogite in the Gföhl Nappe, Czech Republic: new evidence on Variscan high-pressure metamorphism. *Journal of Metamorphic Geology*, **16**, 563–576.

Mezger, K., 1990. Geochronology in granulites. In: *Granulites and Crustal Evolution* (eds Vielzeuf, D. & Vidal, P.H.), Kluwer, Dordrecht. The Netherlands, 451–470

Michard, A., Gurriet, P., Soudant, M. & Albarede, F., 1985. Nd isotopes in French Phanerozoic shales: external vs. internal aspects of crustal evolution. *Geochimica Cosmochimica Acta*, **49**, 601-610.

Moecher D. P., Essene, E. J., & Anovitz, L. M., 1988. Calculation & application of clinopyroxene - garnet - plagioclase - quartz geobarometers. *Contributions to Mineralogy & Petrology*, **100**, 92-106.

Nasdala, L. & Massonne, H. J., 2000. Microdiamonds from the Saxonian Erzgebirge, Germany: in situ micro-Raman characterisation. *European Journal of Mineralogy*, **12**, 495-498.

Nemčok, J., Bezák, V., Biely, A., Gorek, A., Gross, P., Halouzka, R., Janák, M., Kahan, Š., Mello, Š., Reichwalder, P. & Zelman, J., 1994. Geologická mapa Tatier, Bratislava, GÚDŠ.

Newton, R. C. & Haselton, H. T., 1981. Thermodynamics of the garnet- plagioclase-Al_2SiO_5-quartz geobarometer. In: *Thermodynamics of Minerals & Melts* (eds R. C. Newton, et al.,) Springer-Verlag, New York, pp. 131-147.

Paces, J. B. & Miller, J. D., 1993. Precise U-Pb ages of Duluth Complex and related mafic intrusions, northeastern Minnesota: Geochronological insights to physical, petrogenetic, paleomagnetic, and tectonomagmatic process associated with the 1.1 Ga Midcontinent Rift System. *Journal of Geophysical Research*, **98**, 13, 13997-14013.

Petrik, I., Konecny, P., Kováčik, Mártin. & Holicky, I., 2006. Electron microprobe dating of monazite from the Nizke Tatry Mountains orthogneisses (Western Carpathians, Slovakia). *Geologica Carpathica*, **57**, 4, 227-242.

Perchuk, L. L., Aranovich, L. Y., Podlesskii, K. K., Lavranteva, I. V., Gerasimov, V. Y., Fed'Kin, V. V., Kitsul, V. I., Karasakov, L. P., & Berdnikov, N. V., 1985. Precambrian granulites of the Aldan shield, eastern Siberia, USSR. *Journal of Metamorphic Geology*, **3**, 265-310.

Plašienka, D., Janák, M., Luptak, B., Milovsky, R. & Frey, M., 1999. Kinematics and metamorphism of a cretaceous core complex: the Veporic Unit of the Western Carpathians. *Physics & Chemistry of the Earth Part A-solid Earth & Geodesy*, **24**, 8, 651-658.

Poller, U., Todt, W., Janák, M. & Kohút, M., 1999. The geodynamic evolution of the Tatra Mountains constrained by new U-Pb single zircon data on orthogneisses, migmatites and granitoids. *Geologica Carpathica*, **50**, 129-131.

Poller, U., Janák, M., Kohùt, M. & Todt. W., 2000. Early Variscan magmatism in the Western Carpathians: U-Pb zircon data from granitoids & orthogneisses of the Tatra Mountains (Slovakia). *International Journal of Earth Sciences*, **89**, 336-349.

Poller, U., Uher, P., Broska, I., Plašienka, D. & Janák, M. 2002. First Permian-Early Triassic zircon ages for tin-bearing granites from the Gemeric unit (Western Carpathians, Slovakia): connection to the postcollisional extension of the Variscan orogen and S-type granite magmatism. *Terra Nova*, **14**, 1-7.

Powell, R. & Holland, T. J. B., 1988. An internally consistent thermodynamic dataset with uncertainties & correlations: 3. Applications to geobarometry, worked examples & a computer program. *Journal of Metamorphic Geology*, **6**, 173-204.

Powell, R., 1985. Regression diagnostics & robust regression in geothermometer/geobarometer calibration: the garnet-clinopyroxene geothermometer revisited. *Journal of Metamorphic Geology*, **3**, 231-243.

Pressler, R. E., Schneider, D. A., Petronis, M. S., Holm, D. K. & Geissman, J. W., 2007. Pervasive horizontal fabric & rapid vertical extrusion: Lateral overturning & margin sub-parallel flow of deep crustal migmatites, northeastern Bohemian Massif. *Tectonophysics*, **443**, 19-36.

Renne, P. R., Swisher, C. C., Deino, A. L., Karner, D. B., Owens, T. L. & DePaolo, D. J., 1998. Intercalibration of standards, absolute ages and uncertainties in $^{40}Ar/^{39}Ar$ dating. *Chemical Geology*, **145**, 1-2, 117-152.

Rivers, T., Ketchum, J., Indares, A. & Hynes, A. 2002. The High Pressure belt in the Grenville Province: architecture, timing, and exhumation. *Canadian Journal of Earth Sciences*, **39**, 5, 867-893

Robl, J., Hergarten, S., Stüwe, K. & Hauzenberger, C., 2007. THERMAL HISTORY: A new software to interpret diffusive zoning profiles in garnet. *Computers & Geosciences*, **33**,760–772.

Schmitt, A. K., Grove, M., Harrison, T. M., Lovera, O., Hulen, J. B. & Walters, M., 2003. The Geysers-Cobb mountain magma system California: U–Pb zircon ages of volcanic rocks conditions of zircon crystallization and magma residence times. *Geochimica et Cosmochimica Acta*, **67**, 3423–3458.

Schneider, D. A., Zahniser, S., Glascock, J., Gordon, S. M. & Manecki, M., 2006. Thermochronology of the West Sudetes (Bohemian Massif): rapid and repeated education in the eastern Variscides, Poland and Czech Republic. *American Journal of Science*, **306**, 846–873.

Schulmann, K., Kröner, A., Hegner, E., Wendt, I., Konopásek, J., Lexa, O. & Stípská, P., 2005. Chronological constraints on the pre-orogenic history, burial & exhumation of deep-seated

rocks along the eastern margin of the Variscan orogen, Bohemian Massif, Czech Republic. *American Journal of Science*, **305**, 407–448.

Schulmann, K., Lexa, O., Stıpska, P., Racek, M., Tajcmanova, L., Konopasek, J., Edel, J. B., Peschler, A. & Lehmann, J., 2008. Vertical extrusion & horizontal channel flow of orogenic lower crust: key exhumation mechanisms in large hot orogens? *Journal of Metamorphic Geology*, **26**, 273–297.

Schulmann, K., Konopásek, J., Janoušek, V., Lexa, O., Lardeaux, J. M., Edel, J. B., Štípská, P. & Ulrich, S., 2009. An Andean type Palaeozoic convergence in the Bohemian Massif. Comptes Rendus Geoscience, **341**, 266-286

Schuster, R. & Stüwe, K., 2008. Permian metamorphic event in the Alps. *Geology*, **36**, 8, 603-606.

Smith, H. A. & Giletti, B. J., 1997. Lead diffusion in monazite. *Geochimica et Cosmochimica Acta*, **61**, 5, 1047-1055.

Sobolev, N.V. & Shatsky, V. S., 1990. Diamond inclusions in garnets from metamorphic rocks: a new environment for diamond formation. *Nature*, **343**,742-746.

Spear, F. S., 1993. Metamorphic Phase Equilibria & Pressure-Temperature-Time Paths. Monograph 1, Mineralogical Society of America, Chantilly, Virginia.

Spear, F.S. & Kohn, M.J., 1999. Program GTB: Geothermo-barometry. Version 2.1: Departement of Earth and Environmental Sciences, Rensselaer Polytechnic Institute.

Stampfli, G. & Borel, G. D., 2002. A plate tectonic model for the Paleozoic and Mesozoic constrained by dynamic plate boundaries and restored synthetic oceanic isochrones. *Earth and Planetary Science Letters*, **196**, 17-33.

Steiger R., & Jaeger, E., 1977. Subcommission on Geochronology: Convention on the use of decay constants in geo- and cosmochronology. *Earth and Planetary Science Letters*, **36**, 359–362.

Stipska, P., Schulmann, K. & Powell, R., 2008. Contrasting metamorphic histories of lenses of high-pressure rocks & host migmatites with a flat orogenic fabric (Bohemian Massif, Czech Republic): a result of tectonic mixing within horizontal crustal flow? *Journal of Metamorphic Geology*, **26**, 623–646.

Stıpska, P., Schulmann, K. & Kröner, A., 2004. Vertical extrusion & middle crustal spreading of omphacite granulite: a model of syn-convergent exhumation (Bohemian Massif, Czech Republic). *Journal of Metamorphic Geology*, **22**, 179–198.

Strnad, L. & Mihaljevic, M. 2005. Sedimentary provenance of Mid-Devonian clastic sediments in the Teplá-Barrandian Unit (Bohemian Massif): U–Pb and Pb–Pb geochronology of detrital zircons by laser ablation ICP-MS, *Mineralogy & Petrology*, **84**, 47–68.

Suess, F. E. 1926. Intrusionstektonik und Wandertektonik im variszischen Grundebirge. Borntraeger. Berlin.

Suzuki, K., Adachi, M., & Kajizuka, I. 1994. Electron microprobe observations of Pb diffusion in metamorphosed detrital monazites. *Earth and Planetary Science Letters*, **128**, 391-405.

Taylor, J. R. 1982. An introduction to error analysis: the study of uncertainties in physical measurements. University Science Books, Mill Valley, 1–269.

Thöni, M. & Miller, C., 2009. The "Permian event" in the Eastern European Alps: Sm–Nd and P–T data recorded by multi-stage garnet from the Plankogel unit. *Chemical Geology*, **260**, 1-2, 20-36.

Tirone, M., Ganguly, J., Dohmen, R., Langenhorst, F., Hervig, R. & Becker, H-W., 2005. Rare-earth diffusion kinetics in garnet: experimental studies & implications. *Geochimica Cosmochimica Acta*, **69**, 2385-2398.

Walsh, E. & Hacker, B. 2004. The fate of subducted continental margins: two stage exhumation of the high-pressure to ultrahigh-pressure Western Gneiss Region, Norway. *Journal of Metamorphic Geology*, **22**, 671–687.

Weyer, S., Jarick, J. & Mezger, K., 1999. Quantitative temperature-time information from retrograde diffusion zoning in garnet: constraints for the P–T–t history of the Central Black Forest, Germany. *Journal of Metamorphic Geology*, **17**, 449-461.

Wiedenbeck, W., Alle, P., Corfu, F., Griffin, W. L., Meier, M., Oberli, F., Von Quad, A., Roddick, J. C. & Spiegel, W., 1995. Three natural zircon standards for U-Th-Pb, Lu-Hf, trace element & REE analyses. *Geostandards Newsletter*, **19**, 1-23.

Yan, H., Gao, S., Liu, X., Li, H., Günther, D. & Wu, F., 2004. Accurate U-Pb age & trace element determinations of zZircon by laser ablation-inductively coupled plasma-mass spectrometry. *Geostandards & Geoanalytical Research*, **28**. 353-370.

Zeck, H. P., Monié, P., Villa, I. M., & Hansen, B. T., 1992. Very high rates of cooling & uplift in the alpine belt of the Betic Cordilleras, southern Spain. *Geology*, **20**, 79–82.